AD-A247 294

TATION PAGE

.. ~~AGENCY~~ USE ONLY (Leave blank)	2. REPORT DATE	3. REPORT TYPE AND DATES COVERED
	1 February 1992	Final: 1 Jan. 1982 – 31 Jan. 1990

4. TITLE AND SUBTITLE	5. FUNDING NUMBERS
Nanostructure, Defect Chemistry and Properties of Relaxor Ferroelectrics	C N00014-82-K-0190

6. AUTHOR(S)

M. P. Harmer and D. M. Smyth

Mod. P00007

7. PERFORMING ORGANIZATION NAME(S) AND ADDRESS(ES)	8. PERFORMING ORGANIZATION REPORT NUMBER
Lehigh University Bethlehem, Pennsylvania 18015	533614

9. SPONSORING/MONITORING AGENCY NAME(S) AND ADDRESS(ES)	10. SPONSORING/MONITORING AGENCY REPORT NUMBER
Office of Naval Research Ceramics Program Materials Division 800 N. Quincy Street Arlington, VA 22217	

DTIC ELECTE MAR 0 5 1992 S D

11. SUPPLEMENTARY NOTES

13. ABSTRACT (Maximum 200 words)

This research focused on cation ordering, defect chemistry, and dielectric properties of the $BaTiO_3$-$Ba(Zn_{1/3}Nb_{2/3})O_3$ (BZN) system. The latter compound was chosen as an analog of the PbO-based relaxor ferroelectrics to avoid the severe experimental restrictions caused by the volatility and reducibility of PbO.

Two types of ordering of the Zn and Nb content of BZN were observed; a 1:1 (alternate layer) type that represents a local compositional change and charge imbalance that restricts the size of ordered domains, and a 1:2 type that is consistent with the composition of BZN. The effects of the Zn/Nb ratio and doping on the type and extent of ordering were determined. The defect chemistry of BZN is closely related to that of $BaTiO_3$, which has been well-characterized. The material usually contains a large concentration of extrinsic oxygen vacancies because of compositional variations and ZnO loss. Mass-action expressions and thermodynamic parameters of the oxidation and reduction reactions, and of the band gap were determined. The proposed defect model is in excellent quantitative agreement with the experimental observations. The evolution of dielectric properties was studied as the Ti content of $BaTiO_3$ was gradually replaced by $Zn_{1/3}Nb_{2/3}$

14. SUBJECT TERMS	15. NUMBER OF PAGES
Relaxor ferroelectrics, Barium Zinc Niobate, Defect chemistry, Cation ordering, Dielectric properties	183
	16. PRICE CODE

17. SECURITY CLASSIFICATION OF REPORT	18. SECURITY CLASSIFICATION OF THIS PAGE	19. SECURITY CLASSIFICATION OF ABSTRACT	20. LIMITATION OF ABSTRACT
Unclassified	Unclassified	Unclassified	UL

GENERAL INSTRUCTIONS FOR COMPLETING SF 298

The Report Documentation Page (RDP) is used in announcing and cataloging reports. It is important that this information be consistent with the rest of the report, particularly the cover and title page. Instructions for filling in each block of the form follow. It is important to *stay within the lines* to meet *optical scanning requirements.*

Block 1. Agency Use Only (Leave blank).

Block 2. Report Date. Full publication date including day, month, and year, if available (e.g. 1 Jan 88). Must cite at least the year.

Block 3. Type of Report and Dates Covered. State whether report is interim, final, etc. If applicable, enter inclusive report dates (e.g. 10 Jun 87 - 30 Jun 88).

Block 4. Title and Subtitle. A title is taken from the part of the report that provides the most meaningful and complete information. When a report is prepared in more than one volume, repeat the primary title, add volume number, and include subtitle for the specific volume. On classified documents enter the title classification in parentheses.

Block 5. Funding Numbers. To include contract and grant numbers; may include program element number(s), project number(s), task number(s), and work unit number(s). Use the following labels:

C	- Contract	PR	- Project
G	- Grant	TA	- Task
PE	- Program Element	WU	- Work Unit Accession No.

Block 6. Author(s). Name(s) of person(s) responsible for writing the report, performing the research, or credited with the content of the report. If editor or compiler, this should follow the name(s).

Block 7. Performing Organization Name(s) and Address(es). Self-explanatory.

Block 8. Performing Organization Report Number. Enter the unique alphanumeric report number(s) assigned by the organization performing the report.

Block 9. Sponsoring/Monitoring Agency Name(s) and Address(es). Self-explanatory.

Block 10. Sponsoring/Monitoring Agency Report Number. *(If known)*

Block 11. Supplementary Notes. Enter information not included elsewhere such as: Prepared in cooperation with...; Trans. of...; To be published in.... When a report is revised, include a statement whether the new report supersedes or supplements the older report.

Block 12a. Distribution/Availability Statement. Denotes public availability or limitations. Cite any availability to the public. Enter additional limitations or special markings in all capitals (e.g. NOFORN, REL, ITAR).

DOD - See DoDD 5230.24, "Distribution Statements on Technical Documents."
DOE - See authorities.
NASA - See Handbook NHB 2200.2.
NTIS - Leave blank.

Block 12b. Distribution Code.

DOD - Leave blank.
DOE - Enter DOE distribution categories from the Standard Distribution for Unclassified Scientific and Technical Reports.
NASA - Leave blank.
NTIS - Leave blank.

Block 13. Abstract. Include a brief *(Maximum 200 words)* factual summary of the most significant information contained in the report.

Block 14. Subject Terms. Keywords or phrases identifying major subjects in the report.

Block 15. Number of Pages. Enter the total number of pages.

Block 16. Price Code. Enter appropriate price code *(NTIS only).*

Blocks 17. - 19. Security Classifications. Self-explanatory. Enter U.S. Security Classification in accordance with U.S. Security Regulations (i.e., UNCLASSIFIED). If form contains classified information, stamp classification on the top and bottom of the page.

Block 20. Limitation of Abstract. This block must be completed to assign a limitation to the abstract. Enter either UL (unlimited) or SAR (same as report). An entry in this block is necessary if the abstract is to be limited. If blank, the abstract is assumed to be unlimited.

FINAL REPORT

Office of Naval Research Agreement N00014-82-K-0190, Mod. P00007

1 January 1982 to 31 January 1990

Nanostructure, Defect Chemistry, and Properties of Relaxor Ferroelectrics

M. P. Harmer and D. M. Smyth
Materials Research Center, Lehigh University

This report deals with the final work done on this project related to the reliability of ceramic dielectrics. It represents the doctoral dissertation of Dr. P. Peng. While the funding for this project concluded on 31 January, 1990, the research continued until Dr. Peng received his PhD in January, 1991. In order to present a complete picture, the entire dissertation is being distributed in the form of this report.

The purpose of this research was to investigate cation ordering phenomena, the defect chemistry, and the electrical properties of a well-characterized material having a composition closely related to those of the relaxor ferroelectrics. The latter materials are most commonly Pb-based compounds having the generic formula $Pb(B'_{1/2}B''_{1/2})O_3$ or $Pb(B'_{1/3}B''_{2/3})O_3$, where B' and B'' may be either a trivalent and a pentavalent cation (the former case), or a divalent and a pentavalent cation (the latter case), for example. The structures are closely related to the familiar perovskite structure. These ferroelectric oxides have unusually high dielectric constants with an extended ferroelectric transition that exhibits frequency dispersion.

Since the volatility of PbO causes serious problems in the precise control of the cation content, and because its easy reducibility greatly restricts the oxygen activity range over which the equilibrium defect chemistry can be studied, a Ba analog was chosen for this study, namely $Ba(Zn_{1/3}Nb_{2/3})O_3$, BZN. Since the cation ordering and the defect chemistry are almost entirely determined by the cations on the octahedrally-coordinated sites, i.e. the Zn and Nb, the substitution of Ba^{++} for Pb^{++} has very little effect on these aspects. The electrical properties were studied over the entire $BaTiO_3$-BZN compositional range. The dielectric properties of the true relaxor ferroelectrics have been extensively studied elsewhere. There has been some interest in BZN itself as a microwave dielectric, but that has not been the focus of this research.

SUMMARY

This report describes a systematic study of the characterization of the phase transitions, microstructures, defects and transport properties of undoped and doped complex perovskite barium zinc niobate, $Ba(Zn_{1/3}Nb_{2/3})O_3$ (BZN).

Complex perovskite BZN is a paraelectric material while its parent material barium titanate is ferroelectric. Codoping of (Zn + 2Nb) into the Ti site of $BaTiO_3$ results in three distinguishing features. First, the Curie temperature is lowered; second, the three phase transitions (cubic-tetragonal-orthorhombic-rhombohedral) coalesce; and lastly, the transition becomes diffuse showing a typical 2nd order phase transition compared with 1st order in undoped $BaTiO_3$.

Complex microchemical ordering is another characteristic of BZN. Stoichiometric BZN shows a mixture of two types of ordering schemes among the B-site cations. 1:1 and 1:2 ordered microdomains and the disordered matrix co-exist. The 1:1 type ordering involves an internal charge imbalance which inhibits the growth of 1:1 type of ordered microdomains. The 1:2 type ordering is consistent with the chemical composition of BZN. These ordering patterns can be modified by either adjustment of the Zn/Nb ratio or by doping.

The defect structure of the stoichiometric BZN is closely related to that of $BaTiO_3$. Stoichiometric BZN is an insulator with wide band gap (~3.70 eV). Undoped BZN has a high oxygen vacancy concentration which comes from three possible sources, such as unavoidable acceptor impurities, due to their natural abundance, Zn/Nb ratio uncertainty due to processing limitations, and high temperature ZnO loss during the sintering process. The oxygen vacancy concentration for undoped BZN lies in the neighborhood of 1500 ppm (atomic). The compensating defects for various dopants have also been identified.

Both electrons and holes conduct by a small polaron mechanism. Various thermodynamic parameters, such as enthalpies of oxidation and reduction, mass-action constants for intrinsic electronic disorder, oxidation and reduction have been determined. Finally, the defect concentrations and conductivities are calculated based on the proposed defect model. A computer simulation yields excellent agreement between theoretical calculations and experimental observations.

In conclusion, a self-consistent picture of the phase transitions, ordering and defects, along with their migration in BZN, has been obtained.

TABLE OF CONTENTS

LIST OF FIGURES

taken from [110] zone axis at 300 kV with near optimum Scherzer defocus condition, showing 1:2 type of ordered microdomains with two variants at this particular zone axis. The laser ODM patterns are taken from the HRTEM negatives.

LIST OF TABLES

LIST OF ABBREVIATIONS

A	Energy transform term.
A$'$	Acceptors.
AC	Alternating Current.
AEM	Analytical Electron Microscopy.
α	Seebeck Coefficient/Thermal Electric Power (mV/$^\circ$C).
α_e	Electron polarizability.
α_i	Ionic polarizability.
APBs	Anti-Phase Domain Boundaries.
$Ba_I^{\cdot\cdot}$	Ba in an interstitial site.
BF	Bright Field.
BMN	$Ba(Mg_{1/3}Nb_{2/3})O_3$.
BMT	$Ba(Mg_{1/3}Ta_{2/3})O_3$.
BSE	Backscattering Electron.
BST	$Ba(Sr_{1/3}Ta_{2/3})O_3$.
BT	$BaTiO_3$.
BKZN	$Ba_{1-x}K_x(Zn_{(1-x)/3}Nb_{(2+x)/3})O_3$.
BKZN$'$	$Ba_{1-x}K_x(Zn_{1/3}Nb_{2/3})O_{3-x/2}$.
BLZN	$Ba_{1-x}La_x(Zn_{(1+x)/3}Nb_{(2-x)/3})O_3$.
BLZN$'$	$Ba_{1-3x/2}La_x(Zn_{1/3}Nb_{2/3})O_3$.
BZN	$Ba(Zn_{1/3}Nb_{2/3})O_3$.
BZNB	$Ba(Ba_xZn_{1/3-x}Nb_{2/3})O_3$.
BZNN	$Ba(Zn_{1/3}Nb_{2/3})_{1-x}Nb_xO_3$.
BZNZ	$Ba(Zn_{1/3}Nb_{2/3})_{1-x}Zn_xO_3$.
C	Capacitance.
σ	Electrical conductivity.
σ_e	Electron conductivity.
σ_h	Hole conductivity.
σ_i	Ionic conductivity.
σ_t	Total electrical conductivity.
θ	Phase angle between Y^* and Y'.
CBED	Convergent Beam Electron Diffraction.
CDF	Centered Dark Field.

C_p	Parallel capacitance.
C_s	Series capacitance.
CT	$CaTiO_3$.
$D^{\cdot}$	Donors.
dc	Disordered cubic.
DC	Direct Current.
Δ	Crystal field stabilization energy.
ΔH_s	Enthalpy of formation of Schottky defects.
ΔH_m	Enthalpy of electrical charge carrier motion.
ΔH_O	Enthalpy of oxidation.
ΔH_R	Enthalpy of reduction.
ΔT_c	Curie temperature difference.
DPT	Diffuse Phase Transition.
DSC	Differential Scanning Calorimetry.
e	Electron charge ($1.602 * 10^{-19}$ C).
E	External electrical field.
e'	Electron.
ϵ^*	Complex permittivity ($\epsilon^* = \epsilon' + j\epsilon''$).
ϵ_o	Dielectric constant in vacuum ($8.854*10^{-12}$ F/m).
ϵ_r	Relative dielectric constant.
E_c	Valence band edge energy.
E_d	Donor energy level.
EDS	Energy Dispersive Spectrum (or Spectrometer).
E_F	Fermi energy level.
Eg	Energy band gap; $E_g^{(o)}$: energy band gap at o degree Kelvin.
EG	Ethylene glycol.
E_L	Lorentz local electrical field.
EPMA	Electron Probe Micro-Analysis.
eV	Electron volt.
f	Frequency.
FCC	Face Center Cubic.
FEG-STEM	Field Emission Gun-Scanning Transmission Electron Microscopy.
FIM	Field Ion Microscopy.
G	Conductance.

h	Planck's Constant.
$h^{\cdot}$	Hole.
HP	Hewlett-Packard.
HRTEM	High Resolution Transmission Electron Microscopy.
IEEE	Institute of Electrical and Electronic Engineers.
I-V	Current-Voltage.
k	Boltzmann constant/or quantity 1000.
κ	Thermal conductivity.
K	Degree Kelvin.
$K_{Ba}{}'$	A potasium atom on a barium lattice site.
K_i	Mass action constant for intrinsic electronic disorder.
K_s	Mass action constant for intrinsic Schottky disorder.
K_O	Mass action constant for oxidation.
K_R	Mass action constant for reduction.
LCR	Inductance-Capacitance-Resistance.
LCN	$La(Co_{1/3}Nb_{2/3})O_3$.
M^*	Complex modulus ($M^* = M' + jM''$).
m^o	Electron rest mass ($9.109*10^{-31}$ kg).
m^*_e	Electron effective mass.
m^*_h	Hole effective mass.
μ/μ_i	Charge carrier mobility.
μ_o	Constant for mobility expressions.
μ_e/μ_h	Electron/hole mobility.
μ_T	Electrical charge carrier mobility due to lattice vibration.
μ_I	Electrical charge carrier mobility due to impurity scattering.
MPa	Mega-Pascal.
ν_{ph}	Lattice vibration frequency.
n/n_i	Electron concentration/charge carrier concentration.
$Nb_{Ti}^{\cdot}$	A niobium atom on a titanium lattice site.
$Nb_{Zn}^{\cdots}$	A niobium atom on a zinc lattice site.
N_d	Donor concentration.
NIST	National Institute of Science and Technology.
n_o	Density of state.
N_o	Total number of the oxygen lattice site.

ω	Angular frequency ($\omega = 2\pi f$).
Ω	Frequency of an emitted phonon.
ODM	Optical Diffractometry.
O_I''	An oxygen atom in an interstitial site.
Oo	An oxygen atom on an oxygen lattice site.
OSC	Oscillation level.
ot	Ordered trigonal.
p	Hole concentration.
P	Polarization/electron pairing energy.
PFW	$Pb(Fe_{2/3}W_{1/3})O_3$.
PMN	$Pb(Mg_{1/3}Nb_{2/3})O_3$.
Po_2	Oxygen partial pressure.
PST	$Pb(Sc_{1/2}Ta_{1/2})O_3$.
PSW	$Pb(Sc_{2/3}W_{1/3})O_3$.
PT	$PbTiO_3$.
PTC	Positive Temperature Coefficient.
PZN	$Pb(Zn_{1/3}Nb_{2/3})O_3$.
PZT	$Pb(Zr_xTi_{1-x})O_3$.
q	Electron charge ($1.602 * 10^{-19}$ C).
Q	Dielectric loss quality factor.
RF	Radio Frequency.
R_H	Hall coefficient.
R_p	Parallel resistance.
R_s	Series resistance.
SAEDP	Selected Area Electron Diffraction Pattern.
SAXS	Small Angle X-ray Scattering.
SE	Secondary Electron.
SEM	Scanning Electron Microscopy.
SLTC	$Sr_{1-x}La_x(Ti_{1-x}Co_x)O_3$.
SMN	$Sr(Mg_{1/3}Nb_{2/3})O_3$.
Sr_{Nb}'''	A strontium atom on a niobium lattice site.
Sr_{Sr}	A strontium atom on a strontium lattice site.
SSN	$Sr(Sr_{1/3}Nb_{2/3})O_3$.
ST	$SrTiO_3$.

STEM	Scanning Transmission Electron Microscopy.
SZN	$Sr(Zn_{1/3}Nb_{2/3})O_3$.
τ	Relaxation time.
T	Temperature.
T_c	Curie temperature/cold end temperature for α measurement.
TEM	Transmission Electron Microscopy.
TGA	Thermal Gravimetric Analysis.
T_h	Hot end temperature for α measurement.
3D	3 Dimension.
TPT	Tetra-isopropyl-titanate.
V_B''''	B-site cation vacancy.
V_{Ba}''	Barium vacancy.
V_c	Cold end voltage for α measurement.
V_h	Hot end voltage for α measurement.
V_{Nb}'''''	Niobium vacancy.
$V_O^{\cdot\cdot}$	Oxygen Vacancy.
V_{Sr}''	Strontium vacancy.
V_{Ti}''''	Titanium Vacancy.
WDS	Wave-length Dispersive Spectrum (or Spectrometer).
XRD	X-ray Diffractometry.
Z^*	Complex impedance ($Z^* = Z' + jZ''$).
Y^*	Complex admittance ($Y^* = Y' + jY''$).
Zn_{Ti}''	A zinc atom on a titanium lattice site.
Zn_{Nb}'''	A zinc atom on a niobium lattice site.

Chapter 1 <u>BACKGROUND</u>

1.1) *Introduction*

Since the middle of this century, the use of ceramics in electrical and electronic equipment has become widespread. It is well known that the great advantages offered by electronic ceramics are inherently connected with their defects and microstructures. In particular, many unique properties depend upon the defect states (e.g. doping), transport mechanism, order/disorder crystal structure and phase transitions etc.. Solid state chemistry and microstructure are favorite topics studied by ceramists, chemists and physicists. Hundreds of papers devoted to the doping, defect chemistry, microstructural development and order/disorder phenomena are published each year. More and more meetings and symposia on these topics are held around the world. Nevertheless, in contrast with the development of crystalline semiconductors, where desired electrical properties are often derived from appropriate design and control of doping species and levels, the development of electronic ceramics has followed a rather more empirical evolutionary growth.

It is appropriate to ask why the technology of crystalline semiconductors has advanced more rapidly than electronic ceramic technology. The main reason is that the semiconductor devices are prepared from very high purity single crystals under carefully controlled conditions. Another important reason is that the design of semiconductor devices is based on a thorough understanding of defect structure, transport mechanism and carefully controlled microstructures. In contrast, the vast majority of polycrystalline ceramics are produced using less defined synthesis and manufacturing processes. Electronic ceramics are often multicomponent and multiphase. In addition, they can possess significant macroscopic and microscopic defects. Uncontrolled impurity levels are usually very high which can drastically affect the electrical/electronic properties of working devices. Furthermore, complex crystal structures, defect equilibria, and especially order/disorder phenomena are not easy to control independently. Therefore, the reliability of final working devices has always been a difficult problem for almost all devices made of electronic ceramics materials. These difficulties impede the development of electronic ceramics.

In spite of these problems, many significant developments have occurred in electronic ceramics. Among these are the ZnO varistor, $BaTiO_3$ (BT) PTC (positive

3

temperature coefficient) thermistor, boundary layer capacitor, and piezoelectric transducers, pyroelectric sensors, electrostrictive actuators, high dielectric loss quality factor Q ceramic microwave resonators and high temperature ceramic superconductors (Herbert, J.M., 1982; Levinson, L.M., 1988; Glass, A.M., et.al., 1977). The development of electronic ceramics has not only rested content with achievement in the understanding of their behavior, but has moved forward in tailoring their properties for specific electrical and electronic applications. The reliability of electronic ceramic devices has been improved greatly based on the understanding of structure, defects and their migration under various conditions. A new stage of development of electric/electronic devices by tailoring electronic ceramic material properties using microstructural and defect chemistry control has started. The current trends and activities in this field are well summarized in the following overview papers by Cross, L.E. (1990, 1988, 1987, 1984), Newnham, R.E. (1989), Smyth, D.M. (1989, 1985, 1984), and Harmer, M.P., et.al., (1989). The emphasis of defect chemistry and microstructural study in electronic ceramics are on controlling chemical composition with the use of dopants, high temperature defect structure, redox (reduction/oxidation) behavior, mass and charge transport phenomena, cation/anion ordering, phase transitions and resultant electric/dielectric properties. Since most electronic ceramics are fabricated at high temperature and in different atmospheres under either equilibrium or non-equilibrium conditions, a thorough understanding of all these aspects will help with the development of new materials for various device applications and improvement of device reliability. The advent of many new analytical techniques and defect chemistry is having a profound impact upon the understanding of structure/defects and property relationship. Now we are at the turning point of developing new materials, designing new devices and improving product reliability from general qualitative investigations toward more accurate quantitative control.

1.2) *Statement of Problem*

Relaxor ferroelectrics and other structurally-related compounds are emerging as a technically important class of materials for use in a wide variety of applications. Two important characteristic features associated with these materials are their complex crystal structures and defect structures. The complex crystal structure usually contains a compensated mixture of cations with the same valence as A or B-site cations or with higher and lower valence cations mixed together. The complex defect structure varies from case to case depending upon, for example, the property of the transition metal

cations involved. Some examples of relaxor ferroelectrics are: $Pb(Zr_{1-x}Ti_x)O_3$ (PZT), $Pb(Sc_{1/2}Ta_{1/2})O_3$ (PST), $Pb(Mg_{1/3}Nb_{2/3})O_3$ (PMN), $Pb(Zn_{1/3}Nb_{2/3})O_3$ (PZN), $Pb(Fe_{2/3}W_{1/3})O_3$ (PFW), $Sr_{1/2}La_{1/2}(Co_{1/2}Ti_{1/2})O_3$ (SLCT). Examples of non-ferroelectric systems in the same structural family as relaxors are: $Sr(Sr_{1/3}Nb_{2/3})O_3$ (SSN), $Sr(Mg_{1/3}Nb_{2/3})O_3$ (SMN), and $Ba(Zn_{1/3}Nb_{2/3})O_3$ (BZN). The ferroelectric materials, especially lead-based systems are mostly used in high dielectric constant applications such as multilayer capacitors. The structurally-related non-ferroelectric strontium and barium based compounds have relatively low dielectric constants, e.g. 30 for BMN versus 20,000 for PMN. and are more suited for high frequency applications.

In all of these systems the electrical properties are influenced to a large degree by the cation ordering and the redox behavior of the transition metal ions. For example, in relaxor ferroelectrics, short-range ordering on the B-site sub-lattice gives rise to B-site compositional fluctuations occurring on a nanometer scale, and is believed to be responsible for the diffuse phase transition (DPT) characteristic of relaxors (Chen, J. et.al., 1989; Cross, L.E., 1987; Chan, H.M., et.al., 1985; Setter, N., 1980), see figure 1.1. In some of the barium and strontium analogs to the relaxors (e.g. SMN and BZN), the dielectric loss quality factor (Q) at microwave frequencies is significantly affected by the degree of B-site cation ordering (Matsumo, K. et.al., 1986; Tamura, H., et.al., 1986, 1984; Wakino, K., et.al., 1985 and Kawashima, S., et.al, 1983) On the other hand, for $Sr_{1-x}La_x(M_xTi_{1-x})O_3$ compounds where M is a transition metal with +3 valence (e.g. Cr, Co Ni Fe etc.), the formation of a grain boundary layer depends upon the enthalpy of oxidation of transition metal cations (Peng, P., et.al, 1990). This can greatly affect the dielectric relaxation behavior of final polycrystalline ceramic products. In addition, the reliability of electronic/electric devices, such as ferroelectric thin film memory devices, relaxor ferroelectric capacitors, and microwave resonators, is also greatly dependent upon the correspondent defect chemistry.

Because of the technical and fundamental importance of these relaxor ferroelectrics and structurally related non-ferroelectric complex perovskite materials, their structure-property relations have been researched significantly over the past five decades (Newnham, R.E., 1989, 1975). However, due to cation volatility and easy reducibility of lead-based relaxor systems at high temperature, very little earlier work appears to have been carried out on high temperature defect chemistry, or on the relationship between defect chemistry and dielectric properties. A French research
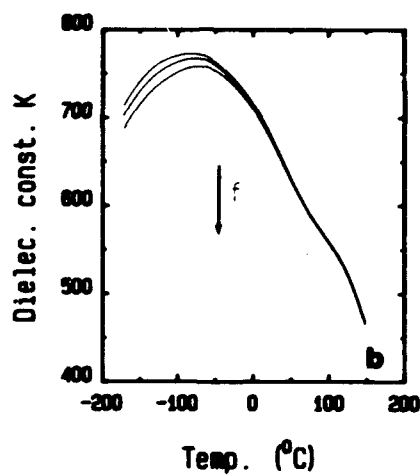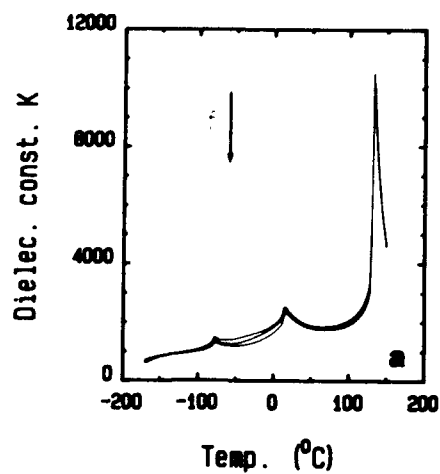
Figure 1.1 (a) Temperature and frequency dependence of dielectric constant of BT, showing a typical first order ferroelectric to paraelectric phase transition. (b) Temperature and frequency dependence of dielectric constant of $BaTi_{0.82}(Zn_{1/3}Nb_{2/3})_{0.18}O_3$, showing a typical DPT behavior. The measuring frequencies are 1k, 10k and 100kHz.

group (Lecomte, J. and Raveau, B. et.al., 1981, 1982), an American research group (Chang, E.K., Smyth, D.M. and Harmer, M.P., et.al., 1988) and a Chinese research group (Liu, D.H. and Yao, X., 1989) have conducted systematic research on SSN and $A_nB_nO_{3n-1}$ (A=Sr, B=Ti and Fe) or $A_nB_nO_{3n+1}$ (A=Sr, B=Ti and Nb) systems, respectively. These studies have helped to understand the relationship between defect structure, microstructure and electrical properties of complex perovskites. The unique combination of defect chemistry, structural characterization and electrical properties in these investigations indicates that this is a powerful way of understanding the material problems associated with working devices and of developing new materials for device applications.

Unfortunately, very few papers about ferroelectric lead-based materials and their structure related non-ferroelectric relaxor materials in terms of correlation between defect chemistry, microstructure and dielectric properties can be found in the open literature (Hardtl, K.H., et.al., 1972; Atkin, R.B., et.al., 1971; Hennings, D., et.al., 1970). The purpose of this work is therefore to improve the current understanding of the correlation between defect chemistry, microstructure, and dielectric properties of relaxor complex perovskite ceramic materials based on a carefully chosen model system. Since we believe that this study is the first focused attempt to conduct systematic research combining defect chemistry, microstructure and electrical properties in the area of self-compensated complex perovskite materials structurally related to relaxor ferroelectric systems, it is necessarily in the nature of an exploratory study covering a rather wide range of special topics, each of which could form the basis for a full study itself.

Topics which are explored in this work based on the model system $Ba(Zn_{1/3}Nb_{2/3})O_3$ include:

1) Microstructure and microchemical ordering (chapter 3):

   a) TEM studies of stoichiometric BZN and its complex ordering scheme.

   b) TEM (including HRTEM, AEM) studies of nonstoichiometric BZN.

   c) Donor and acceptor doped BZN.

2) Defect structure and transport properties (chapters 4, 5 and 6):

   a) Defect structure study of stoichiometric and doped BZN using high temperature equilibrium electrical conductivity measurement, AEM, and EPMA.

   b) Transport mechanism study using high temperature equilibrium electrical

conductivity, Seebeck coefficient, low temperature AC conductivity, dielectric relaxation, impedance analysis and optical absorption analysis.

c) Development of a defect model and a computer simulation technique that permits modelling of the complete defect structure of BZN.

3) Ferroelectric phase transition (chapter 4):

The focus is on BT co-doped with Zn and Nb with careful composition modification using liquid mixing technique. This system undergoes a ferroelectric to paraelectric transition within the experimental temperature-pressure range where both end members BT and BZN are important ferroelectric and paraelectric materials, respectively.

The author hopes that this work may become the basis for further studies on the relaxor type ferroelectric and non-ferroelectric complex perovskite materials, and also the knowledge gained from this work may be valuable for the improvement of device reliability and development of new materials for device applications. A number of challenging problems which may become accessible to investigation using the approach in this study are delineated in the final chapter.

1.3) *Choice of Model System*

As the first task in the study of defect chemistry, microstructure and dielectric properties of complex perovskite materials, it is necessary to establish logical guidelines for selecting a good model system.

1.3.1) Principles in Selecting a Model System

(1) The model system should be structurally related to relaxor type complex perovskites, such as the systems starting from simple perovskite ABO_3, to the complex $(A'A'')(B'B'')O_3$ perovskites. This system should also be capable of being prepared by either the conventional ceramic route or special processing techniques.

(2) The system must show complex microchemical ordering resulting in compositional fluctuation so that the research results can be directly related to ferroelectric relaxors.

(3) The system should contain components without too much volatility and reducibility so that the high temperature defect and transport measurements can be conducted at elevated temperature and reduced atmospheres.

(4) The system should exhibit a certain degree of nonstoichiometry so that appropriate doping species and levels can be added with observable property differences

8

in order to study the defect structure.

In short, the chosen model system should be typical from both theoretical and experimental points of view. It should be suitable for the application of defect chemistry analysis, microstructural characterization and dielectric measurements, and relatively simple without losing all essential features of relaxor type complex perovskite materials.

1.3.2) Lead-based Systems

Lead-based systems, such as PMN or PZN, could serve as an ideal model system for structural and dielectric studies. The ferroelectric relaxor behavior is attributed to the microchemical ordering (Chen, J., et.al., 1989; Cross, L.E., 1987) due to compositional fluctuation. Compositional adjustments give rise to a change in the degree of ordering. Recent theoretical calculations show that this system can serve as a good model for prediction of microchemical ordering (Zhang, X.W., et.al., 1990a). From a simple perovskite e.g. $PbTiO_3$ (PT) to a complex compound e.g. PMN, a ferroelectric phase is maintained over the entire composition range within the test temperature region. However, the system shows a gradual change from a first order transition to a DPT as the composition becomes richer in PMN. Enormous amounts of research work have been conducted on the relationship between structure, composition and dielectric properties (Cross, L.E. 1987; Jiang, S.J. 1979; Ouchi, H. et.al., 1965). Wide applications for this type of material have been found as optical switches (Glass, A.M., 1988; Smith, P.W., 1988), multilayer capacitors (Herbert, J.M., 1982), pyroelectric sensors (Watton, R., 1986), piezoelectric transducers (Jaffe, B. et.al., 1971), and electrostrictive actuators (Uchino, K., 1987) and ferroelectric thin film non-volatile memory devices (Scott, J.F., et.al., 1989). It is a very interesting class of materials from both theoretical and practical points of view. Unfortunately, some basic problems eliminate it as a model system for comprehensive microstructural and defect chemistry study. First of all, lead volatility and reducibility at high temperature and reduced atmospheres make it difficult to study defect chemistry. Since defect chemistry studies require high temperature equilibrium measurements, loss of cations due to volatility would change the stoichiometry of the studied compound in terms of standard cation/cation and cation/anion ratio. Therefore thermodynamic equilibrium could not be achieved. Second, lead-based systems, e.g. PMN, usually can only tolerate a limited degree of B-site cation nonstoichiometry (in terms of change of cation ratio in reference to the starting formula). In other words, perovskite stability is limited by the cation nonstoichiometry, excess Nb, for instance, would result in the formation of pyrochlore.

9

It is obviously not a good model system for the type of study to be conducted here.

1.3.3) Strontium-based Systems

Strontium-based systems, such as SMN, can have a complex ordered crystal structure. SMN (Gallasso, F., et.al., 1963) is a good model system for studies of microstructural development and defect chemistry. It does not have the volatility problem that lead-based systems have. The parent material $SrTiO_3$ has been investigated extensively because of its practical importance as a base material for boundary layer capacitors, and its theoretical importance as an ideal perovskite for defect chemistry studies. The only drawback is that this system does not show any ferroelectric phase transition within the experimental temperature range (the Curie temperature, Tc(ST)=-233°C). Both $SrTiO_3$ and SMN belong to the cubic paraelectric class. Lack of ferroelectricity makes strontium-based system less attractive to study. In addition, SMN itself does not have practical application. It could be a good model system, but obviously not the best one.

1.3.4) Barium-based Systems

Barium-based systems, especially the parent material BT, is a widely used model material. BT is an excellent representative of the ferroelectric perovskite family. It has been carefully studied in almost every aspect since it was discovered in the mid-forties. There is much information about its processing conditions, crystal structure, domain configuration, phase transition, defect structure, transport and dielectric/electric properties (Jaffe., B., et.al., 1971). Complex perovskites derived from BT, such as BZN, the ferroelectric to paraelectric transition from BT to BZN with Zn and Nb co-doped on the Ti site, usually shift to lower temperatures. This could be interesting in terms of dielectric properties. Furthermore, BZN has a complicated ordered crystal structure that shows a mixture of different types of microchemical ordering. These ordering patterns can be controlled by either adjustment of chemical composition or heat treatment conditions. Since BZN is very refractory (sintering temperature around 1600°C), and Nb can be reduced to quite low oxygen partial pressure, the high temperature equilibrium defect and transport study can also be conducted on this system. Finally, BZN itself possesses rather good high frequency properties and has been used in microwave resonators for satellite telecommunications (Kawashima, S., et.al., 1978). It is therefore fair to say that BT-BZN covers a wide range of research topics, and is an excellent representative for such a comprehensive study of the

interrelationship between defect, transport, microstructural and dielectric properties.

1.3.5) Brief Summary

The main purpose of this study is to gain a comprehensive understanding about the relationship between the defect chemistry, microstructural and dielectric properties of relaxor type ferroelectric and structurally related non-ferroelectric materials. The emphasis is on the defect chemistry and microstructure, since a vast amount of information on the dielectric properties can be found in the open literature. The unique facilities and expertise on microstructural characterization and defect chemistry analysis at Lehigh university make this research work possible. Unfortunately due to the problems of volatility and reducibility of PbO with the lead-based system, as mentioned above, a defect chemistry study could not be carried out. However, as a structurally related non-ferroelectric material, BZN is an analogous system to lead-based relaxor ferroelectric materials in terms of ordered structure and defect chemistry except that it does not show any ferroelectricity within the experimental temperature range. Considering that the defect chemistry study is conducted at high temperatures where most relaxor ferroelectric materials are in their paraelectric state, the BT-BZN system can be considered as a close relative to relaxor ferroelectrics for this type of comprehensive study. It is the best presently available model system for this research project.

1.4) *Microchemical Ordering in Complex Perovskites*

The crystal structure of $A(B'B'')O_3$ type complex perovskites has been tabulated by Galasso (1969). The octahedral B-site cations can be either randomly distributed or ordered. Most reported examples of B-site cation ordering correspond to the general stoichiometric ternary perovskites, such as $A(B'_{1/2}B''_{1/2})O_3$, $A(B'_{1/3}B''_{2/3})O_3$ and $A(B'_{2/3}B''_{1/3})O_3$. The so-called 1:1 (Figure 1.2a) and 1:2 (Figure 1.3a) type of ordered scheme for the ideal perovskite cubic structure can be understood as follows: Considering {111} planes of the cubic perovskite structure (ABO_3), B-site cation planes are stacked perpendicular to the <111> directions with a packing sequence of B:B:B:B....... If the B-site cation layer stacking sequence is $B':B'':B':B''$...... , this leads to 1:1 type ordering: $A(B'_{1/2}B''_{1/2})O_3$ (Figure 1.2b). The cubic unit cell is doubled as shown in Figure 1.2a (after Pauling, L., 1924). If the B-site cation stacking sequence is $B':B'':B'':B':B'':B''$......, this leads to 1:2 type ordering: $A(B'_{1/3}B''_{2/3})O_3$ (Figure 1.3b). As shown in Figure 1.3a (after Galasso, F., et.al.,

11

1961), the ordered unit cell is not a simple triple of the cubic unit cell. The cubic unit cell is slightly distorted, and along the <111> direction of the distorted pseudo-cubic cell, a hexagonal or trigonal unit cell can be constructed. The ordered unit cell is indexed based on trigonal symmetry, but can still be indexed based on the tripled cubic unit cell for some simple and important zone axes. The detailed crystallographic issues will be discussed in the following sections.

The ordering of B site cations in $A(B'_{1/2}B''_{1/2})O_3$ type compounds has been studied extensively (Blasse, G., 1965; Roy, R., 1964; Galasso, F., 1969; Goodnough, J.B., et.al., 1970; Setter, N., 1980). However, not many detailed structural investigations of ordering in $A(B'_{1/3}B''_{2/3})O_3$ systems have been reported (Harmer, M.P., et.al., 1989). In the early sixties, a study of $Ba(B'_{1/3}{}^{+2}Ta_{2/3}{}^{+5})O_3$ compounds showed a decrease in the ordering as the difference in the size of B'^{+2} and Ta^{+5} ions became less (Galasso, F., et.al., 1963a). These results were confirmed in a later investigation for $Ba(B'_{1/3}{}^{+2}Nb_{2/3}{}^{+5})O_3$ compounds (Galasso, F., et.al., 1963b). This is in general true for these type of complex perovskites with $B'^{+2}/B''^{+5} = 1/2$. It has been noted that not all examples where $B'/B''=1/2$ led to genuine 1:2 type of ordering. Some systems have shown 1:1 type of ordering, such as $Pb(Mg_{1/3}Nb_{2/3})O_3$ (Chen, J., et.al., 1989), $Ba(U_{1/3}Fe_{2/3})O_3$ (Padel, L., et.al., 1972), $Ba(W_{1/3}Sc_{2/3})O_3$ (Fresia, E.J., et.al., 1959), and $Sr(Sr_{1/3}Nb_{2/3})O_3$ (Lecomte, J., Raveau, B., et.al., 1981, 1982) etc.. Most of the compounds with the general formula $A(B'_{2/3}{}^{+3}B''_{1/3}{}^{+6})O_3$ possess 1:1 type of ordering (see Appendix I). According to the comprehensive overview that Galasso did forty years ago (Galasso, F., 1969), many $A(B'_{1/3}B''_{2/3})O_3$ type materials (see Appendix II) show a disordered structure based on XRD results. However, a major deficiency of XRD techniques is the detectability of ordered phases with small volume fractions. The TEM technique using electron diffraction with the unique advantage for detecting the ordered phase with small volume fraction has been utilized in materials science for quite a long time (Tanner, L.E., et.al., 1977; Iveronova, V.I., 1977). In the early eighties, Harmer et. al. (1984) first demonstrated this technique to reveal the chemically ordered 1:1 type APBs (anti-phase domain boundaries, see Edinton, J.W., 1975) in PST single crystal. Later on, Chan et. al. (1985), Chen et. al. (1989) and our work demonstrated the possibility to observe small microchemical domains (30~40 Å in size) in quenched PST, PMN and BZN systems, respectively, which were usually recognized as disordered cubic structures based on XRD technique. It is therefore
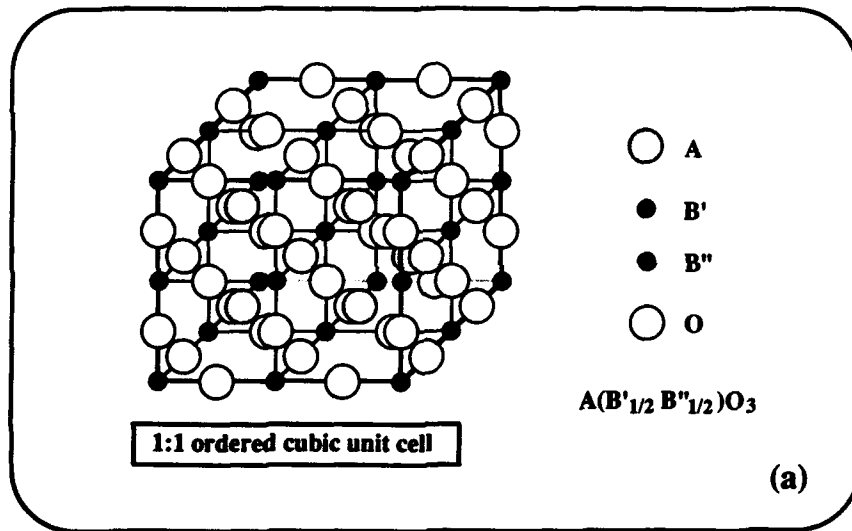
12

Figure 1.2 Schematic of 1:1 type of ordered structure for $A(B'_{1/2}B''_{1/2})O_3$ type of compound. (a) 3D representation.
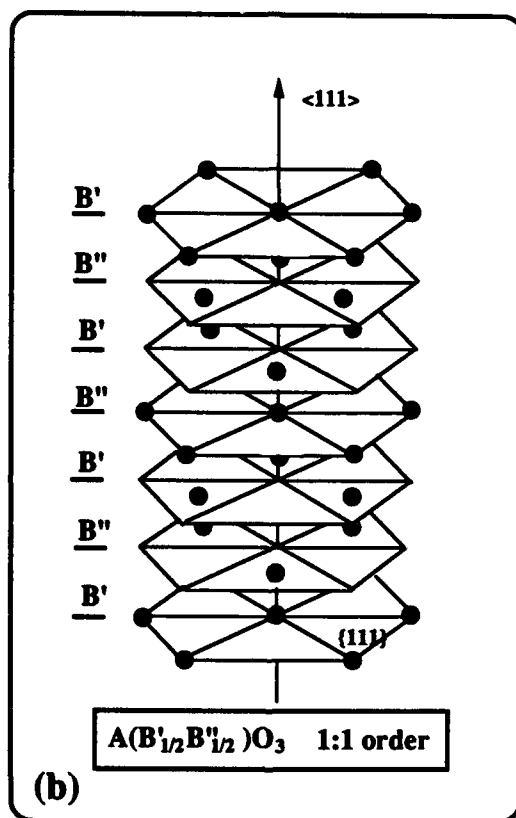
Figure 1.2 Schematic of 1:1 type of ordered structure for $A(B'_{1/2}B''_{1/2})O_3$ type of compound. (b) Cations stacking sequence along <111> direction.
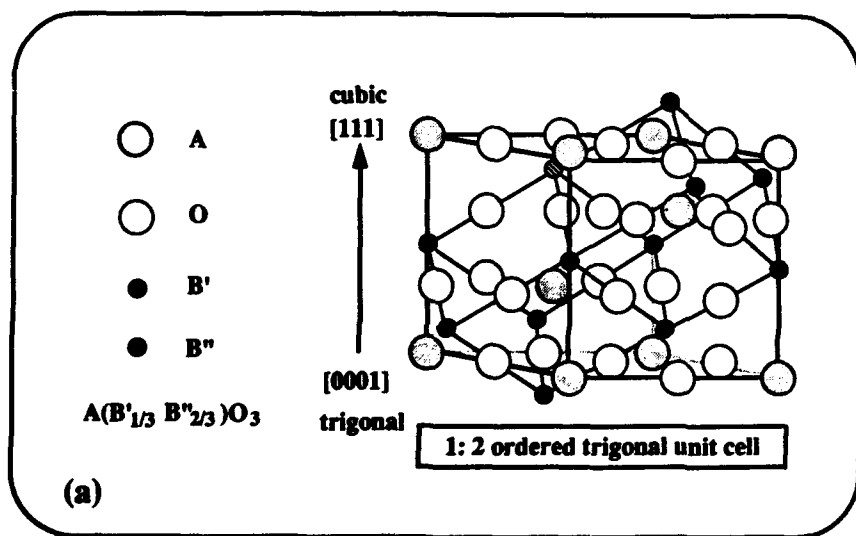
Figure 1.3 Schematic of 1:2 type of ordered structure for $A(B'_{1/3}B''_{2/3})O_3$ type of compound. (a) 3D representation.
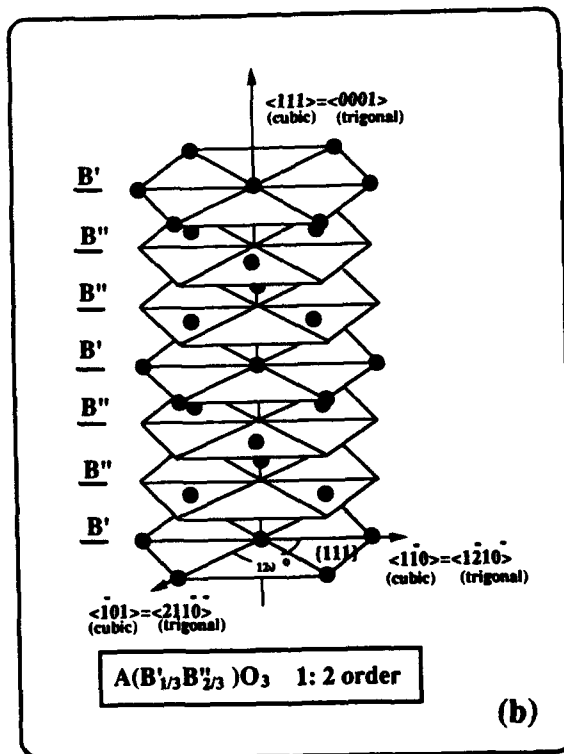
Figure 1.3 Schematic of 1:2 type of ordered structure for $A(B'_{1/3}B''_{2/3})O_3$ type of compound. (b) Cations stacking sequence along <111> direction.

a challenge for Galasso's tabulation whether or not part or all of these $A(B'_{1/3}B''_{2/3})O_3$ compounds show a disordered structure. It is also interesting from both a theoretical and technical viewpoint to ask why 1:1 type ordering appears in 1:2 type compositions. A recently developed concept "atom position probability wave" considers the atom location in ionic crystals as a probability wave (Zhang, X.W., 1990b). This is an analogous concept to a De Broglie wave or phonon wave etc.. The atom location probability in a certain position in a particular crystal system can be calculated based on the wave function, which may give some insight into the complex ordering behavior. Based on this theory, Zhang et. al. (1990a) started predicting the ordering behavior in $A(B'_{1/3}B''_{2/3})O_3$ compounds with 1:1 type ordering and they did meet with some success. On the other hand, from the conventional free energy argument, Zhang et. al. also calculated the electrostatic energy of this system based on the Kikuchi method (Kikuchi, R., 1974). They reached a conclusion that is in fairly good agreement with experimental observation, especially for lead-based relaxor systems. However, for some systems, such as $Pb(Sc_{2/3}W_{2/3})O_3$ (PSW, Raymond, M., 1990) and especially barium-based systems, this theory is not as successful. It is therefore a new challenge for all materials scientists and solid state physicists and chemists to overview all of these $A(B'_{1/3}B''_{2/3})O_3$ type compounds once again. Obviously, extensive theoretical and experimental work is required to clarify this problem.

1.5) *Nonstoichiometry and Defect Chemistry of Perovskites*

It is useful to review perovskites in terms of "perovskite space" as by Smyth, D.M. (1989). This is a three dimensional representation of the compositional and structural relationships of a wide variety of perovskite-related materials. The basic form of perovskite space as proposed by Smyth (Smyth, D.M., 1989) is shown in figure 4.1. It is intended to be a qualitative representation of simple and complex perovskites. Attempts to be completely rigorous generally result in details that obscure the underlying simplicity. The diagram contains two orthogonal axes that lie in the plane of the page. The horizontal axis reflects variations in the oxygen content, and is plotted in terms of the O/A ratio for the generic formula ABO_3. Movement along this line can result from either substitution of aliovalent impurities, i.e. ions of either lesser or greater charge than the ion they replace, or by redox reactions that are also equivalent to changes in the average oxidation number of the cations. The vertical axis, at O/A= 3, allows self-compensating substitutions for either the A ions (upward) or the B ions (downward). For the compositions shown in figure 1.4, it is assumed that A is divalent

17

and B is tetravalent, e.g. $BaTiO_3$. Thus A^{+2} can be replaced by equal amounts of A^{+1} and A^{+3}, while B^{+4} can be replaced by $\frac{1}{2}B^{+3}$ and $\frac{1}{2}B^{+5}$ or by $\frac{1}{2}B^{+2}$ and $\frac{1}{2}B^{+6}$ or by $\frac{1}{3}B^{+2}$ and $\frac{2}{3}B^{+5}$ or by $\frac{1}{3}B^{+6}$ and $\frac{2}{3}B^{+3}$ etc.. In the plane of these two orthogonal axes, the A/B ratio remains fixed at unity. Changes in the A/B ratio are taken into account by a third axis that passes through the plane of the page. It is not perpendicular to the page, because the O/A ratio must also change along this axis. At the origin of the diagram is ABO_3, the ideal, fully-stuffed perovskite composition and structure. It can be shown that the structures of compositions along each of the axes converge systematically toward the ideal perovskite structure as the compositions approach the origin. Properties of practical interest can also be located on such a diagram, as shown in Figure 1.4 (Smyth, D.M., 1989). In the present study, only the area near the "Y" axis in the perovskite space is of interest.

The various systems are quite specific in their tendency to form ordered superlattices and behave differently in defect structure and dielectric properties. For example, PT−PMN (Ouchi, H., et.al., 1965; Jiang, S.J., 1979), BT−BZ (Hennings, D., et.al., 1982; McSweeney, R., et.al., 1987, 1988), ST−SLTC (Parkash, O., et.al., 1990a), BT−CT (Han, Y.H., 1987; Zhang, X.W., et.al., 1987, Timari, P.S., 1989). Numerous research papers covering a wide range of aspects, such as phase transition, electric/dielectric properties, microstructures and defect chemistry can be found in the open literature.

1.5.1) Simple Perovskites

In the current section, the nonstoichiometry in general and defect chemistry of $BaTiO_3$ in particular will be discussed briefly. Detailed review of this subject can be found in Smyth's review papers (1985, 1989). In principle, all crystalline compounds exist over some finite range of composition, rather than being limited to a single, precise atomic ratio. this deviation from the ideal or stoichiometric composition is termed *nonstoichiometry*. The effect is particularly notable in compounds of the transition metals, where more than one oxidation state of the element is chemically stable. Thus cobaltous oxide CoO, tolerates up to about 1 atomic% excess oxygen while retaining the crystal geometry of the rock salt structure of CoO. This reflects the stability of the Co^{+3} oxidation state, and the oxygen excess compositions can be reviewed as solid solutions of Co_2O_3 in CoO. The extent of nonstoichiometry is directly related to the stability of the adjacent oxidation state. For oxides such as Nb_2O_5, Ta_2O_5, and TiO_2, on the other hand, where the lower oxidation states are somewhat stable, small amounts

18
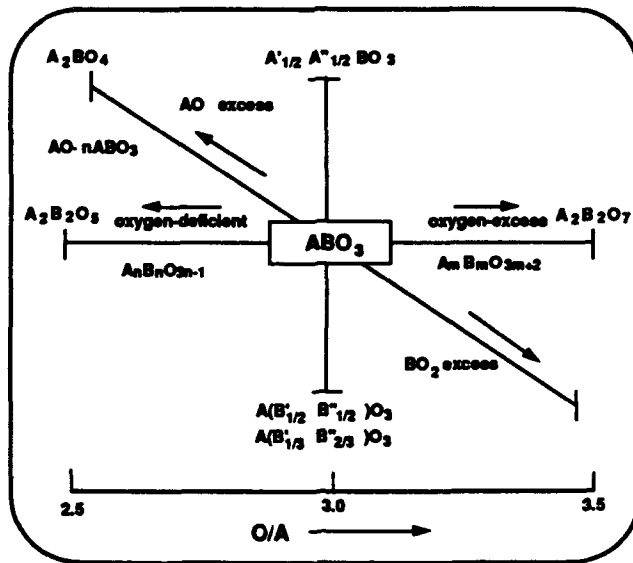
Figure 1.4 Perovskite space (from Ref. Smyth, D.M., 1989).
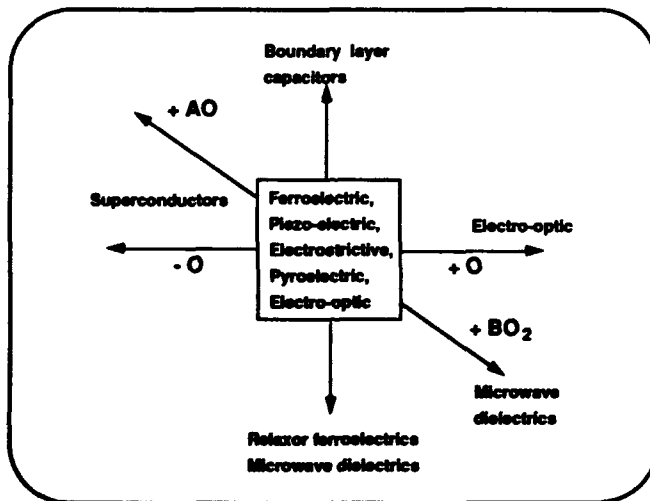
Figure 1.5 Applications in the perovskite space (from Ref. Smyth, D.M., 1989).

19

of oxygen deficiency can be achieved, e.g. the equivalent of a solid solution of Ti_2O_3 in TiO_2. Since the metals in these oxides are in their highest achievable oxidation states, oxygen excess compositions are not expected in the pure compounds.

Small deviations from stoichiometry can be accommodated within the host structure by point defects such as unoccupied lattice positions, vacancies, or ions located in normally unoccupied positions, interstitials. For compounds that can become oxygen deficient, the loss of oxygen commonly leaves unoccupied oxygen sites, oxygen vacancies, and the crystal density decreases. Not only are lattice point defects created by nonstoichiometry, the electronic order is also perturbed. The oxygen in the crystal can be formally considered to be the oxygen ion O^{-2}. When the oxygen leaves the crystal on reduction, it appears in the gas phase as the neutral gaseous species O_2. Not only does the O^{-2} ion leave behind an unoccupied oxygen site in the crystal, it also leaves the two electrons with which it was combined in the ionic form. In the symbolism of defect chemistry (Kröger, F.A. and Vink, H.J., 1956), this reaction is written as

$$O_O = \tfrac{1}{2} O_2 + V_O^{\cdot\cdot} + 2e' \tag{1.1}$$

O_O represents the normal situation of an oxide ion on an oxide lattice position, $V_O^{\cdot\cdot}$ is a vacancy on an oxygen site with two dots denoting the missing ionic charge, thus representing two extra positive charges relative to the ideal crystal. e' is an extra electron with its negative charge. If the electron is not bound by electrostatic attraction to the positively charged $V_O^{\cdot\cdot}$, they will contribute to the electronic conductivity, which will then increase as oxygen is lost from the crystal. The measurement of conductivity is a convenient experimental means of tracking the progress of such a reaction.

In addition to the metal-nonmetal type of nonstoichiometry just described, in a ternary compound such as $BaTiO_3$ there can be deviations in the ratio of the two metallic constituents, i.e. in Ba/Ti. Again the excess components must be accommodated by the creation of defects in the crystalline lattice. Excess BaO could either be inserted into the structure as interstitial ions, $Ba_I^{\cdot\cdot}$ and O_I'' or added in the form of new unit cells that would result in titanium and oxygen vacancies, V_{Ti}'''' and $2V_O^{\cdot\cdot}$. The perovskite structure has no room for large interstitial ions and V_{Ti}'''' represents a large charge or bonding disruption. An extensive range of solubility for excess BaO is thus not expected. The experimentally detected solubility limit is about

200 ppm (molar) level (Hu, Y.H. et.al., 1985). On the other hand, excess TiO_2 can be accommodated by a combination of barium and oxygen vacancies

$$TiO_2 \rightarrow Ti_{Ti} + 2O_O + V_{Ba}'' + V_O^{\cdot\cdot} \qquad (1.2)$$

which are not unreasonable. Sharma, R.K., et.al., (1981) has shown that the tolerance for excess TiO_2 is also extremely limited, being no more than 100 ppm (molar) in $BaTiO_3$. These amounts are not sufficient to have any first order effect on the properties of these compounds.

When an impurity compound is dissolved into a crystalline lattice having a different cation/anion ratio, the solid solution must contain defects. ZnO has a larger cation/anion ratio than TiO_2, i.e. the cation has a smaller positive charge, and thus it is classified as an acceptor impurity. Since ZnO brings in fewer anions per cation than can be accommodated by the TiO_2 lattice, it is reasonable to expect the solid solution to contain oxygen vacancies

$$ZnO \xrightarrow{TiO_2} Zn_{Ti}'' + O_O + V_O^{\cdot\cdot} \qquad (1.3)$$

Zn_{Ti}'' represents Zn^{+2} on a Ti^{+4} site, the charge discrepancy being explicitly noted in the superscript. In the case of $BaTiO_3$, one can consider the addition of ZnO along with an equivalent amount of BaO to keep the Ba sub-lattice filled

$$BaO + ZnO \rightarrow Ba_{Ba} + Zn_{Ti}'' + 2O_O + V_O^{\cdot\cdot} \qquad (1.4)$$
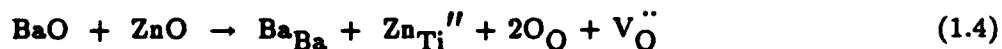
Donor impurities are cations with higher positive charge than the cation they replace, e.g. Nb_2O_5 substituted for TiO_2 in $BaTiO_3$. In an oxidizing atmosphere, the extra oxygen in the impurity oxide might be accommodated interstitially, or it might create new lattice sites with resulting V_{Ti}'''' and/or V_{Ba}''. Neither of these options is very favorable, and for small impurity concentrations ($\lesssim 0.5$ mol%), the extra oxygen is expelled from the crystal, leaving behind its extra electrons relative to the neutral atom (Chan, N.H., et.al., 1984)

$$2BaO + Nb_2O_5 \rightarrow 2Ba_{Ba} + 2Nb_{Ti}{}^{\cdot} + 6O_O + \tfrac{1}{2}O_2 + 2e' \qquad (1.5)$$
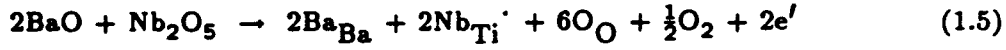
The impurity-related electrons impart n-type semiconduction to $BaTiO_3$ in the specified concentration range.

With the background in defect chemistry reviewed above, it is now possible to discuss the defect model and related effects of nonstoichiometry and impurities on the electrical conductivity of $BaTiO_3$. A convenient model plot with Log(relative concentration) versus Log(oxygen partial pressure) is shown in figure 1.6. The different regions in the diagram correspond to the following redox (reduction/oxidation) reactions:

At the stoichiometric
composition:

$$nil = e' + h^{\cdot} \text{ (electronic disorder)} \qquad (1.6)$$

$$n = p \qquad (1.6)'$$

$$nil = V_{Ba}{}'' + V_{Ti}{}'''' + 3V_O{}^{\cdot\cdot} \text{ (Schottky disorder)} \qquad (1.7)$$

$$2[V_{Ba}{}''] + 4[V_{Ti}{}''''] = 2[V_O{}^{\cdot\cdot}] \qquad (1.7)'$$

Here the Schottky disorder is assumed to be a major type.

Reduction:

$$O_O \rightarrow \tfrac{1}{2}O_2 + V_O{}^{\cdot\cdot} + 2e' \qquad (1.1)$$

$$2[V_O{}^{\cdot\cdot}] = n \qquad (1.1)'$$

Oxidation:

$$\tfrac{3}{2}O_2 \rightarrow 3O_O + V_{Ba}{}'' + V_{Ti}{}'''' + 6h^{\cdot} \qquad (1.8)$$

$$2[V_{Ba}{}''] + 4[V_{Ti}{}''''] = p \qquad (1.8)'$$

It is well known that undoped $BaTiO_3$ contains unavoidable "naturally occurred impurities" at the ppm level (Chan, N.H., et.al., 1981a). Those impurity cations are mostly acceptor type, such as Al^{+3}, Mg^{+2}, Ca^{+2}, Zn^{+2}, etc., due to their natural abundance, and they make the undoped BT behave like an acceptor doped material (e.g. with $[Zn_{Ti}{}''] = [V_O{}^{\cdot\cdot}]$). Therefore, the starting oxygen vacancy level is relatively higher than the metal vacancy concentration and oxidation can then take place by the filling of extrinsic oxygen vacancies.

Oxidation:

$$\tfrac{1}{2}O_2 + V_O{}^{\cdot\cdot} \rightarrow O_O + 2h^{\cdot} \qquad (1.9)$$

22
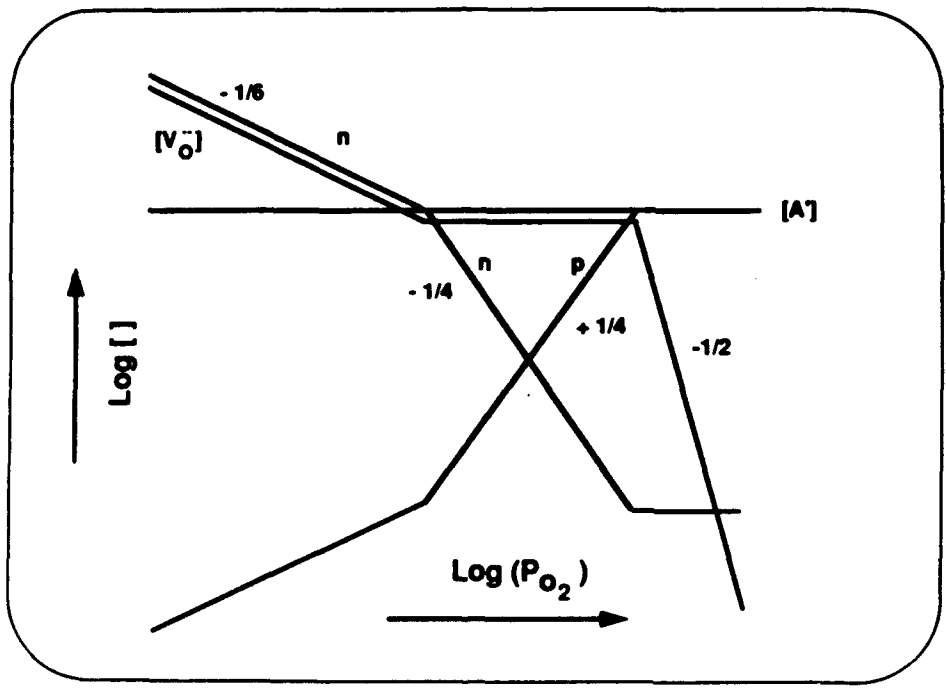
Figure 1.6 Schematic of defect model for BT. Only the majority defects in the testing oxygen partial pressure range are drawn.

$$2[V_O^{\cdot\cdot}] = p \qquad\qquad (1.9)'$$

Here the concept of "naturally occurred impurities" and $V_O^{\cdot\cdot}$ proposed by Smyth (Chan, N.H. and Smyth, D.M., 1981) is used instead of $V_O^{\cdot}$ because the energetics are unfavorable for $V_O^{\cdot}$ (Chan, N.H., et.al., 1981; Catlow, C.A.R., et.al., 1986). The overall charge neutrality condition for majority defects is

$$2[Zn_{Ti}''] + n = 2[V_O^{\cdot\cdot}] + p \qquad\qquad (1.10)$$

By applying the dilute solution thermodynamic mass action law to the above reactions (1.1) and (1.6) through (1.9), one obtains

$$K_i = np = K_i' \exp(-E_g^{(o)}/kT) \qquad\qquad (1.11)$$

$$K_s = [V_{Ba}''][V_{Ti}''''][V_O^{\cdot\cdot}]^3 = K_s' \exp(-\Delta H_s/kT) \qquad\qquad (1.12)$$

$$K_R = \frac{[V_O^{\cdot\cdot}]\, n^2\, P_{O_2}^{1/2}}{[O_O]} = K_R' \exp(-\Delta H_R/kT) \qquad\qquad (1.13)$$

$$K_O = \frac{[O_O]\, p^2}{[V_O^{\cdot\cdot}]\, P_{O_2}^{1/2}} = K_O' \exp(-\Delta H_O/kT) \qquad\qquad (1.14)$$

Where K_i, K_s, K_R and K_O are mass action constants of intrinsic electronic, Schottky, reduction and oxidation, respectively. Square brackets denotes the concentration of the enclosed species, and n and p are electron and hole concentrations, respectively. $E_g^{(o)}$ is the indirect band gap at 0 K. ΔH_R and ΔH_O are the enthalpies of reduction and oxidation, respectively. P_{O_2} represents oxygen partial pressure. Other parameters have their usual meanings.

For isothermal conditions, the relative concentration of various defects as a function of P_{O_2} can be divided into various regimes where different approximations to the electro-neutrality condition dominate as follows:

(1) near the stoichiometric point, n = p and $[Zn_{Ti}''] = [V_O^{\cdot\cdot}]$ (fixed value only depending upon the doping level)

24

$$n \propto P_{O_2}{}^{-1/4} \tag{1.15}$$

$$p \propto P_{O_2}{}^{1/4} \tag{1.16}$$

(2) at low oxygen partial pressure, increasing of $[V_O^{\cdot\cdot}]$ due to reduction(2.1) reaches the $[Zn_{Ti}{}'']$, then $p \ll n = 2[V_O^{\cdot\cdot}] > 2[Zn_{Ti}{}'']$

$$n \propto P_{O_2}{}^{-1/6} \tag{1.17}$$

$$p \propto P_{O_2}{}^{1/6} \tag{1.18}$$

$$[V_O^{\cdot\cdot}] \propto P_{O_2}{}^{-1/6} \tag{1.19}$$

Since ideally pure BT does not contain oxidizable ions, there is no chance for excess oxygen to be accommodated into the crystal. The short p-type (oxidation) wing in the figure 1.6 is due to the acceptor doping. Figures 1.7 and 1.8 show the acceptor and donor doped cases, respectively that have been proven correct by both this experimental work and many others (see review papers by Smyth, D.M., 1984, 1989). For the heavily donor doped case, electronic compensation switches to an ionic compensation mechanism, a detailed discussion will be dealt with in chapter 4.

1.5.2) Self-compensated Complex Perovskite

In this section, the author will trace the progress of defect chemistry of self-compensated complex perovskites to the present state of understanding. As more data were gathered and more investigations were conducted on various systems, a consistent and quantitative picture of the defect structure of this type of compound will become much more clear. It is therefore expected to benefit the improvement of reliability of working devices and the development of new materials for device applications.

Defect chemistry of general complex perovskites has been reviewed extensively by Smyth, D.M. (1985, 1989). However, at present, very little work on the defect chemistry of self-compensated complex perovskites appears in the open literature. Since the cation substitutions are fully compensated, and no other defects are generated, the defect chemistry of this type of complex system is usually believed to be that of a simple perovskite. For compounds not involving transition metal ions or involving those ions

25
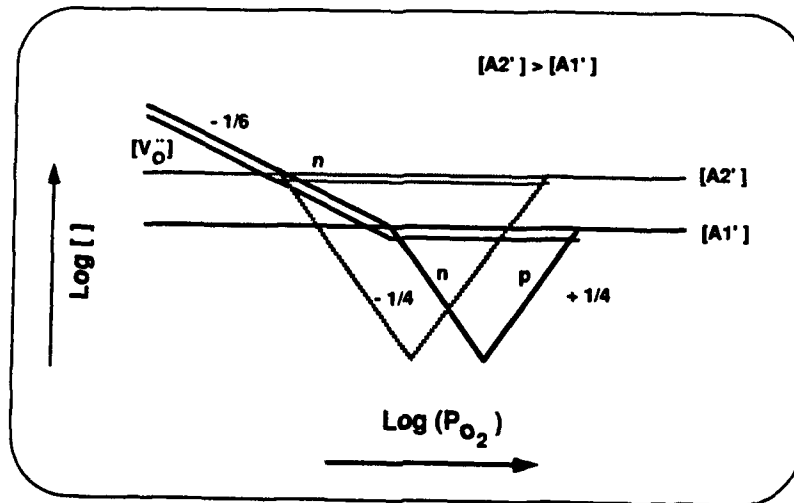
Figure 1.7 Schematic of defect concentration as a function of P_{O_2} for acceptor-doped BT.
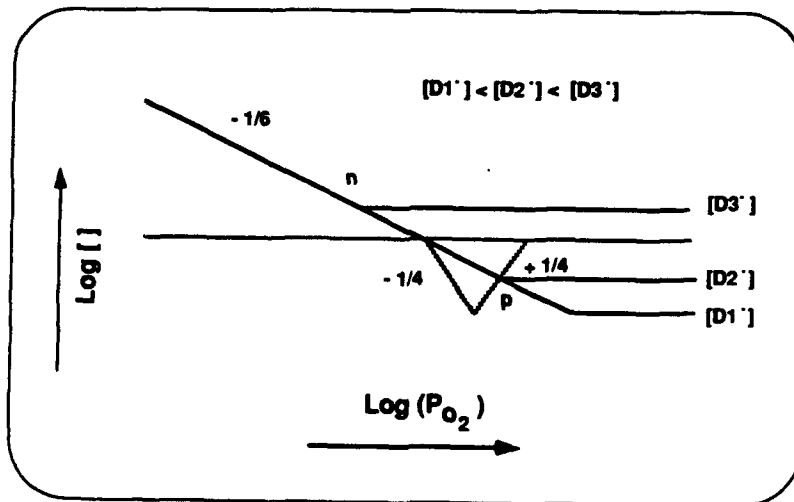
Figure 1.8 Schematic of defect concentration as a function of P_{O_2} for lightly donor-doped BT.

26

with lower redox activity compared with the cation replaced, this is generally true. For example, in the case of the simple perovskite BT and its derivative $(Ba_{1/2}Sr_{1/2})(Ti_{1/2}Zr_{1/2})O_3$, there is not much difference in terms of defect structure. A recent defect chemistry study on the self-compensated lead-based complex perovskite PMN performed by Uchikoba, F. et.al. (1989) and Kato, J. et.al. (1989) provides another example for this argument (Figure 1.9). Although this brief report does not contain any details, it indicates that the general principle does apply to those systems. Nevertheless, two points are worth mentioning here. One point concerns the system in which A and B cations can switch positions. This usually leads to the complex ordering phenomena due to the large difference between the ionic radii of the cations normally located in the six-coordinated B-site and twelve-coordinated A-site. The full understanding of defect chemistry of this type of compound is therefore a structure related matter. The other point is associated with the system consisting of transition metal ions with high redox activity, such as Cr, Fe, Co, Ni, Cu etc.. The multi-stable valence state of these cations would result in rather an interesting change in terms of defect structure comparing with that of the simple perovskite (for a comprehensive study, see Hägemann, H.J., 1980).

An infrared spectroscopy study by Griffiths, A.J. et. al.(1980) indicated that Ba^{+2} partially occupies the octahedral sites in such compositions as $Ba(Sr_{1/2}U_{1/2})O_3$ and Sr^{+2} partially occupies the octahedral sites in $(Ba_{1/2}Sr_{1/2})(Ca_{1/2}U_{1/2})O_3$. The exchange of Sr^{+2} and Ca^{+2} between A and B sites was estimated at 10~25%. This extreme situation does not often occur in other compositions. Some related studies conducted by Zhang, X.W. et.al., (1987) and Takada, K. et.al., (1987) involve the ability of cations to occupy either the six-coordinated B-site or twelve-coordinated A-site. For those cations with intermediate ionic radius, such as Ca and Er, the occupancy probability in BT depends on the Ba/Ti ratio. It is therefore reasonable for A and B cations to switch position in the self-compensated complex perovskite consisting of those cations as charge compensation species.

One interesting example is a work carried out on the defect chemistry of the system $Sr(Sr_{1/3+x}Nb_{2/3-x})O_{3-3/2x}$ with $0 \leqq x \leqq \frac{1}{6}$ (Lecomte, J., et. al., 1981 a, b; 1982). For the composition with $x = 0$, the octahedral sites are in planes of two types: B' and B''. The B'' planes contain only Nb^{+5}, while the B' planes contain Sr^{+2} and the rest of Nb^{+5}. This configuration was first proposed by Steward and Booksby (1951) to interpret the 1:1 type ordering for complex perovskites with general formula

$A(M_{1/3}{}'M_{2/3}{}'')O_3$. The end member SSN (x=0) corresponds to a self-compensated composition on the "Y" axis in the perovskite space (Figure 1.4). An interesting point is that the authors proposed a modified Schottky disorder model in this system. Normal Schottky disorder would correspond to

$$nil = V_{Sr}{}'' + (\tfrac{1}{3}V_{Sr}{}'' + \tfrac{1}{6}V_{Nb}{}''''')_{B'} + (\tfrac{1}{2}V_{Nb}{}''''')_{B''} + 3V_o^{\cdot\cdot} \quad (1.20)$$

Since A site Sr^{+2} can switch to the B' site, this process then ends up with no vacancy on the octahedral sites by adding one Sr into the lattice B site position and assuming disorder in the crystal at high temperature.

$$Sr_{Sr} = 2V''_{Sr} + (\tfrac{1}{3}Sr_{Sr} + \tfrac{2}{3}Sr_{Nb}{}''')_B + 3V_o^{\cdot\cdot} \quad (1.21)$$

Based on this argument, ignoring the unavoidable acceptor impurity effect, the experimentally observed flat bottom of conductivity for SSN can then be attributed to the increasing concentration of oxygen vacancies which give rise to high ionic conductivity. In spite of the quantitative estimation of Schottky disorder energy which is rather too small for this system (4.0 eV), compared with the other perovskites (Catlow, C.R.A., et.al., 1986), this defect chemistry analysis seems quite logical. If this model is appropriate, the modified Schottky disorder built into the crystals during the sintering process may be frozen in at the lower temperatures. This indeed explains the observed high portion of ionic conductivity and weaker ordering behavior. However, other factors are also worth mentioning here, such as the naturally occurred acceptor impurities or the uncertainty of A/B ratio due to processing. These may be the other sources that are responsible for the part of oxygen vacancies for the stoichiometric SSN composition.

For solid solutions with x>0, the Sr/Nb ratio steadily increases in the B' planes. Electron diffraction studies suggest some ordering of the two species on the B' planes which will be discussed in Chapter 3 as a possible ordering pattern. For example, when x= $\tfrac{1}{6}$, the system becomes $Sr(Sr_{1/2}Nb_{1/2})O_{2.75}$, 1:1 type ordering is expected. On the other hand, for x>0, the material is increasingly acceptor doped with $xSr_{Nb}{}'''$ (relative to x=0) on the B' planes, compensated by $\tfrac{3}{2}x$ oxygen vacancies, i.e. $3[Sr_{Nb}{}'''] = 2[V_o^{\cdot\cdot}]$. The high temperature equilibrium conductivity (Figure 1.10) can be explained based on

28

Equations 1.1 and 1.9 perfectly.

This study illustrates the necessity of combining insight into structural details with the concepts of defect chemistry in order to fully understand the behavior of this type of self-compensated complex perovskite. Moreover, the basic defect chemistry model for the simple parent phase perovskite $SrTiO_3$ can be directly applied toward the complex system.

On the other hand, if a self-compensated complex perovskite involves transition metal cations with multi-stable valence states as mentioned above, the defect chemistry is not as simple. High temperature equilibrium conductivities for a series of samples with the general formula $(Sr_{1-x}La_x)(Ti_{1-x}M_x)O_3$ (M = Cr, Co, Ni) with x = 0.1 are shown in Figure 1.11 (Parkash, O., et.al., 1990b). In this case, self-charge compensation requires M to be M^{+3}. It is apparent that a simple defect model cannot cover all of these compositions. If a dopant cation changes its valence state from which the self-charge compensation holds, there will no longer be self-charge compensation. The distinguishing features for each case are obviously attributed to the transition metal ion "M". For self-compensated complex perovskites involving transition metal cations with multi-stable valence states, the defect chemistry is not the same as for simple perovskite (Hägemann, H.J., 1980; Parkash, O., et.al., 1990b).

1.6) *Electrical Transport Mechanism*

In this section, we are now briefly reviewing the theoretical background and characterization techniques for electrical transport mechanism in semiconducting ceramic materials.

The transport properties of any material are obtained by imposing one or more thermodynamic forces, such as an external electric or magnetic field or a temperature gradient, across a sample and then measuring the resulting flows of electric current and heat. The simplest effects are the direct ones: the electrical current arising from an electric field, which gives the electrical conductivity σ; and the heat flow due to temperature gradient, which yields the thermal conductivity κ. Cross-effects include the thermoelectric power (Seebeck coefficient) α and Hall coefficient R_H. These transport coefficients are important because they can be used to either verify theoretical predictions or set values on important parameters which are useful in estimating some of the other properties of the solids.

29
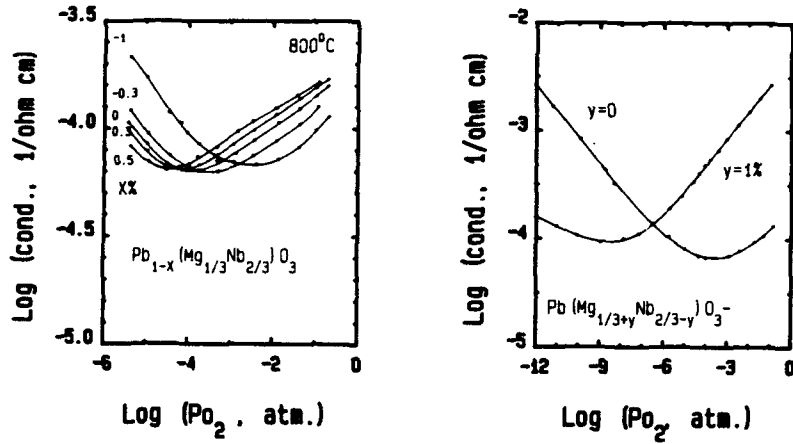
Figure 1.9 Dependance of composition ratio on equilibrium electrical conductivity: (a) A/B ratio, (b) Mg/Nb ratio (from Ref. Uchikoba, F., et.al., 1989).
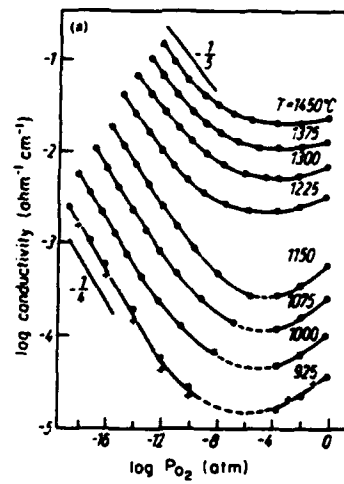
Figure 1.10 equilibrium electrical conductivity of $Sr(Sr_{1/3}Nb_{2/3})O_3$. (from Ref. Lecomte, I.J., et.al., a, 1981).
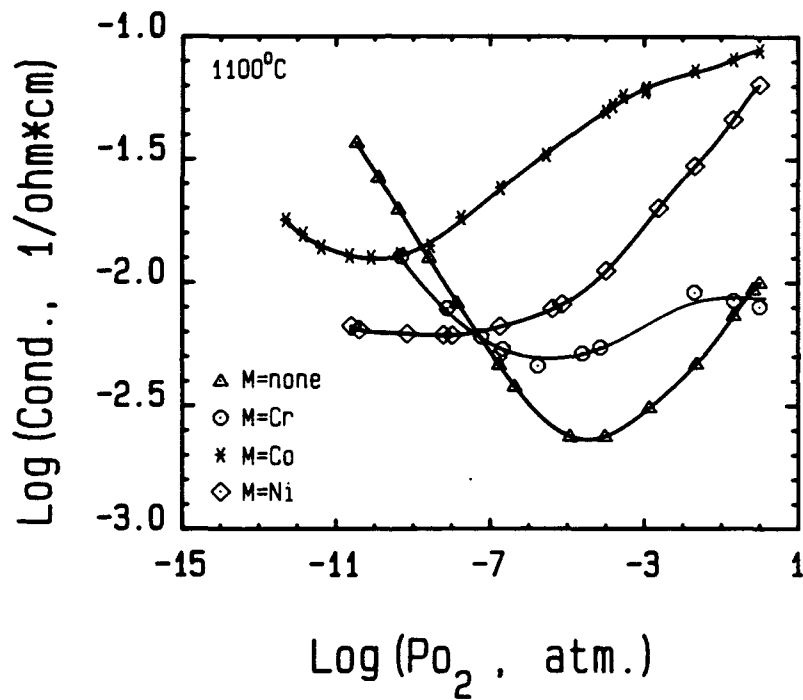
Figure 1.11 High temperature equilibrium conductivity as a function of P_{O_2} for samples $(Sr_{1-x}La_x)(Ti_{1-x}M_x)O_3$ (M = Cr, Co, Ni) with x = 0.1. Noticing that the conductivity profile changes with different dopant ion M (from Ref. parkash, O., et.al., 1990b).

31

The most significant transport coefficient for these purposes is the electrical conductivity. Microscopically, electrical current results only from the flow of charged particles in an applied electric field; thus, in a solid the conductivity must be either ionic or electronic. In most of cases (Kittel, C., 1986), the conductivity can be expressed microscopically as

$$\sigma = \sum_{i}^{m} n_i q_i \mu_i \qquad (1.\,22)$$

where n_i is the number of particle i of the charge q_i per unit volume available to flow in the applied field and μ_i is the average velocity per unit field attained by these particles. m represents that if there are m conduction mechanisms, we must sum their contributions to σ. The importance of Equation (1.22) is that it relates a macroscopically measurable quantity σ to a microscopic parameter μ which can often be calculated. The parameter μ is called the microscopic mobility.

Charge carrier conduction consists of two basic types: ionic and electronic conduction. In many cases, ionic conduction, which is the motion of ions in an applied electric field, is usually negligible compared to electronic conduction for several reasons. Since ions are generally about 10^5 times as massive as electrons, the velocities that ions reach at any given energy are lower by a factor of 10^2-10^3 compared to those of electrons; thus ionic mobilities are correspondingly low, and rarely exceed $10^{-3} cm^2/V$-sec. (Adler, D., 1975). Furthermore, ions can move through the solid only by means of lattice defects whose mobility depends on the crystal structure and transport mechanism. In some cases, such as in perovskite structures, cation diffusion is very difficult (Buessem, W.R., et.al., 1971). Generally speaking, electronic conduction is dominant at sufficiently high temperatures for perovskite materials. There are two kinds of electronic charge carries: nearly-free charge carriers and charge carriers bound to centers (Kittel, C., 1986). Electronic conduction associated with nearly-free charge carriers is termed band type conduction and bound charge carrier conduction is usually referred to as hopping conduction.

For a pure stoichiometric oxide/non-oxide compound, the band type conduction usually deals with nearly-free electrons/holes transport (Bube, R.H., 1974). Electrical current consists of nearly-free electrons/holes flow through conduction/valence band under an external electric field. A detailed definition and discussion about this type of

32

electrical conduction can be found in any standard solid state physics text book (Kittel, C., 1986; Bunget, I., et.al., 1987; Mott, N.F., et.al., 1940, 1979; Wimmer, J.M., et.al., 1975 and Bube, R.H., 1974). One characteristic of this type of conduction is that there is no extra energy needed for electrons (holes) to move through the energy band except for the formation energy of those charge carriers. In the case of degenerate semiconductors (also called metallic type conductors), the electron concentration is fixed (10^{22} to 10^{23} nearly-free electrons/cm^3), and there is no energy of formation. Some transition metal oxides, such as CrO_2, VO, TiO, and ReO_2, behave this way (Adler, D., 1975). In the more usual case, there is an energy band gap Eg between the filled and empty bands which is appreciably greater than kT. The concentration of conduction electrons/holes therefore has an Arrhenius relationship with energy of formation Eg (Kittel, C., 1986).

$$n = p = 2(\frac{2\pi kT}{h^2})^{3/2}(m_e{}^*m_h{}^*)^{3/4} \exp(-\frac{Eg}{2kT}) \tag{1.23}$$

Where h is Planck's constant and $m_e{}^*$ and $m_h{}^*$ are the effective masses of the electron and hole that depend on the strength of the interaction between electrons or holes with the lattice. The effective masses may be larger or smaller than the rest mass (m^o) of an electron depending upon the above interactions. For impurity dominant conduction, e.g. a donor center in the forbidden gap, the charge carrier concentration is determined by (Kittel C., 1986)

$$n \cong 2(\frac{2\pi m_e{}^*kT}{h^2})^{4/3}N_d{}^{1/2} \exp(-\frac{E_d}{2kT}) \tag{1.24}$$

where N_d is the concentration of donors and E_d is donor energy level below the conduction band edge. Only when $kT<<E_d$, electrons are trapped at donor centers. However, once the electrons are released from donor centers, they move under the external electrical field without any additional thermally activated energy. The drift mobility of this type of charge carrier only depends on two types of scattering factors which are lattice and impurity scattering. The total mobility is (Wimmer, J.M., 1975; Bube, R.H., 1974):

$$\mu = [\frac{1}{\mu_T} + \frac{1}{\mu_i}]^{-1} \tag{1.25}$$

33

and $\quad \mu_T = \mu^o{}_T T^{-2/3}$,

where $\mu^o{}_T$ is a constant, μ_T is generally predominant at high temperature; (1.25a)

and $\quad \mu_I = \mu^o{}_I T^{2/3}$,

where $\mu^o{}_I$ is a constant, μ_I is generally predominant at low temperature. (1.25b)

Where μ_T is due to lattice vibrations (phonon) and μ_I is from the distortion of the periodicity of the lattice due to the presence of an impurity. The mobility of this type is obviously not thermally activated.

The electrical conduction for bound charge carriers, on the other hand, requires both energies for formation and motion of the charge carriers moving under the external electric field. A thermally activated mobility is therefore observed. In the host lattice, where there is an interaction between the electrons and lattice, there is a polarization of the lattice associated with the presence of electronic carriers. Electronic carriers can therefore minimize their energy by introducing this lattice polarization. This associate consisting of the electronic carrier plus its polarization field (or distorted lattice, in other words) can be considered as a quasi-particle, and is referred to as a *polaron* (Kittel, C., 1986). A polaron clearly has a lower energy than an electron alone, but it has a larger effective mass since it must carry its lattice distortion with it as it moves. When the associate is weak or the lattice distortion is over a dimension larger than the lattice parameter, this case is termed a large polaron. Conductivity is similar to nearly-free electrons in the band type conductors except for two things: (a) large effective mass; (b) thermally activated mobility with small activation energy on the order of kT which is required by an electron to move along with a weakly polarized lattice under the external electrical field. This motion energy is so small that the pre-exponential term is dominant. When the electronic carrier plus the lattice distortion has a linear dimension smaller than the lattice parameter, it is referred to as a small polaron, and the mobility is strongly affected by the lattice distortion which must move along with the electronic carrier. This process is then often referred to as the hopping mechanism because the electronic carrier is bound or localized at specific lattice sites and can only move from one distorted lattice site to another by overcoming an energy barrier, ΔH_m. Electrical conductivity resulting primarily from small polaron motion is represented by (from Equations (1.22), (1.23) and (1.24)):

$$\sigma \propto n\mu \propto \exp \left[\left(- \frac{Eg}{2kT}\right) + \left(- \frac{\Delta H_m}{kT}\right) \right] \qquad (1.26)$$

There are quite a few techniques for the study of electrical transport properties; such as electrical conductivity and Seebeck coefficient; TGA; Hall coefficient; DC/AC conductivity; complex plane impedance analysis; dielectric relaxation and optical absorption.

Review of these techniques can be found in the open literature (Blumenthal, R.V., et.al., 1974; Bosman, A.J., et.al., 1970; Elliott, S.R., 1987). In the present study, the combination of high temperature equilibrium DC conductivity and Seebeck coefficient, low temperature AC conductivity, complex plane impedance analysis, dielectric relaxation, and optical absorption have been used to study the electrical transport of the model system BZN. We will briefly review only the related techniques instead of going through a lengthy discussion of all the transport characterization techniques.

Seebeck coefficient, also called thermoelectric power, is defined as (Wimmer, J.M., et.al., 1974)

$$\alpha = \frac{dV}{dT} \qquad (1.27)$$

when measured under the experimental conditions of zero current flow through the specimen. If α is taken as

$$\alpha = - \frac{V_h - V_c}{T_h - T_c} \qquad (1.28)$$

where $V_h - V_c$ and $T_h - T_c$ are the emf and temperature differences between the hot and cold ends of the specimen, then the sign of the charge carrier corresponds to the sign of α.

For a single charge carrier type, α can be written as (Mott, N.F., et.al., 1979)

$$\alpha = \pm \frac{k}{e}\left(\frac{E_F}{kT} + A\right) \qquad (1.29)$$

35

where E_F is the Fermi energy measured relative to the transport level and A is an energy-transport term. For a nondegenerate semiconductor where Boltzmann statistics can be applied, Equation (1.29) has the form (Mott, N.F., et.al, 1979; Wimmer, J.M., et.al, 1974)

$$\alpha = \pm \frac{k}{e}(Ln\frac{n_o}{n} + A) \tag{1.30}$$

where n is the charge carrier concentration and n_o the effective density of states at the transport level. Thus the determination of the free charge carrier concentration from the thermal-emf measurement requires the knowledge of both the effective density of states n_o and the transport energy term A. In addition, the determination is rather insensitive because of the logarithmic relation between α and n. These disadvantages are partially compensated by the fact that it is generally easier to make accurate Seebeck coefficient measurements than to measure concentration changes by thermal gravimetric analysis (TGA) technique.

In order to determine the value for n_o and A, two extreme cases can be distinguished. In the case of band type or large polaron conduction, if it is assumed that the charge carrier scattering is by an acoustic phonon in a broad band having a spherical energy surface (Mott, N.F., et.al., 1979)

$$n_o = 2(\frac{2\pi m^* kT}{h^2})^{3/2} = 4.835*10^{15}(\frac{m^*}{m_o}T)^{3/2} \ (cm^{3/2}) \tag{1.31}$$

and AkT is the kinetic energy of the charge carrier with A=2. This is the large polaron/band type conduction case. For the small polaron case, the conduction band is narrow enough that all available states are included in an interval of the width kT. Now the density of states is one per available site for a charge carrier, and can be calculated from the number of available sites per unit cell and unit cell dimension (i.e. $n_o=$ # of available sites per unit cell/unit cell volume). For a very narrow polaron band, the kinetic energy of the charge carrier is much smaller than kT and $A\cong0$. However, since this analysis is somewhat crude, it should not be used to obtain an activation energy which is on the order of kT.

Another powerful technique for the study of charge carrier transport is AC

conductivity and dielectric relaxation (Mott, N.F., et.al., 1979; Bossman, A.J., et.al., 1970). Three cases are shown in figure 1.12. Case (a) represents a transport by carriers excited to the extended states near Ec or Ev. For this band type conduction, the Drude equation (Mott, N.F., et.al., 1979) applies

$$\sigma(\omega) = \sigma(0)/(1 + \omega^2\tau^2) \tag{1.32}$$

The relaxation time τ will however be very small ($\sim10^{-15}$s.) and a decrease in $\sigma(\omega)$ as ω^{-2} (i.e. free-carrier absorption) is not expected until a frequency $\sim10^{15}$ Hz is reached. The σ_{AC} is thus independent of frequency in the low frequency range (e.g. 10 - 10^6 Hz). Case (b) is transport by carriers exited into the localized states at the edges of the conduction or valence band (non-degenerate state). Because transport here is by hopping, $\sigma_{AC} \propto \omega\{\ln(v_{ph}/\omega)\}^4$, i.e. approximately as ω^s where $0<s<1$ if $\omega<<v_{ph}$; v_{ph} is lattice vibration frequency. The temperature dependence of this component of the σ_{AC} should be the same as that for the σ_{DC}. Taking electrons as an example, both σ_{AC} and $\sigma_{DC} \propto \exp\{-(E_c+E_d-E_F+\Delta H_m)/kT\}$. Case (c) is hopping transport by carriers with energies near the Fermi level (degenerate state). The σ_{AC} again should increase with frequency in the same manner as for the process (b). However, the exponential dependence on the temperature will be absent, and $\sigma(\omega)$ should be proportional to T, if kT is small compared to the width of the occupied part of the defect band; and independent of T otherwise.

Since polaron nature represents a charge carrier and a bound center, a dielectric relaxation process can occur because of the orientation polarization of the "dipole" formed by the bound charge carrier with each center. Standard Debye type relaxation theory may apply (Bossman, A.J., et.al., 1970; Bunget, I., et.al., 1987). In sufficiently dilute systems, it is characterized at a certain temperature by a single relaxation time, which in general depends on the type of dopant species, but is independent of the dopant concentration. In non-dilute systems, the interface between centers leads in general to a broadening of the relaxation time temperature or frequency spectrum. Moreover, in compensated non-dilute systems, movement of a "bound" charge carrier from an occupied to a neighboring unoccupied center leads to a relaxation process characterized by a broad spectrum of relaxation times, corresponding to the distribution of distances between such pairs of centers. The Debye type relaxation can be expressed as (Bunget, I., et.al., 1987; Frölich, H., 1986)

37
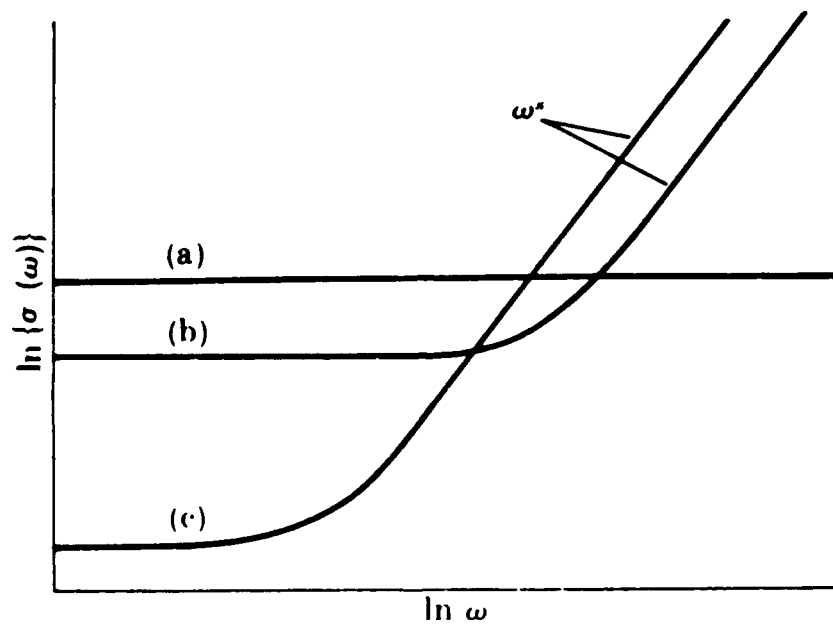
Figure 1.12 Schematic illustration of the frequency dependence of conductivity for the three modes of conduction described in the text (from Ref. Mott, N.F., et.al., 1979).

$$\tau = \tau_o \exp(\Delta H_m / kT) \tag{1.33}$$

Based on an Arrhenius plot of the dissipation factor or ϵ'' peak frequency, the hopping energy ΔH_m can be obtained.

Using complex plane impedance analysis, we can also get σ_{DC} at the same time. There are four types of parameters that can be used in this type of analysis. They are

* Complex impedance (e.g. for simple RC network):

$$Z^* = Z' + jZ'' = \frac{R_p}{1 + \omega R_p^2 C_p^2} + j \frac{\omega R_p^2 C_p}{1 + \omega^2 R_p^2 C_p^2}; \tag{1.34}$$

* Complex admittance (for simple RC network):

$$Y^* = Y' + jY'' = \frac{\omega^2 C_s^2 R_s}{1 + \omega R_s^2 C_s^2} - j \frac{\omega C_s}{1 + \omega R_s^2 C_s^2} \tag{1.35}$$

* Complex permittivity: $\qquad \epsilon^* = \epsilon' + j\epsilon'' \tag{1.36}$

* Complex Modulus: $\qquad M^* = M' + jM'' = \frac{1}{\epsilon^*} \tag{1.37}$

By plotting the real part against the imaginary part of these variables, a so-called Cole-Cole plot results. For more practical case, double arcs can occur and the center of the arc may drop down below the horizontal axis. A detailed discussion can be found in McDonald's book (1987). The sample plots for the complex impedance case are shown in figures 1.13 (simple case) and 1.14 (complex case).

All of these analyses and measurements provide the electrical transport information at lower temperatures and can be used as additional evidences to support the conclusion drawn based on the high temperature σ_{DC} and Seebeck coefficient measurements.

Optical absorption is used to confirm the conclusion based on the above experiments. Detailed discussion can be found in Bossman's (1970) review paper.
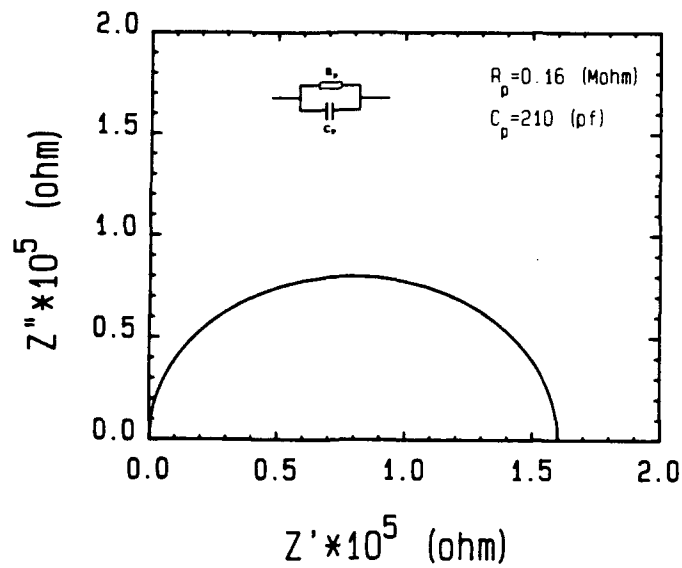
Figure 1.13 Impedance complex plane analysis for a simple parallel RC (resistance-capacitance) network.
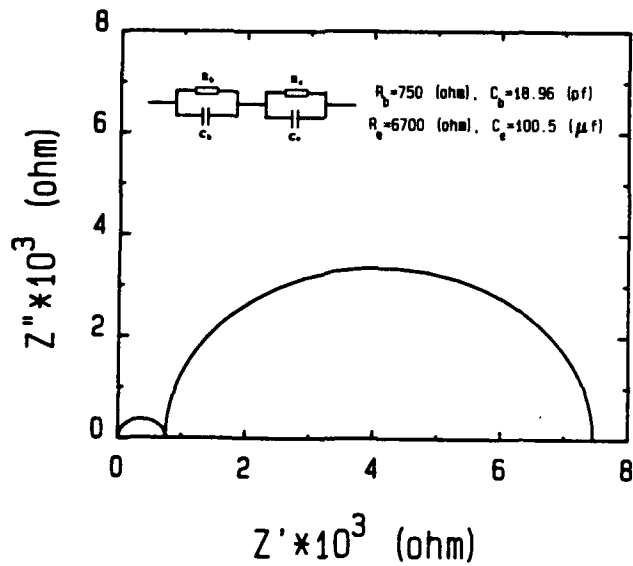
Figure 1.14 Impedance complex plane analysis for a complex RC network involving bulk and electrode process.

40

Chapter 2 EXPERIMENTAL TECHNIQUES

In this chapter, several available processing methods for preparing uniformly mixed compounds with various doping species and levels will be discussed. Some suitable techniques for best understanding the relationship between defect chemistry, microstructure and dielectric properties will also be explored.

2.1) *Sample Preparation*

In this section, general preparation methods for ceramic samples will be discussed, the different sample preparation techniques for specific analyses, such as TEM, EPMA and dielectric relaxation, will be also described in brief.

Ultra high purity(>99.99%) starting chemicals have been used throughout most of these studies. Oxides, carbonates, nitrates and other organo-metallic compounds were purchased from the companies of Johnson Matthey, Alfa, Aldrich and Fisher Scientific. Several processing techniques utilized in this work will be discussed as follows:

CONVENTIONAL CERAMIC PROCESSING ROUTE. Correct amounts of the starting chemicals $BaCO_3$, ZnO, Nb_2O_5, $La(HC_2O_4)_3$, and K_2CO_3 (purchased from Johnson Matthey) were weighed on an analytical balance. The chemicals were then ball-milled in a plastic bottle with 200 proof CH_3CH_2OH (purchased from Fisher Scientific) using resin coated iron balls for 24 hours (Takada, K., 1986). The slurry was then dried on a hot plate in a Teflon beaker using a Teflon coated stirring bar to avoid sedimentation. The dried mixture was calcined at 800°C for 8 - 10 hours in air. After calcination, the powder was hand milled using an agate mortar and pestle for 2 hours. The powder was then put into a plastic bottle to go through the ball-milling (24 hours), drying, calcination (increasing the temperature by ~100°C, yet keeping it ~400°C below the final sintering temperature), and hand-milling procedure again. This repeated processing method proved to be an effective way of obtaining a homogeneous, calcined powder. Since special care was taken, contamination was minimized. Finally, the calcined powders were cold-pressed into pellets of desired geometry at 77 MPa. Subsequently, selected samples were isostatically cold-pressed at 280 MPa to increase the green density. The pellets were sintered at temperatures between 1400°C and 1600°C in either a conventional tube furnace (air atmosphere), or a hot press furnace in a reduced atmosphere for three hours.

41

<u>CO-PRECIPITATION METHOD</u>. Co-precipitation is a chemical method by which homogeneous, fine particle size ceramic powders can be prepared after an appropriate calcination. The precipitate is formed by the simultaneous precipitation of cations from a solution by drop-wise addition to a basic bath. The improved homogeneity with respect to conventional ceramic processing would be an advantage for this study since small amounts of dopants need to be homogeneously dispersed. Also, the fine particle size which will improve the sinterability of BZN which is rather refractory and difficult to sinter. Therefore, the co-precipitation method is an attractive method to make powders. Unfortunately, it is very difficult to find a water soluble Nb salt. Kakegawa et.al. (1986) claimed that when a solution containing Mg^{+2} and Ta^{+5} was added to an aqueous ammonia solution of oxine, a precipitate was obtained. The thermally decomposed precipitate was mixed with $BaCO_3$ and fired at 1300°C to obtain BMT. The only drawback with their procedure is that the starting solution containing Ta^{+5} comes from $TaCl_5$. It is very difficult to eliminate Cl ions from the final ceramic product. This inhibits the study of defect chemistry of these type of materials. In this study, niobium oxalate ($Nb(HC_2O_4)_5$) was used to make the starting solution. Unfortunately, the solubility product of $ZnC_2O_4.2H_2O$ is quite small ($1.37*10^{-9}$, CRC Handbook, 1986). Therefore, only a very dilute solution containing both Zn^{+2} and Nb^{+2} could be obtained which is of no practical use. The present task for making a complete series of solid solutions between BT and BZN could not be fulfilled.

<u>LIQUID MIX TECHNIQUE</u>. Since Pechini (1967) first demonstrated this novel method, it has been widely used in the research laboratory for a variety of applications, especially where precise control of the chemical composition is required (Chan, N.H., et.al., 1981a, b; 1982; 1984). This technique is basically a three step procedure (mixing-polymerization-calcination). The stock solutions containing different cations are mixed and then polymerized at high temperature. Final powder is obtained through calcination. The procedure for preparing stock solutions is described in detail below.

Ti stock solution was prepared through the following procedure:

(1) Pour 600 ml ethylene glycol (EG, purchased from Fisher Scientific) into a flask.

(2) Slowly add 200 ml tetra-isopropyl-titanate (TPT, purchased from Alfa Chemical) into the flask, and stir it using a Teflon coated stirring bar.

(3) Slowly add 150 grams citric acid (purchased from Fisher Scientific) into solution and stir it. Pay attention to the color of solution, wait till color change from milky white suspension to transparent light yellow.

42

(4) After obtaining a clear solution, add 200 grams more of citric acid into solution.

(5) Keep the temperature close to 100°C on a hot plate. Stir the solution for about 8 hours to let the alcohol evaporate, so that the final stock solution can be easily weighed later on.

(6) Keep the stock solution in a cool dry place without exposure to strong light to avoid decomposition.

The Zn stock solution was a $Zn(NO_3)$ water solution. Nb stock solution was prepared as follows:

(1) In a gas tight glove box, pour 300 ml EG into a flask, and add 20 grams citric acid into flask.

(2) Set a hot plate around 120°C, and stir the solution until all of the citric acid dissolves.

(3) Flush the glove box with dry CO_2 for a few minutes to avoid niobium ethoxide decomposition in air.

(4) Open niobium ethoxide bottle (purchased from Aldrich Chemical). Pour it into the flask, and stir it with a Teflon coated stirring bar for about 2 minutes until the solution turns light yellow and transparent. Keep temperature close to 120°C.

(5) Keep Nb stock solution in a tight plastic bottle in a cold and dry place without exposure to strong light.

Before actually making the sample, all stock solutions were assayed using a gravimetric method. Since the oxide powder after calcining has a large surface area, special care was taken to minimize the experimental error. Proper amounts of the stock solutions were weighed and slowly heated to form a gel. The gel was calcined in a box furnace with a very slow ramp rate of 0.2°C/min. until the peak temperature was reached (800 - 950°C) and held for 3 hours. The calcined oxide powders were cooled to ~100°C, and put into a desiccator directly to avoid absorbed moisture. After it was completely cooled to room temperature, the powder was quickly weighed on an analytical balance with subtraction of the air buoyancy effect, which depends on the temperature and atmospheric pressure. The final concentration of the stock solution in terms of oxide(g)/solution(g) was obtained.

Correct amounts of $BaCO_3$, Ti, Zn and Nb stock solution were weighed and mixed into a platinum crucible. The solution was put on a hot plate set at the temperature around 120°C. A citric acid water solution (1:1) was added dropwise into

43

the solution using a squeeze bottle to help dissolve the $BaCO_3$. After all of the $BaCO_3$ was dissolved, the temperature was gradually increased to gel the solution. The gel was put into a box furnace and the temperature was raised slowly until it polymerized. Calcination was carried out at 800-950°C for 3 hours. A fine homogeneous powder with precisely controlled chemical composition was obtained.

In the case of Zn and Nb co-doped BT, special care was taken to avoid undesired precipitation. $BaCO_3$ and Zn stock solutions were added into the Ti stock solution first, and then the solution was put on the hot plate. The Nb stock solution was added after all of the $BaCO_3$ dissolved.

The only problem with this technique is the limitation of high doping level. The highest doping level for Zn/Nb co-doped BT in this study is 9%. Higher doping levels did not give rise to a clear solution. Therefore, further gel-polymerization-calcination became ineffective. From BT to BZN, higher substitution of Ti by Zn/Nb was produced using a conventional solid state reaction route.

2.2) *High Temperature Equilibrium DC Conductivity and Seebeck Coefficient*

High temperature equilibrium DC conductivity and Seebeck coefficient measurements at different oxygen partial pressures are the main tools for high temperature defect chemistry studies. Samples for this type of measurement were rectangular bar type. Standard four point DC measurement was carried out for conductivity (Chan, N.H., et.al., 1981a). Sample geometry and electrode setting are shown in figure 2.1. A special fixture for conductivity and Seebeck coefficient measurements was made to meet high temperature and various oxygen partial pressure requirements (figure 2.2). A platinum heater was mounted next to the sample to generate a temperature gradient. The equilibrium conductivity and Seebeck coefficient can be measured simultaneously in this set up.

2.3) *Electron Microscopy*

Various electron microscopes were used in this work for microstructural/microchemical characterization. An ETEC SEM equipped with EDS (energy dispersive spectrometer) was used mainly for grain size, surface morphology and routine chemical composition observations. AEM (analytical electron microscopy) studies were carried out using Philips 400T and Philips 430, 300kV analytical transmission electron microscopes equipped with EDS. In order to study the
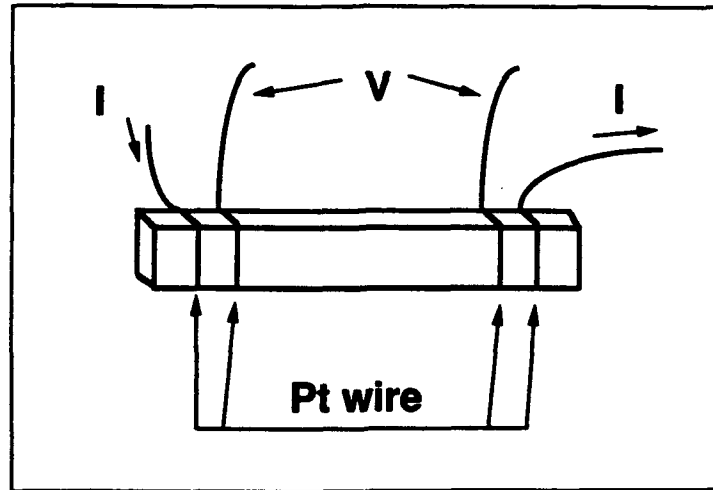
Figure 2.1 Sample geometry for the four point high temperature equilibrium DC conductivity measurement.
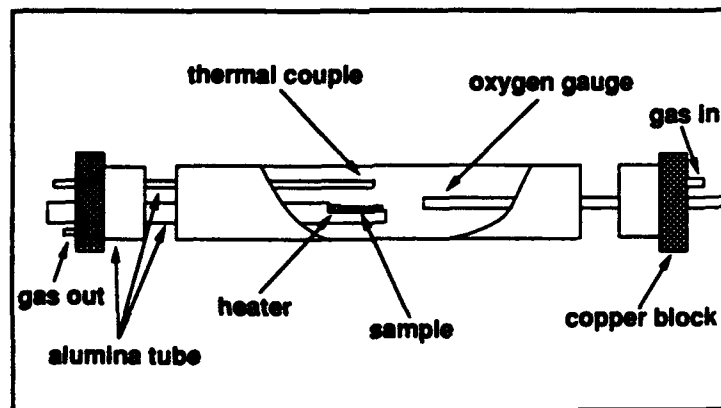
Figure 2.2 Schematic of an experimental set up for a simultaneous measurement of high temperature equilibrium electrical conductivity and Seebeck coefficient.

microchemical ordered microdomains and related phenomena, not only conventional SAEDP (selected area electron diffraction pattern) but special techniques, such as CBED (convergent beam electron diffraction) and HRTEM (high resolution TEM) were also carried out in this work. For defect structure analysis, phase identification purposes, the JOEL 733 super probe EPMA (electron probe micro-analysis) equipped with WDS (wavelength dispersive spectrometer) was utilized.

Samples for TEM, HRTEM etc. were prepared by standard TEM sample preparation procedures. Thin slices from sintered pellets were cut using a diamond saw and then ground on fine SiC grinding papers with successive grades down to 600 grade (about $17\mu m$). 3-1μm diamond paste on a polishing wheel covered with a cloth was temperature equilibrium DC conductivity and Seebeck coefficient.used for final polishing. The thin foil (50-100μm in thickness) was cut to a round piece (3 mm in diameter) using a Gaton ultrasonic disc cutter (model 601) and dimpled down to $\sim 10\mu m$ on an automatic dimpler grinder (Gaton model 656). The sample was then mounted on a copper grid using Krazy glue. A Gaton Ion Beam Thinner was used for final thinning. The thinning conditions were as follows: Ar beam; 5kV acceleration voltage and 1mA gun current (0.5mA for each side); 30°-12° for tilting angle (first 0.5 hour 30°, then 12°). In order to avoid sample heating, a liquid nitrogen cold stage was used during the thinning process. Sometimes for thinner foils, the acceleration voltage was dropped to 2 kV and 0.5mA (0.25mA for each side) to avoid ion beam damage. The prethinning of thin foil samples (dimpling process) is very important for preventing ion beam damage. The shorter the samples stay in the ion beam thinner, the less the damage.

Bulk samples for EPMA study were mounted in an epoxy mount. Grinding was carried out using successively finer grits of SiC grinding paper. 6μm and 1μm diamond paste, 0.05μm SiO_2 colloid solution and a Buehler Vibromet I automatic vibratory polisher were used for polishing to optical finish. Samples were then coated with a thin layer of carbon for WDS, BSE (backscattering electron imaging) and X-ray map analysis. For grain morphology and grain size observations, a piece of sintered pellet was ground and polished following the procedures described above. Final samples with well polished surfaces were either thermally etched at a temperature of $\sim 400°C$ below the sintering temperature for about 0.5 to 1 hour or chemically etched at room temperature by dipping the sample into a solution (4% HNO_3 + 2% HF + 96% water) for a few seconds. The Pd/Au coating was sputtered onto the surface for SEM observation.

2.4) *XRD and DSC*

Powder X-ray diffractometry (XRD) and differential scanning calorimetry (DSC) were used for phase transition studies. Bulk and powder forms were both tested under the conditions of Cu Kα radiation, 45 kV and 30 mA using a Philips APD 3720 XRG 3100 X-ray diffractometer. Lattice refinement and lattice parameter determination were carried out utilizing a commercial computer software package Philips APD Crystallography. A Mettler DSC instrument was used for latent heat measurements. Weighed powder or small bulk samples were put into an aluminum pan. The heat flow difference was measured against a reference pan. The heating rate was 4 K/min. The measurement was taken in air using a liquid nitrogen cooling system.

2.5) *Optical absorption*

Optical absorption study was conducted on a bulk sample using a Cary 2300 automated spectrophotometer. Diffused scattering mode was selected and scanning wave length was in the range of 200 nm to 500 nm. The bulk sample with a flat but rough surface was placed against the window. Relative absorption intensity against wavelength was recorded on a floppy disk. The main purpose of using this technique was to determine the band gap of the material for comparison with the results obtained from electrical conductivity.

2.6) *Dielectric measurements*

Dielectric spectra of the weak field permittivity and dissipation factor were measured over the wide temperature range (-150 to 600°C) and frequency range (10 Hz to 15 MHz).

For the low temperature range (-150 to 200°C), an automated measurement system was used. Hewlett-Packard (HP) new generation of microprocessor-based multifrequency impedance meters were used to measure capacitance and dissipation factor. The HP4274A multi-frequency LCR meter covers the frequency range from 100 Hz to 100 kHz with basic accuracy of 0.1%. The HP 4194A RF impedance analyzer covers the frequency range from 100 Hz to 40 MHz with an accuracy ranging from 0.5% to 100% depending on the sample impedance, measuring frequency and measuring circuit.

A Delta Design model 2300 oven with an IEEE 488 interface and an environmental chamber covers the temperature range from -150 to 200 °C. Low

47

temperatures were obtained by liquid nitrogen cooling. Measured samples (up to 8 samples can be measured simultaneously) were mounted on a specially designed fixture. An HP 9825 desk top computer was used for on line control of automatic measurement through a standard IEEE 488 interface. Results of the measurements were recorded on a flexible magnetic disk.

For higher temperature measurements, a regular tube furnace with carefully designed sample fixture to minimize the complication due to parasitic capacitance and inductance was used for measurements from 25 to 600°C. The quartz and alumina tubes with silver coating was carefully grounded to avoid interference from the 60 Hz power line frequency. Inert gases, such as Ar_2, He_2 or N_2, were passed through the quartz tube during the measurement to protect the silver electrode and coating. The measurement of capacitance and conductance was carried out using a General Radio 1616 precision capacitance bridge with a basic accuracy of 0.1%.

Samples for dielectric measurement were polished disc type. Electrodes were applied by either vacuum depositing gold or painting a low temperature (200°C) cured silver. Some samples with the same electrode material and different thickness (Jain, H., 1990) were also tested to identify if electrode polarization existed.

Special software was developed for data analysis. A Cyber 850 mainframe was used to carry out the main calculation for complex plane impedance analysis.

Chapter 3 MICROSTRUCTURE of BZN

In this chapter, we will present a systematic experimental study for the model system BZN. Stoichiometric BZN (Zn/Nb=1/2) has been reported to have a cubic structure with a space group Pm3m, where the cations Zn and Nb are randomly distributed (Galasso, F., et.al., 1963; Tennery, V.J., 1969; Treiber, U., et.al., 1982). In this study, the partially ordered nature of stoichiometric BZN has been identified by electron diffraction. It has also been found that the Zn/Nb ratio plays an important role in determining the nature of the ordering in nonstoichiometric BZN (Zn/Nb$\neq$1/2). Nb-rich BZN favors 1:2 type ordering which coincides with the high temperature annealing results. On the other hand, Zn-rich BZN shows only the 1:1 type of ordering, which does not change with appropriate heat treatment, but can be enhanced by doping La on the Ba site with compositional adjustment of the Zn/Nb ratio close to unity.

3.1) *Composition Design and Experimental*

A summary of the compositions of the samples studied is given in Table 3.1. All polycrystalline ceramics were made by conventional ceramic processing. The starting materials; $BaCO_3$, ZnO, Nb_2O_5 and $La(HC_2O_4)O_3$ (purity > 99.99%) were ball milled in polyethylene bottles using resin coated iron balls for 24 hours in alcohol. The slurry was dried and then calcined at 1000°C for 10 hours. Samples were cold pressed under 77 MPa and sintered between 1350°C and 1600°C for 3 hours in air. Some of the stoichiometric BZN samples were quenched from 1400, 1500 and 1600°C to room temperature, a few were fast fired at 1600°C and some were annealed at 1400°C. Some stoichiometric BZN samples were also sintered or annealed at various oxygen partial pressures.

Nonstoichiometric BZNZ and BZNN were investigated to see if the ordering type depended on the Zn/Nb ratio; the BZNB was used to test if Ba could occupy B$'$ site to generate 1:2 type ordering after Zn loss, BLZN and BLZN$'$ were made to see if La as a donor could enhance 1:1 type ordering. BKZN and BKZN$'$ were used to see the possible counter-effect of acceptor doping on 1:1 type ordering. Final relative densities in the range of 90 -- 98% of theoretical density were achieved for all samples except the heavily Zn rich samples (BZNZ with x>3%), which only reached about 80% of theoretical density. Polished sections of samples were analyzed using EMPA and XRD techniques. The thin foil specimens were examined in a transmission electron microscope (TEM)

49

BZN:	$Ba(Zn_{1/3}Nb_{2/3})O_3$	*stoichiometric undoped BZN.*
BZNZ:	$Ba(Zn_{1/3}Nb_{2/3})_{1-x}Zn_xO_3$ x=0.005 — 0.03	*nonstoichiometric BZN ;* *Zn rich and acceptor doped.* *Zn/Nb > 1/2.*
BZNN:	$Ba(Zn_{1/3}Nb_{2/3})_{1-x}Nb_xO_3$ x= 0.005 — 0.09	*nonstoichiometric BZN;* *Nb rich and donor doped.* *Zn/Nb < 1/2.*
BZNB:	$Ba(Ba_xZn_{1/3-x}Nb_{2/3})O_3$ x=0.01	*1% Ba replace Zn* *and occupy the Zn site.*
BLZN:	$Ba_{1-x}La_x(Zn_{(1+x)/3}Nb_{(2-x)/3})O_3$ x=0.01 — 0.10	*donor doped,* *charge compensated* *by increasing Zn/Nb ratio.*
BLZN':	$Ba_{1-x}La_x\square_{x/2}(Zn_{1/3}Nb_{2/3})O_3$* x= 0.01 — 0.10	*donor doped,* *maintaining Zn/Nb ratio.* * $\square$ *stands for a vacancy.*
BKZN:	$Ba_{1-x}K_x(Zn_{(1-x)/3}Nb_{(2+x)/3})O_3$ x=0.01	*acceptor doped,* *charge compensated* *by decreasing Zn/Nb ratio.*
BKZN':	$Ba_{1-x}K_x(Zn_{1/3}Nb_{2/3})O_{3-x/2}V_{o_{x/2}}$ x= 0.01	*acceptor doped,* *maintaining Zn/Nb ratio.*

Table 3.1 Chemical composition summary

equipped with EDS for chemical analysis. High resolution TEM images were taken at 300 kv with near optimum Scherzer defocus as determined by optical diffractometry (ODM, see Spence, J.C.H., 1981).

3.2) *Microchemical Ordering in BZN*

3.2.1) Stoichiometric BZN

The stoichiometric BZN was sintered at $1600°C$ for 3 hours and furnace cooled ($-400°C$/hr.) to room temperature. XRD results showed that the samples were single phase with the perovskite structure with a=0.4094 nm (Figure 3.1a). However, as can be seen in Figure 3.1b, diffuse superlattice reflections of the type $(\frac{h}{2} \frac{k}{2} \frac{l}{2})_{s1}$ (h k l odd) were obtained in SAEDPs, thus indicating a doubling of the cubic unit cell dimension due to ordering. Figure 3.1d shows a centered dark-field (CDF) micrograph using a $(\frac{1}{2} \frac{1}{2} \frac{1}{2})_{s1}$ reflection; the bright regions (2~5 nm) are ordered domains. Identical CDF images were obtained when imaging by using different variants of the $\{\frac{1}{2} \frac{1}{2} \frac{1}{2}\}_{s1}$ family of reflections. The $(\frac{1}{2} 0 0)_{s1}$ and $(\frac{1}{2} \frac{1}{2} 0)_{s1}$ reflections were absent, which is consistent with the extinction rules for face centered cubic (FCC) materials. Also, no dynamical absences were observed by using convergent beam electron diffraction (CBED) technique (Williams, D.B., 1984; Vacchio, K., 1988). It is then referred that the extinction rule can only be controlled by a center symmetry in the unit cell (Edington, J.W., 1975). Therefore, the lattice type in ordered BZN is FCC. By analogy to lead scandium tantalate (PST, see Setter, N., 1980; Chan, H.M., et.al., 1985), the above results indicate that the structure of ordered BZN is of the general form $A(B'_{1/2}B''_{1/2})O_3$ with space group Fm3m (figure 3.1a). On the other hand, the SAEDPs with long exposure time taken from the [110] and [111] zone axes are shown in Figures 3.1b, c. 1:1 type ordered superlattice spots are clearly seen. In addition, the other weak superlattice reflections of type $(\frac{h}{3} \frac{k}{3} \frac{l}{3})_{s2}$ are also observed, thus implying another type of ordering scheme. Unfortunately, the superlattice reflections located in the $(\frac{1}{3} \frac{1}{3} \frac{2}{3})_{s2}$ and $(\frac{2}{3} \frac{2}{3} \frac{4}{3})_{s2}$ in the [111] zone axis are too weak to resolve the ordered domains with the CDF imaging technique.

3.2.2) 1:1 Type Ordering

3.2.2.1) Ordering Model

The two most likely ordering models consistent with this ordering scheme are as follows:
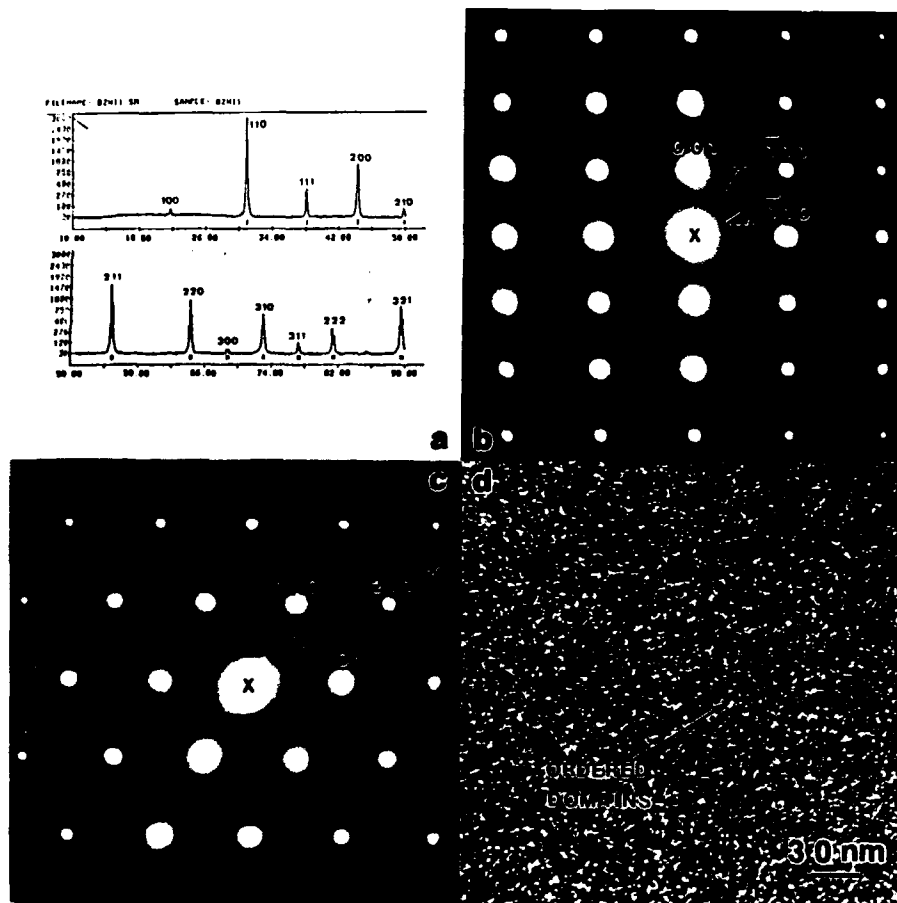
Figure 3.1 Ordering in stoichiometric BZN: (a) XRD result; (b) SAEDP of [110] zone
axis; (c) SAEDP of [111]zone axis; (d) CDF (centered dark field) image using ($\frac{1}{2}$ $\frac{1}{2}$ $\frac{1}{2}$)
reflection. The bright dots are ordered microdomains.

52

MODEL 1: B' ----- Zn^{2+} and Nb^{5+} *(disordered, 2:1 ratio)*

            B'' ----- Nb^{5+}
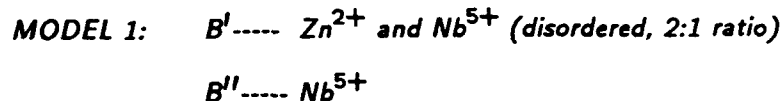
This type of ordering is equivalent to the $(NH_4)_3FeF_6$ (Pauling, L., 1924) type structure, and has been reported to occur in some other systems (Fresia, E.J., 1959; Galasso, F., 1969; Padel, L. et.al., 1972; Lecomte, J., et.al., 1981 and Chen, J., et.al., 1989). Padel (1972) calculated the ordering based on the X-ray analysis for the system $Ba(U_{1/3}Fe_{2/3})O_3$. The simulation results were in good agreement with experimental results. In this model, the ordered BZN structure can be represented as $Ba[(Zn_{2/3}Nb_{1/3})_{1/2}Nb_{1/2}]O_3$; thus the B'' sites are occupied exclusively by Nb^{5+} ions, and B' sites are occupied by a random mixture of Zn^{2+} and the remaining Nb^{5+} ions. Because the average composition of ordered regions is identical to that of the bulk BZN, no charge imbalance exists within the ordered regions. However, if that were the case, the ordered domains would be expected to grow during heat treatment as in PST. Experimentally, however, the microdomains were not observed to grow. Table 3.2 summarizes the heat treatment results. As can be seen, the 1:1 type ordering persists at all heat treatments. However, after annealing at high temperature, the 1:2 type ordered domains did grow, which will be discussed later in this chapter. It follows, therefore, that 1:1 type ordered domain growth is strongly inhibited in stoichiometric BZN.

MODEL 2: B' ----- Zn^{2+}

            B'' ----- Nb^{5+}
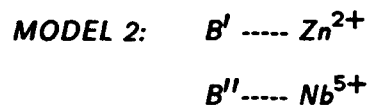
In this model. it is postulated that the Zn^{2+} and Nb^{5+} ions order in a 1:1 ratio on the B site sublattice of BZN. This is directly analogous to the ordered PST structure as shown in Figure 3.1a for this type of ordering. Because the Zn/Nb ratio is 1:1 (or close to 1:1) within the ordered domains, (as opposed to 1:2 for the average composition), strong charge effects would result, in which the ordered regions would have a net negative charge with respect to the surrounding region. This in turn, would be expected to severely restrain domain growth, and indeed, this was observed. In view of this fact, we are inclined to favor model 2 over model 1. Since the ordered regions are Zn rich (relative to the average BZN composition), in order to preserve stoichiometry, the regions around the domains would have to be Nb rich. It then follows that the 1:1

heat treatment	phase	structure
sintered at 1600°C and furnace cooled	single (fig.3.1a)	mixture of short range ordering of 1:1 and 1:2 type (fig. 3.1b,c)
fast fired at 1600°C	single	same as above
quenched from 1600 1500, 1400°C	single	1:1 type + very weak 1:2 type ordering
Annealed at 1400°C for 100 hrs.	Nb rich second phase on the surface (fig. 3.9)	mixture of short range ordering of 1:1 and grain boundary nucleation of 1:2 type ordered phases (fig. 3.10a)

Table 3.2 Heat treatment of stoichiometric BZN

type ordered domains would in fact be acceptor-type island regions (Zn/Nb>0.5) surrounded by a donor-type shell (Zn/Nb<0.5). Jacobson, A.J. (1976) studied oxygen deficient barium zinc tantalate (BZT) with formula $Ba(Zn_{1/2}Ta_{1/2})O_{2.75}$ and found very weak 1:1 type of ordering by X-ray analysis, which supports model 2.

3.2.2.2) La Doped BZN

(a) Zn/Nb Ratio Increased (BLZN):

As an attempt to distinguish between the two models, a series of samples were made up of the following compositions:

$$Ba_{1-x}La_x(Zn_{(1+x)/3}Nb_{(2-x)/3})O_3, \quad \text{where } x=1\%, 5\%, 10\%.$$
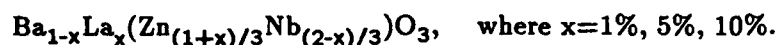
For these compositions, La^{3+} ions are substituted for Ba^{2+} ions on the A site sublattice. Since La is trivalent whereas Ba is divalent, the La behaves as a donor dopant. In this series of samples, the compositions are adjusted so that compensation for the La is achieved by increasing the Zn/Nb ratio. Now let us consider how this influences the 1:1 type of ordering behavior. In the case of model 1, since the Zn/Nb ratio in the ordered regions is the same as in the bulk, there is no charge imbalance resulting from the ordering, thus La doping would not be expected to influence the degree of ordering. However, for model 2, since the ordered regions are Zn rich, they can be considered to be acceptor doped. Thus donor doping with La would be expected to compensate the charge effects resulting from ordering, and hence favor an increased degree of order. As can be seen in following discussion, enhanced ordering was indeed observed.

SAEDPs show that the intensity of the $(\frac{1}{2} \frac{1}{2} \frac{1}{2})_{s1}$ type superlattice reflections increase with the La^{3+} concentration, thus indicating an increased degree of order. In addition, CDF images reveal that the size of the ordered domains increased from 10~20 nm to >500nm (see figure 3.2). The wavy boundaries separating the ordered domains are APB's (Edinton, J.W., 1975).

(b) Zn/Nb Ratio Unchanged (BLZN'):
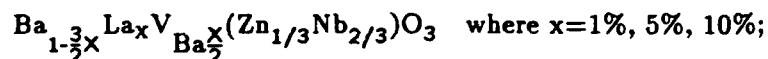
$$Ba_{1-\frac{3}{2}x}La_xV_{Ba\frac{x}{2}}(Zn_{1/3}Nb_{2/3})O_3 \quad \text{where } x=1\%, 5\%, 10\%;$$

Figure 3.2 CDF images of samples $Ba_{1-x}La_x(Zn_{(1+x)/3}Nb_{(2-x)/3})O_3$ with x=0.05 and 0.10, showing the growth of 1:1 type of ordered microdomains with increasing La dopant level .

For this series of samples, the intention was to test whether the La doping could be compensated by the introduction of barium vacancies.

Examination of the sintered microstructures using TEM and EMPA revealed a second phase (figure 3.3). XRD results showed that as the La concentration increased, the volume fraction of second phase increased accordingly. In addition, TEM revealed that the ordered domain structure of these specimens was identical to that of the BLZN compositions (i.e. where compensation was achieved by adjustment of the Zn/Nb ratio).

It can be concluded from these results that barium vacancies are not favorable defect species in this system. Instead, the system prefers to restore the A:B ratio via the formation of a Nb rich second phase, and by self-adjusting the Zn/Nb ratio which results in the enhancement of 1:1 type of ordering. Furthermore, defect chemistry study also supports this idea which will be discussed in chapters 4 and 6. The reaction equation can be written as

$$Ba_{1-\frac{3}{2}X}La_xV_{Ba\frac{X}{2}}(Zn_{1/3}Nb_{2/3})O_3 + \tfrac{X}{4}O_2 =$$
$$Ba_{1-13X/12}La_x(Zn_{1/3}Nb_{(4-X)/6})O_3 + (BaNb_2O_6)_{X/12}$$

$$BLZN' \qquad = \qquad BLZN(Zn/Nb{>}\tfrac{1}{2}) \qquad + \qquad \text{second phase.}$$
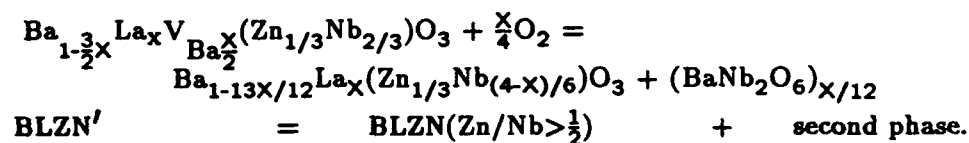
3.2.2.3) K Doped BZN

In order to check that the ordering model is self-consistent, a series of samples were also designed and with the following compositions:

$$BKZN: \quad Ba_{1-x}K_x(Zn_{(1-x)/3}Nb_{(2+x)/3})O_3, \quad \text{where } x{=}1\%.$$
$$BKZN': \quad Ba_{1-x}K_x(Zn_{1/3}Nb_{2/3})O_{3-x/2}V_{Ox/2}, \quad \text{where } x{=}1\%.$$
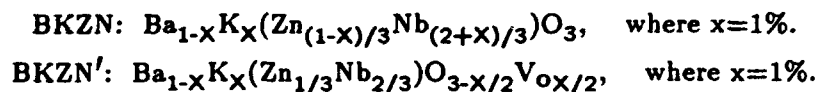
For these compositions, the basic idea is similar to the La doped case, except that by applying the opposite concept to the K doped case, the 1:1 type ordering may be decreased. There are two points to be considered here. First, if model 1 is correct, K doped into the Ba site as an acceptor with self adjustment of the Zn/Nb ratio to maintain the overall charge balance would decrease the tendency for 1:1 type of ordering. In the case of BKZN', the self Zn/Nb ratio adjustment may lead to the
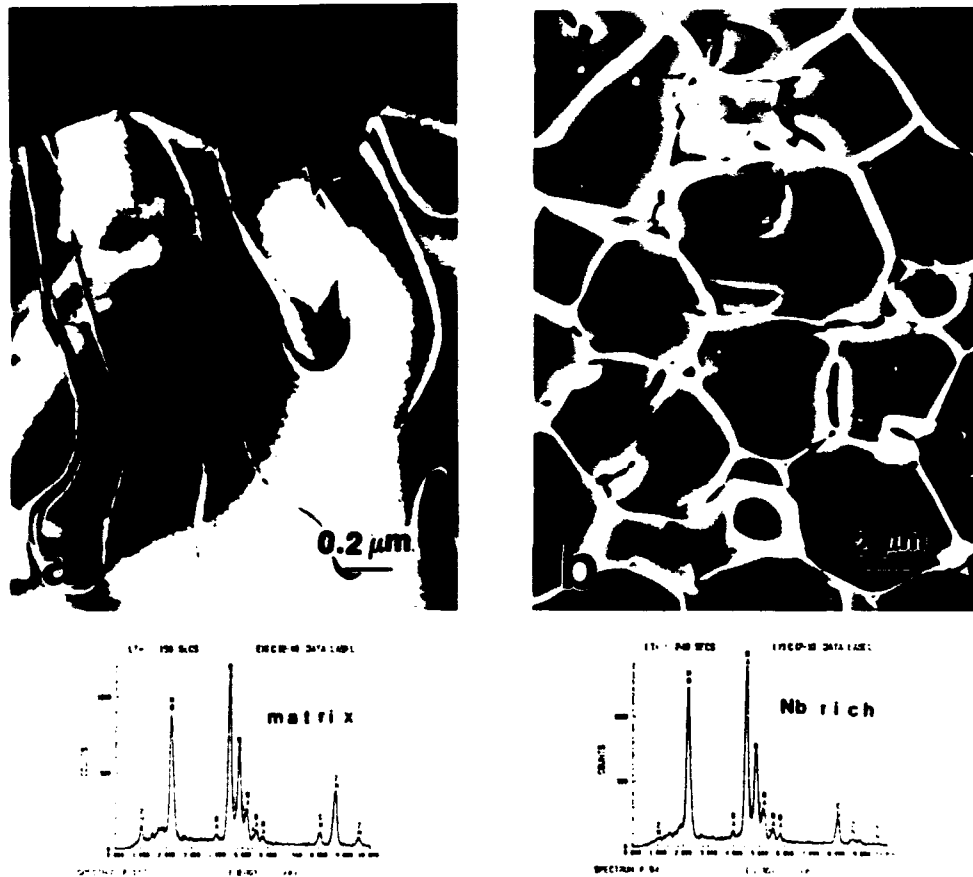
Figure 3.3 (a) CDF images $Ba_{1-\frac{3}{2}x}La_x(Zn_{1/3}Nb_{2/3})O_3$ with x=0.10, showing the same degree of 1:1 type ordering as in figure 3.2 along with grain boundary Nb rich second phase. (b) SEM SE image of the same sample chemically etched showing grain boundary Nb rich second phase. EDS spectra were taken from matrix and second phase, respectively.

appearance of a Zn rich second phase. Otherwise, the system may just simply prefer the oxygen vacancy compensation for K doping, and the ordering behavior would remain the same.

As indicated in Figure 3.4, the intensity of the $(\frac{1}{2} \frac{1}{2} \frac{1}{2})_{s1}$ type superlattice reflections in the [110] type zone axis do not change with K doping. Instead, the system shows a typical acceptor doped behavior which will be discussed in chapter 4. This implies that the system prefers the oxygen vacancy compensation for K doped on the Ba site and the idea for K doping to check the model is not appropriate. This result is surprisingly different from the case for PMN where Na doped PMN shows a weaker 1:1 type ordering compared with undoped PMN (Chen, J., et.al., 1989).

3.2.2.4) Zn/Nb Ratio Adjustment—Zn Rich BZN (BZNZ)

Further information on the mechanism of ordering in BZN can be obtained through an adjustment of the Nonstoichiometry. This is also another approach to test which model is correct. The type of ordering of nonstoichiometric BZN depends on the Zn/Nb ratio. Figure 3.5 summarizes a systematic study of a series of Zn or Nb rich nonstoichiometric BZN compounds.

As discussed previously, when La doping is accompanied by an increase in the Zn/Nb ratio, 1:1 type ordering is enhanced. If model 2 is the correct interpretation for the 1:1 type of ordering, the Zn rich nonstoichiometric BZN with the formula

$$Ba(Zn_{1/3}Nb_{2/3})_{1-x}Zn_xO_3, \quad \text{Where x= 0.5, 1, 3\%}$$
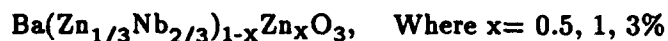
should be inclined towards the 1:1 type of ordering. The experimental results indicate that this is the case. Similar to the figure 3.1d, the 1:1 type ordered domains have been observed in all BZNZ samples. There appears to be almost no difference in the size of those domains observed in BZNZ samples. Notice that in figure 3.7 the 1:2 type of superlattice reflections, however, become weaker as the Zn concentration increases, and eventually disappear. This behavior could be understood as a compromise between Zn rich 1:1 type ordered domain formation and charge imbalance generated by this formation. The larger the Zn/Nb ratio, the more 1:1 type ordering, and less 1:2 type ordering due to chemical composition adjustment is observed. From the defect chemistry point of view, if the extra Zn occupies Nb-sites as a typical acceptor type

59
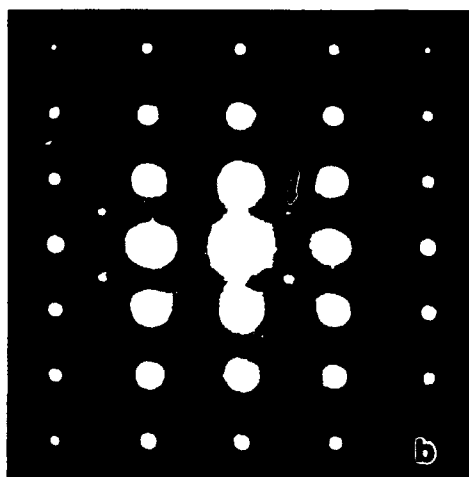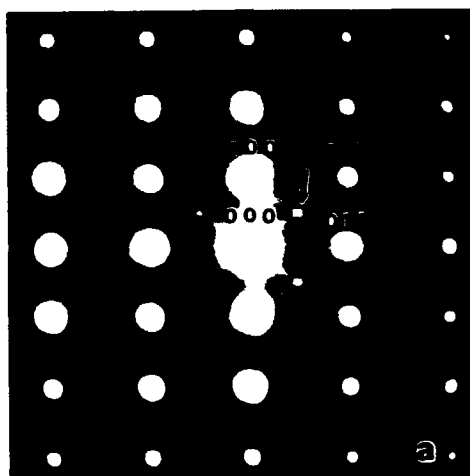
Figure 3.4 SAEDPs ([0$\bar{1}$1] zone axis) of stoichiometric BZN (a) and $Ba_{1-x}K_x(Zn_{(1-x)/3}Nb_{(2+x)/3})O_3$ with x=0.01 (b), showing that the same intensity of superlattice diffraction in both cases.
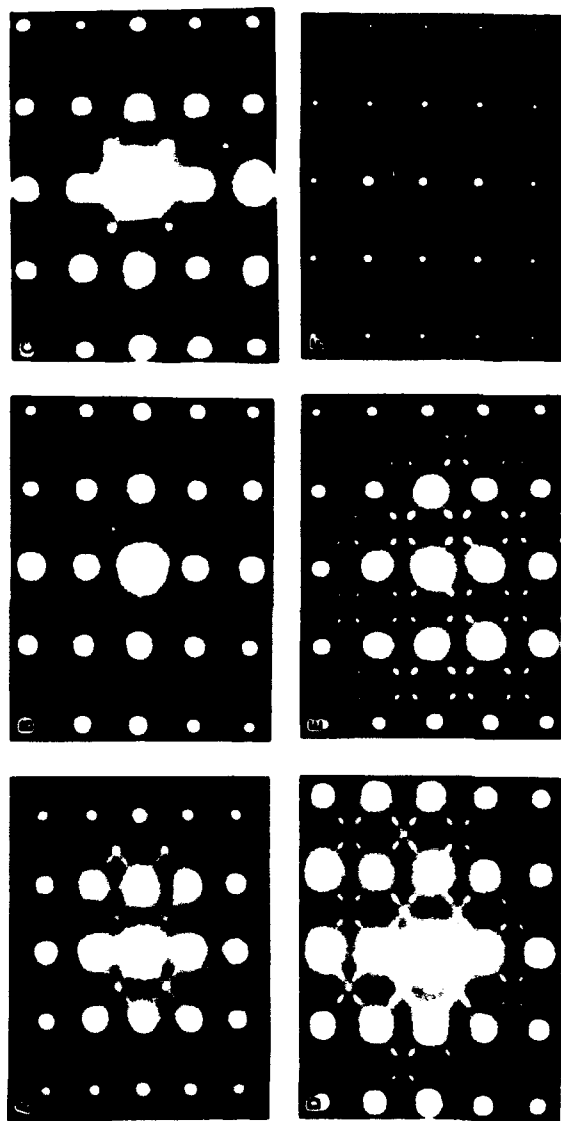
Figure 3.5 A series of SAEDPs of $Ba(Zn_{1/3}Nb_{2/3})_{1-x}M_xO_3$ taken from [110] zone axis: (A) M=0, x=0.00; (B) M=Zn, x=0.005; (C) M=Zn, x=0.01; (D) M=Nb, x=0.005; (E) M=Nb, x=0.03; (F) M=Nb, x=0.09.

defect Zn_{Nb}''', an oxygen vacancy will be generated as a compensating defect species. The oxygen vacancy may weaken the tendency for 1:2 type of ordering. Oxygen deficient $Ba(Zn_{1/2}Ta_{1/2})O_{2.75}$ (Jacobson, A.J., et.al., 1976), and $A(B'_{1/2}B''_{1/2})O_{2.75}$ (A = Sr, Ba; B' = Li, Na; and B'' = Mo, W. See Sabatier, R., et.al., 1971) show this behavior. We also studied $Ba(Zn_{1/2}Nb_{1/2})O_{2.75}$. However, we were not able to get single phase of this formula because of the low solubility of Zn in BZN. The sample was so sensitive to moisture that it fell apart after setting in air for a short period of time. We estimated that up to ~1% extra Zn can be tolerated by the system, above that, the sample turns color from white to purple, and ZnO precipitates out as a second phase (figure 3.6). We also tried to sinter the stoichiometric BZN in the heavily reducing atmosphere in a hot press furnace to force the system to go to $Ba(Zn_{1/2}Nb_{1/2})O_{2.75}$. After sintering at 1600°C for 3 hours, all the zinc ions in the compound were reduced into zinc metal. No useful information could be gathered through this experiment. Stoichiometric samples annealed at 1400°C in the relatively less reduced atmosphere $(P_{O_2}=10^{-10}$ atm.) did not show any enhancement of 1:1 type ordering.

3.2.3) 1:2 Type Ordering

3.2.3.1) Ordering Model

There are also two models to explain this kind of ordering scheme.

MODEL 3: B' ----- Zn^{2+} *and* Nb^{5+} *(ordered, 2:1 ratio)*

             B'' ----- Nb^{5+}
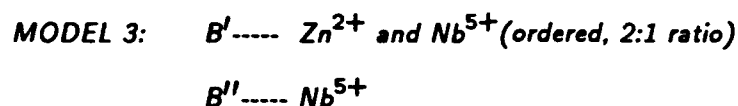
The co-existence of two types of ordered phases in stoichiometric BZN can be explained based on this model. This type of atom configuration was first proposed by Steward and Booksby (1951) to interpret the 1:1 type ordering in complex perovskites with general formula $A(B'_{1/3}B''_{2/3})O_3$. According to the work on $Sr(Sr_{1/3}Nb_{2/3})O_3$, Lecomte and Raveau (1981) suspected that the 1:2 type of ordering could come from B' layer (in our case, $Zn_{2/3}Nb_{1/3} \rightarrow Zn/Nb=2/1$) based on model 1. B' and B'' cations form 1:1 type ordering and the cations in B' layer also form 1:2 type ordering. It follows, thus, that both types of ordering can be observed. However it is difficult to explain why Nb rich nonstoichiometric BZN favors 1:2 type of ordering, and 1:1 type of ordering cannot be controlled by heat treatment. Besides, the Zn/Nb ratio in the 1:2
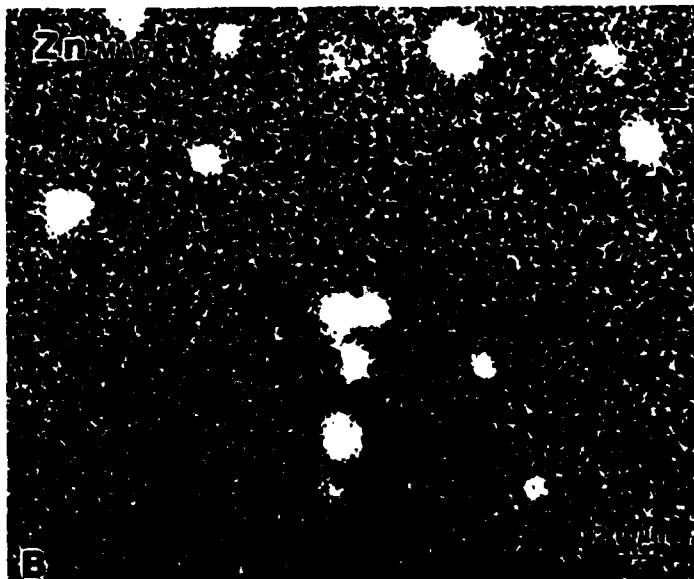
Figure 3.6 BSE (backscattering electron) image (A) and Zn X—ray map (B) of $Ba(Zn_{1/3}Nb_{2/3})_{0.97}Zn_{0.03}O_3$. Noticing the existence of ZnO as a second phase.

type ordered domains were always 1:2 (or close to 1:2) instead of 2:1 by using EDS analysis.

.

MODEL 4: B' ----- Zn^{2+}

B'' ----- $2Nb^{5+}$
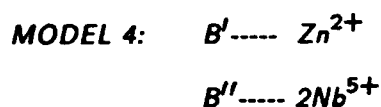
This is a straight forward 1:2 ordering coinciding with chemical composition (Galasso, F., et.al., 1961). However it cannot explain the co-existence of two types of ordering in the system. As will be seen later, the experimental results indicate that the combination of model 2 and model 4 is a proper explanation for the ordering scheme in stoichiometric BZN. Now we are in a position to draw a schematic representation for stoichiometric BZN: there is a phase separation or compositional fluctuation on a nanoscale. Three phases co-exist in stoichiometric BZN; 1:1 , 1:2 type of ordered phases, and a disordered matrix (figure 3.7).

3.2.3.2) Thermal History

As discussed in the above sections, high temperature annealing did not change the 1:1 type ordering, however, it did improve the 1:2 type ordering. The weight change of stoichiometric BZN annealed at 1400°C as a function of time is shown in figure 3.8. Since Zn is the only volatile species in this system, it is reasonable to relate this weight change to the loss of ZnO. The surfaces of annealed samples (1400°C, 100 hours) that were uncovered were significantly different from those that were covered with powder of the same composition (figure 3.9). Figure 3.10a shows the CDF image of stoichiometric BZN annealed at 1400°C for 100 hours. The finger type 1:2 type ordered domains were observed using a $(\frac{1}{3}\ \frac{1}{3}\ \frac{1}{3})_{s2}$ superlattice reflection. Notice that the nucleation of 1:2 type of ordering occurs preferentially along the grain boundary region. Microchemical analysis, however, was not able to resolve any significant chemical composition difference between the region containing 1:2 type ordered domains and the region containing 1:1 type ordered domains.

3.2.3.3) Zn/Nb Ratio Adjustment—Nb Rich BZN (BZNN)

In this case, samples with the formula

$$Ba(Zn_{1/3}Nb_{2/3})_{1-x}Nb_xO_3, \quad \text{where } x=0.5, 1, 2, 3, 9\%;$$
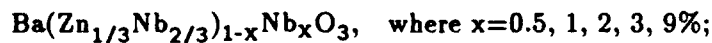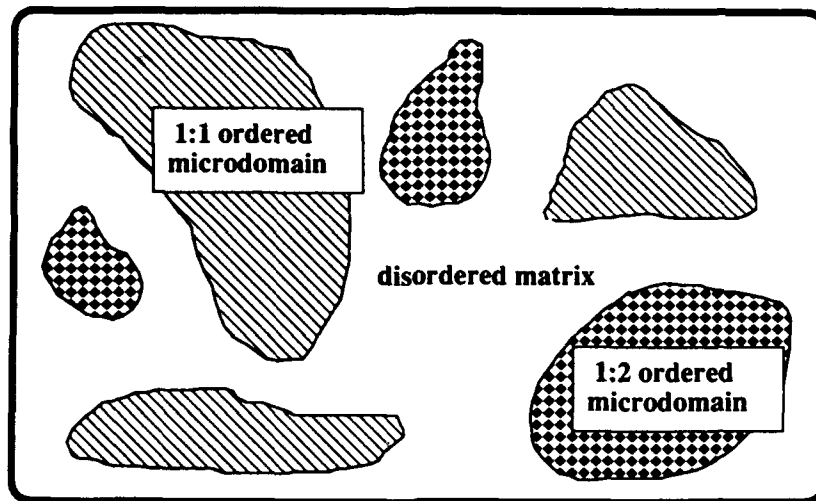
Figure 3.7 Ordering scheme in stoichiometric BZN.
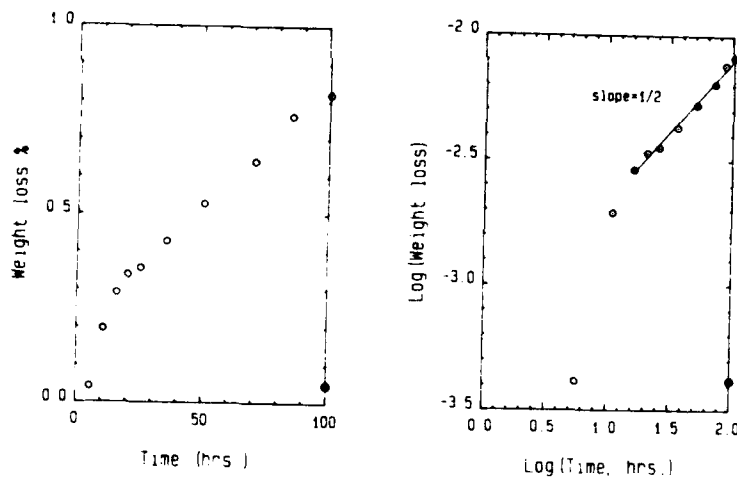
Figure 3.8 (a) Weight loss of stoichiometric BZN as a function of time after annealing at 1400°C. (b) Log (weight loss) vs log (time) for the same sample, showing a typical diffusional process (Shewmon, P.G., 1983). The filled circles designate the weight loss of the same sample covered with powder of the same composition during the annealing.

65
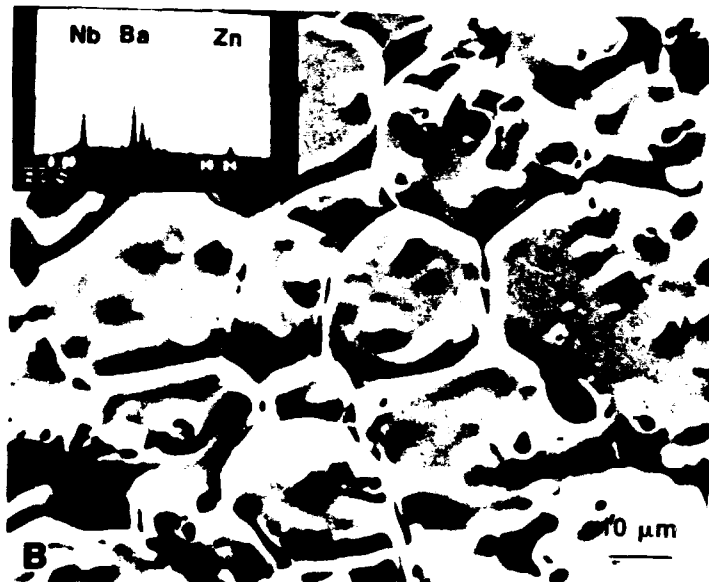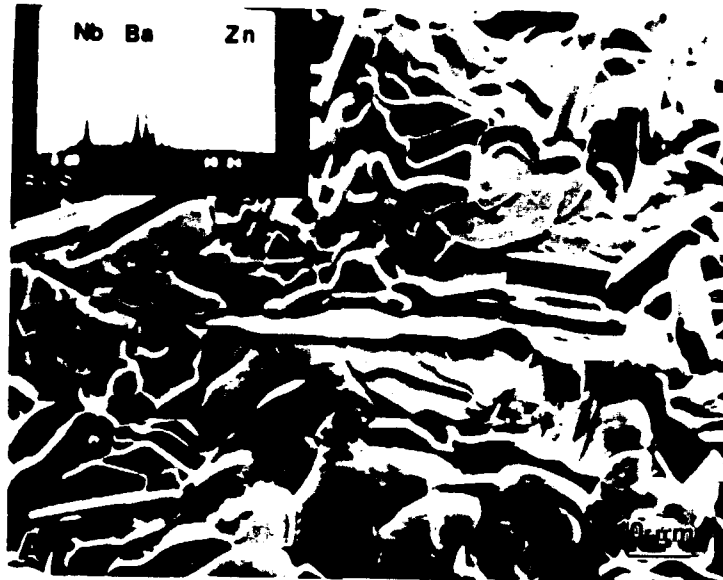
Figure 3.9 SEM SE images of stoichiometric BZN after annealed at 1400°C for 100 hours. (A) Sample without cover protection. (B) Sample covered with the powder of the same composition during the annealing. EDS analysis indicates the ZnO loss and formation of Nb rich second phase on the surface.
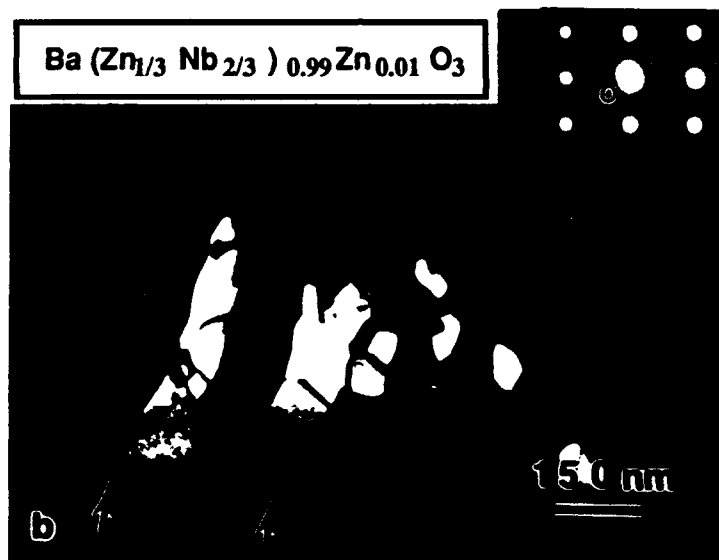
Figure 3.10 CDF images of (a) stoichiometric BZN and (b) $Ba(Zn_{1/3}Nb_{2/3})_{0.99}Zn_{0.01}O_3$ after annealed at 1400°C for 100 hours, showing a typical grain boundary nucleation of 1:2 type of ordered phase. The black arrows point at the grain boundaries.

favor the 1:2 type of ordering. As shown in figure 3.5, the degree of ordering increases with Nb concentration, and the ordered domains can also be controlled by heat treatment. The 1:2 type of ordered microdomains grow with increasing Nb concentration (figure 3.11) or high temperature annealing (figure 3.12). This behavior is different from the 1:1 type ordering in the BZNZ system, but it is consistent with the heat treatment results for stoichiometric BZN and BZNZ. The grain boundary nucleation of 1:2 ordered domains in BZN and BZNZ (figure 3.10) was believed due to Zn loss through the grain boundaries. The overall Nb rich BZNN resulted in APB's after annealing due to a nucleation and growth process (figure 3.12). The reason for the different behavior of the two types of ordered pattern can be attributed to three factors. Firstly, the charge imbalance in 1:1 type of ordered domains inhabits the domain coarsening and it does not exist in 1:2 type of ordered domains. Secondly, the diffusion path involved in the 1:2 type ordering is shorter than that in the 1:1 type ordering. This can be a great advantage for the 1:2 type of ordered domains to grow over the 1:1 type due to the difficulty of cation diffusion in the perovskite materials. Lastly, the existence of B-site cation vacancies due to the loss of ZnO during sintering and Nb rich also help this diffusion process for the 1:2 type ordering. However, the acceptor type vacancies (V_B'''') are not favored by the 1:1 type ordering because of the acceptor doped nature in the 1:1 ordered domains.

3.2.3.4) Analysis of SAEDPs and HRTEM

The 1:2 type of ordering in the $A(B'_{1/3}B''_{2/3})O_3$ system can be understood based on model 4. One B' and two B'' cations packing along the <111> direction of the perovskite structure (figure 1.3). Considering the 1:2 type of ordered phase as $Ba(Sr_{1/3}Ta_{2/3})O_3$ (BST, see Galasso, F., et.al., 1961), which has a space group $P\bar{3}m1$, we now analyze the SAEDPs (figure 3.5) as follows.

Since the 1:2 type of ordered trigonal phase is generated from a disordered cubic matrix, generally speaking, the orientation relationship between these two phases should be geometrically simple (Katz, L. et.al., 1964; Reynaud, P.F., 1976). As shown in figure 3.2, because $<100>_{ot}$ (ot stands for 1:2 type of ordered trigonal phase with space group $P\bar{3}m1$) and $<010>_{ot}$ // $<110>_{dc}$ (dc stands for disordered cubic phase with space group $Pm3m$), and the ordered packing layer along $<111>_{dc}$ is equivalent to $<001>_{ot}$, therefore, there are four possible variants of the 1:2 type ordered phase in the disordered matrix. In other words, four possible $<111>_{dc}$ directions can be used to generate 1:2
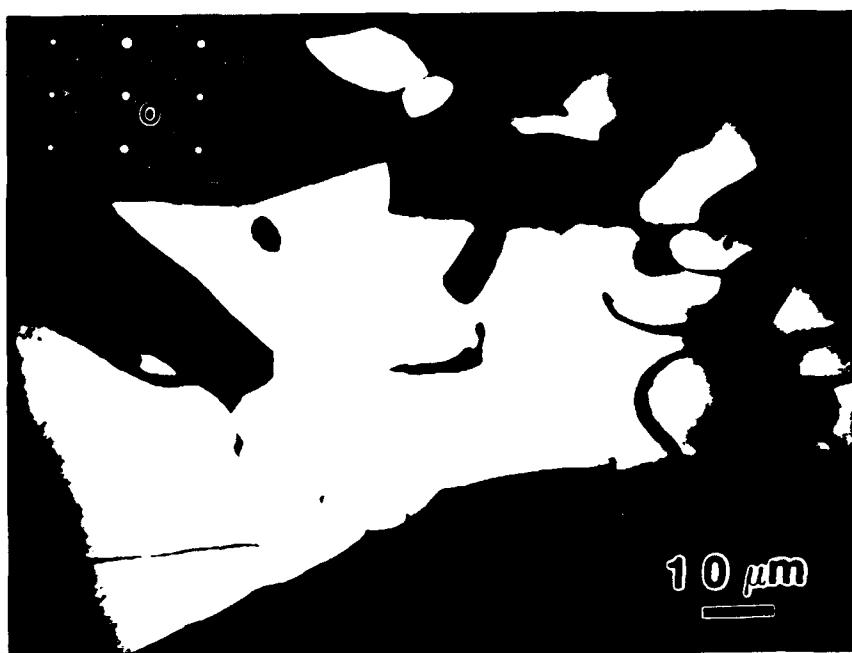
Figure 3.11 CDF image of $Ba(Zn_{1/3}Nb_{2/3})_{0.91}Nb_{0.09}O_3$ showing the coarsening of 1:2 type of ordered domains. Only one variant appears in SAEDP.
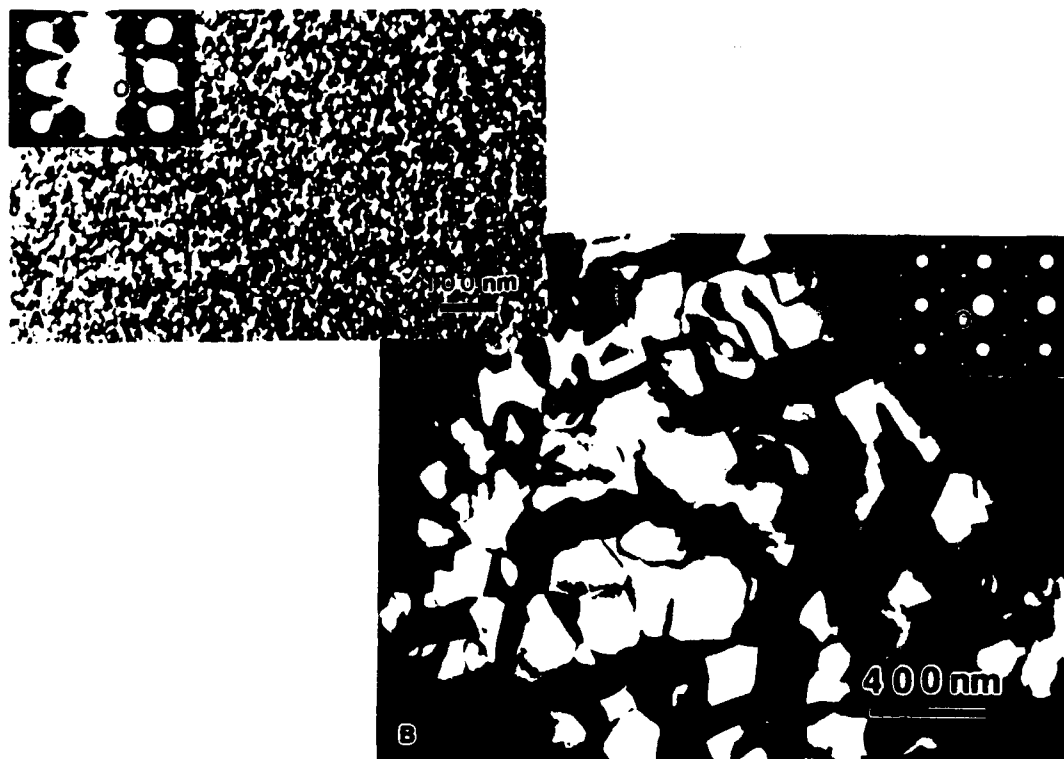
Figure 3.12 CDF image of $Ba(Zn_{1/3}Nb_{2/3})_{0.98}Nb_{0.02}O_3$ before (A) and after (B) annealed at 1400°C for 100 hours, showing the coarsening of 1:2 type ordered microdomains after annealing.

type ordered domains (see figure 3.13, 3.14 and table 3.3). Although there is no obvious group-subgroup relationship between the parent (Pm3m) and the child (P3̄m1) phases (Amelinckx, S., et.al., 1976; Buerger, M.J., 1978), the number of orientational variants can still be expressed as follows (Cahn, J.W., et.al., 198?; Tendeloo, G.V., et.al., 1974):

$$\text{number of variants} = \frac{n}{p} = \frac{48}{12} = 4$$

where n=number of point group operations in supergroup (i.e. Pm3m), and p=number of point group operations in the subgroup (i.e. P3̄m1). Four orientational variants are expected in this system which were indeed observed in the present study (figure 3.14). Figure 3.15 is a HRTEM micrograph of BZNN with x=2% recorded near the Scherzer defocus from $[110]_{dc} = [100]_{ot}$ or $[2\bar{1}\bar{1}0]_{ot}$ zone axis. Ordered domains with two different variants can be seen in this image. Laser ODM was used to check the orientation relationship. The laser beam was focused on the ordered domains with different variants in the HRTEM micrograph, and superlattice reflections with two different variants were revealed. With increasing Nb concentration, the 1:2 type ordered domains coarsen. Finally for x=9%, SAEDPs from an ordered domain shows only one variant (figures 3.5 and 3.11).

Up to now, only one Japanese research group has reported the 1:2 type ordering in BZN (Yoshioka, H., 1987). However, no detailed work has been reported. Desu and O'Bryan (Desu, S.B. and O'Bryan, H.M., 1985) proposed a model suggesting that Zn is lost at high temperatures in barium zinc tantalate, and the excess Ba would go into the Zn sites. This could be a reason for inducing 1:2 type of ordering, (i.e. due to large ionic radius difference), but our experimental results do not support this idea. The sample with 1% Ba doped in Zn sites (BZNB), shows the 1:1 type ordering without inducing any 1:2 type of ordered phase. Lecomte and Raveau (1981) have suggested model 3, that is, the 1:2 type of ordering could be originated from the B′-site, which can explain the mixture of two types of ordering in stoichiometric BZN. However, the results we obtained for Nb rich BZN challenge this model, because there is no reason for extra Nb to generate the 1:2 type of ordering if model 3 is correct. However, we could explain the co-existence of three phases in stoichiometric BZN based on model 2 and 4, and our experimental results. The 1:1 type ordered domains are rich in Zn (Zn/Nb ratio$>\frac{1}{2}$). In order to maintain overall charge balance, the system has to generate a Nb rich shell to
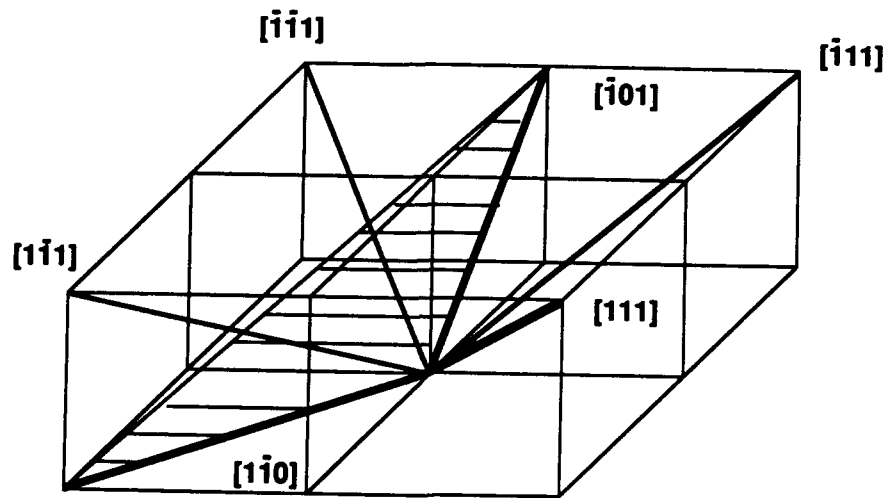
Figure 3.13 Four variants of the ordered trigonal phase in the disordered cubic matrix.

$$<\bar{1}01>_{dc} \longrightarrow <100>_{ot} \text{ or } <2\bar{1}\bar{1}0>_{ot} \quad \textit{angle:} \; (<\bar{1}01>_{dc} \; \& \; <1\bar{1}0>_{dc})= 120°$$

$$<1\bar{1}0>_{dc} \longrightarrow <010>_{ot} \text{ or } <\bar{1}2\bar{1}0>_{ot} \quad \textit{angle:} \; (<100>_{ot} \; \& \; <010>_{ot})= 120°$$

$$[111]_{dc} \longrightarrow [001]_{ot} \text{ or } [0001]_{ot}$$

variant 1	variant 2	variant 3	variant 4
$<1\bar{1}0>$	$<0\bar{1}1>$	$<101>$	$<011>$
$<\bar{1}01>$	$<110>$	$<\bar{1}10>$	$<\bar{1}01>$
$[111]$	$[\bar{1}11]$	$[\bar{1}\bar{1}1]$	$[1\bar{1}1]$

Table 3.3 Orientation relationship between four variants of the ordered trigonal phase and the disordered cubic phase.

72

Figure 3.14 SAEDPs of $Ba(Zn_{1/3}Nb_{2/3})_{0.98}Nb_{0.02}O_3$ with (A) [110], (B) [012] and (C) [113] zone axes, showing four variants.
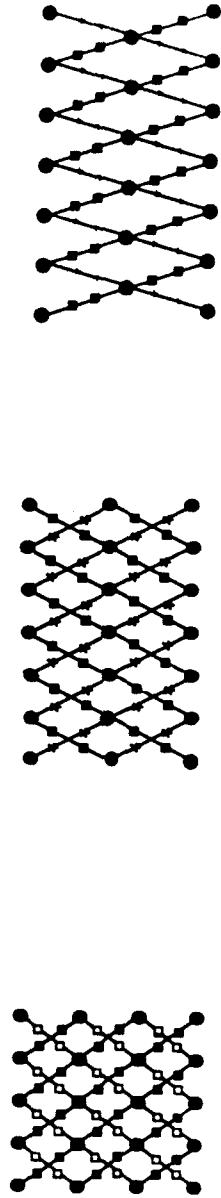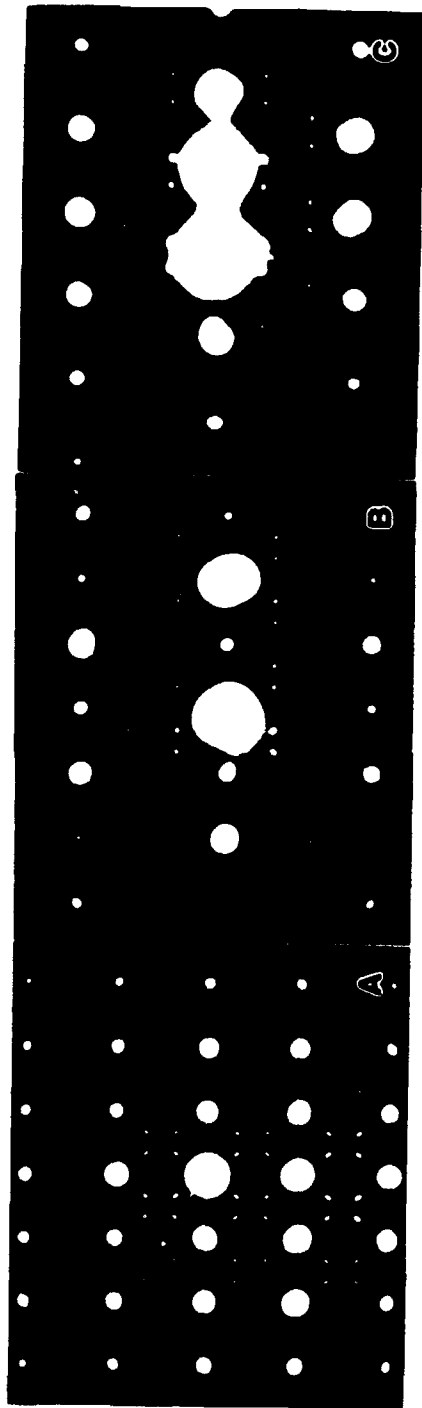
Variant: · 1 ■ 2 □ 3 ★ 4

Multivariants in SADPs with A) [110]; B) [012]; C) [113].
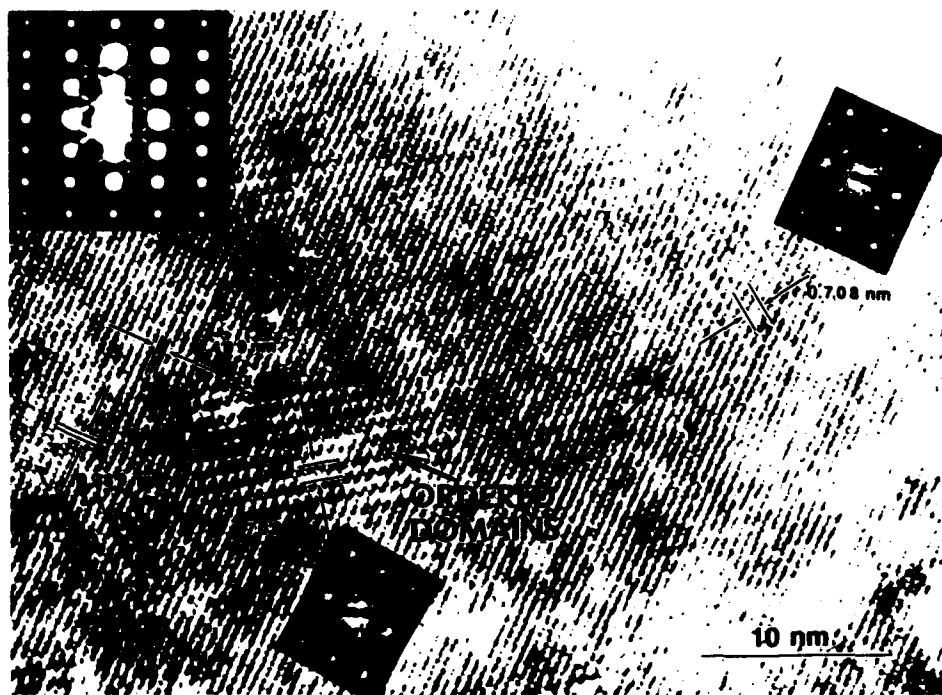
Figure 3.15 HRTEM BF (bright field) image of $Ba(Zn_{1/3}Nb_{2/3})_{0.91}Nb_{0.09}O_3$ taken from [110] zone axis at 300 kV with near optimum Scherzer defocus condition, showing 1:2 type ordered microdomains with two variants at this particular zone axis. The laser ODM patterns are taken from the HRTEM negatives.

compensate these regions. As we already know, Nb rich Nonstoichiometry pushes system to form 1:2 type ordering, therefore the system (stoichiometric BZN) would end up with three phases co-existing on a nanoscale. We will try to interpret the ordering behavior based on the defect chemistry later in the next chapter, but the exact reason why BZN prefers different types of ordering based on the Zn/Nb ratio is not clear at present.

3.3) *Summary*

(1) Stoichiometric BZN contains a mixture of 1:1 and 1:2 type of partially ordered domains and disordered matrix phases. The 1:1 type ordered domains (2~4 nm in size) are randomly distributed, and can be directly imaged by TEM using the CDF imaging technique. The degree of 1:1 ordering cannot be controlled by heat treatment due to the charge imbalance between the 1:1 type of ordered and disordered or 1:2 type of ordered regions, but can be promoted by lanthanum doping to reduce the charge effect. K doped into Ba site does not destroy the 1:1 type ordering, instead the system favors oxygen vacancy compensation as opposed to PMN. The intrinsic 1:2 ordered phase in stoichiometric BZN diffracts electrons too weakly to image the ordered domains using CDF imaging.

(2) The type of ordering in nonstoichiometric BZN depends on the Zn/Nb ratio. If the Zn/Nb ratio is greater than $\frac{1}{2}$, it prefers 1:1 type of ordering; if the Zn/Nb ratio is less than $\frac{1}{2}$, it favors 1:2 type of ordering.

(3) The 1:2 type of ordering is believed to be consistent with the chemical composition. The degree of 1:2 ordering can be controlled by making BZN Nb rich either by thermal loss of ZnO or by deliberately adding excess Nb. The SAEDPs of a series of Nb rich nonstoichiometric BZN samples can be explained by the formation of four possible variants of the ordered trigonal superstructure from a cubic matrix, which is in agreement with both experimental results and group theoretical formulations.

(4) High temperature annealing causes Zn loss which generates 1:2 type of ordering preferentially along the grain boundary region. This is supported by the results for nonstoichiometric BZN. The reason why high temperature annealing has different effect on two types of ordered phases can be understood based on the charge imbalance in the 1:1 ordered microdomains, existence of B-site cation vacancies and difficulty of cation diffusion in the perovskite lattice as well.

Chapter 4 <u>DEFECT</u> <u>CHEMISTRY</u> of <u>BZN</u>

In order to gain a comprehensive understanding about the model system BZN, it is logical to first study the transition from BT to BZN in terms of structure, defect chemistry and dielectric properties. A study of the similarities and differences between these two parallel systems would make a rather interesting contribution in terms of an understanding of the interrelationship between the microstructure, defect chemistry and electrical properties of complex perovskites. In the solid solution system BT-BZN, two end members have different microstructures but are closely related in terms of defect structure and dielectric properties. The structural part of one end member BZN has been dealt with in detail in chapter 3. The study of the transition from a simple perovskite (BT) to a complex perovskite (BZN) as Ti is generally replaced by $Zn_{1/3}Nb_{2/3}$ with general formula $BaTi_{1-x}(Zn_{1/3}Nb_{2/3})_xO_3$ will provide useful information for the understanding of defect chemistry of the complex system BZN. It is therefore the first task to study the defect chemistry, dielectric and structural properties in the solid solution BT-BZN. The detailed defect chemistry study of the complex system BZN will follow these discussion logically.

4.1) *Transition from Simple to Complex Perovskite*

4.1.1) Acceptor (Zn) and Donor (Nb) Doped BT

Starting materials TPT, $BaCO_3$, $ZnNO_3$, and Nb-ethoxide (purity>99.99) were used. The liquid mix technique was used for this part of study. Organic gels were calcined at 850°C for 3 hours, and the resulting ceramic powders were subsequently cold-pressed at 77 MPa and sintered at 1400°C for 3 hours in air. Final relative densities in the range of 90-98% of theoretical density were achieved for all samples. The density was measured using the standard buoyancy method. The XRD pattern showed a single phase for samples without exceeding the solubility limit. Grain size varied from 0.5 μm to 100 μm depending on the type and level of doping.

4.1.1.1) High Temperature Equilibrium Electrical Conductivity

High temperature equilibrium DC conductivity of rectangular bars (1.5 by 5.5 by 14 mm, see figure 2.1) were measured with the standard four-point DC technique using Pt electrode. The high and low ranges of oxygen partial pressures were achieved with O_2, pre-mixed Ar_2-O_2 and $CO-CO_2$ gas mixtures. The intermediate P_{O_2} range was

76

monitored by use of a calcia-stabilized zirconia cell for measuring the oxygen activity adjacent to the sample. All measurements were repeated at least twice from high to low and back to high oxygen partial pressure to assure the reproducibility within 5%. Each time the temperature and/or P_{O_2} level was changed, a waiting period was allowed to achieve equilibrium. For some donor doped samples, the time to reach true equilibrium was extremely long (>48 hours). The recording of the data was therefore based on a change of the reading with time not exceeding $1\mu V/hr$. which is less than 0.5% of the voltage drop across the sample.

Figure 4.1 shows a plot of Log(σ), versus Log(P_{O_2}) for undoped and Zn doped BT, illustrating typical behavior for acceptor doped BT. Note that both n-type and p-type conductivity appear within the experimental P_{O_2} range, and the increase of p-type and decrease of n-type conductivity corresponding to the shift in the conductivity minimum as Ti is replaced by Zn. It can be concluded that the apparent solubility limit for Zn substitution on Ti site is approximately 1%. This was further substantiated by SEM images (Figure 4.2) of polished and thermal etched samples. Large amounts of a second phase in the 2% Zn-doped sample clearly indicate that 2% excess Zn cannot be accommodated by the lattice through the formation of oxygen vacancies. The Nb-doped BT shows a straightforward donor doping behavior. It has been reported that the solubility limit for donor dopants in BT can be quite high (Daniels, J., et.al., 1976). For instance, Nb substitution for Ti in BT can reach about 14% (Subbarao, E.C., et.al., 1959). Two doping levels were studied. The plot of Log(σ) versus Log(P_{O_2}) at 1300°C for these samples is shown in figure 4.3. As can be seen, the low doping level, 600 ppm, can be explained using the model described in the previous section. For the heavily doped case, such as 3%, the overall charge neutrality condition switched from electronic to ionic compensation by introducing V_{Ti}'''' (Chan, H.M., et.al., 1985). The detailed defect chemistry for the heavily donor doped case will be discussed in section 4.3.4 and chapter 6.

4.1.1.2) Dielectric Measurements

Temperature and frequency spectrum of the dielectric constant of undoped, acceptor- and donor-doped BT are shown in figures 4.4 and 4.5, respectively. Dielectric constant relaxation behavior did not show much difference in the case of Zn doped BT except that the magnitude of the dielectric constant drops with increasing Zn content. On the other hand, Nb doped BT changes the dielectric constant drastically. The
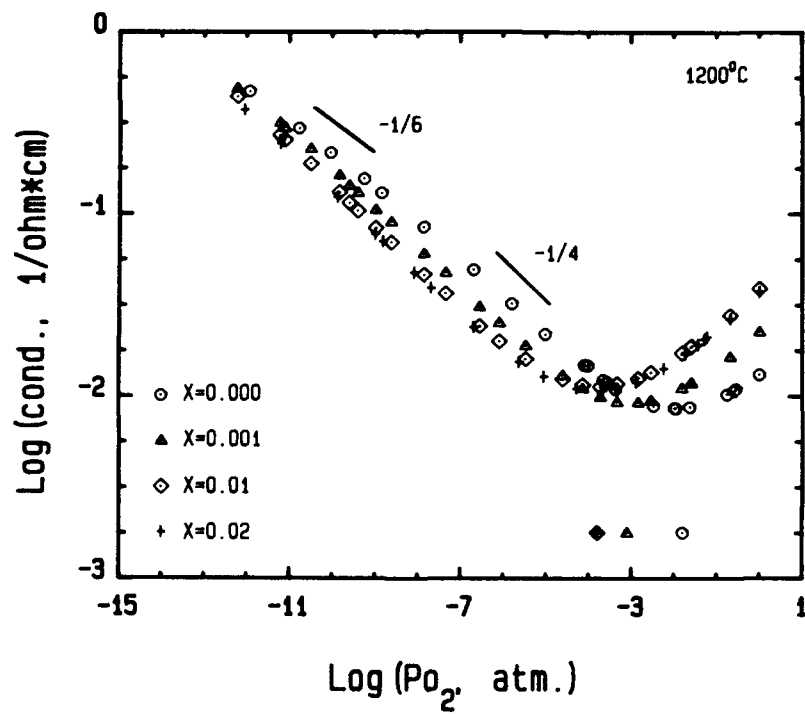
Figure 4.1 Logarithm of high temperature equilibrium DC conductivity of $BaTi_{1-x}Zn_xO_3$ as a function of logarithm of oxygen partial pressure at 1200°C. The minimum positions are marked by the symbols of each corresponding x value.
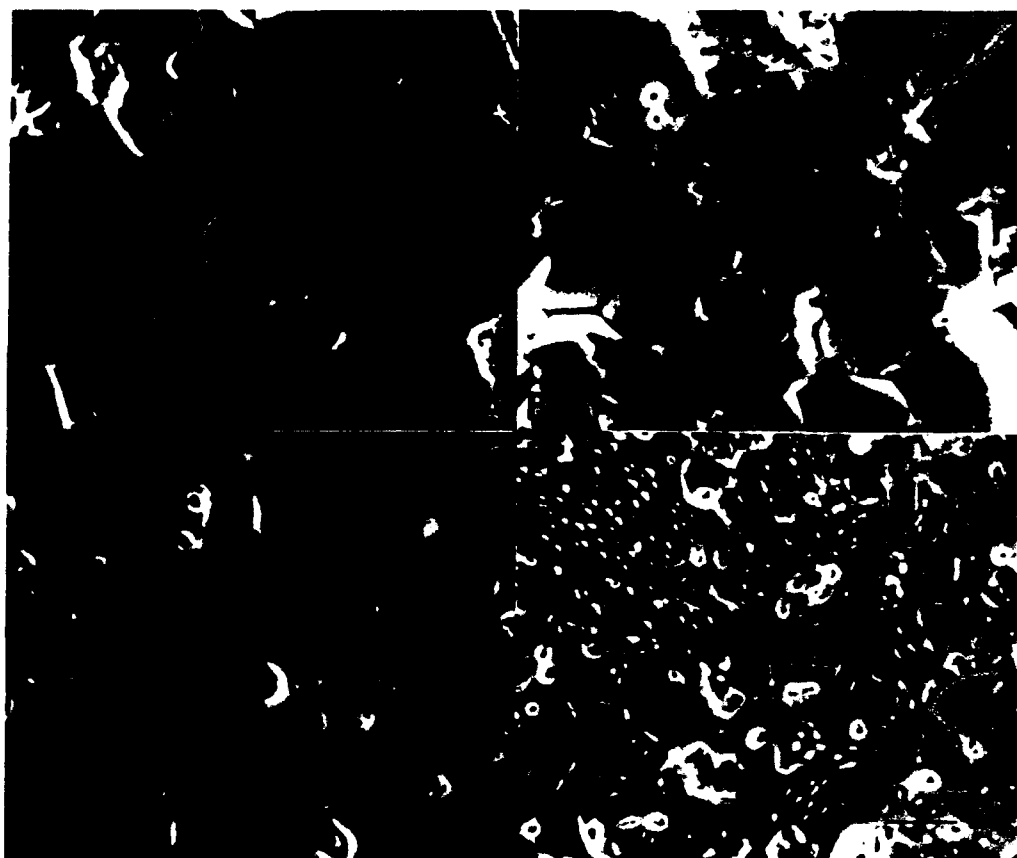
Figure 4.2 SEM secondary electron (SE) images of $BaTi_{1-x}Zn_xO_{3-x}$ with x=0.00 (A), x=0.0003 (B), x=0.001 (C), and x=0.02 (D). Sample were thermally etched at 1200°C for half an hour.
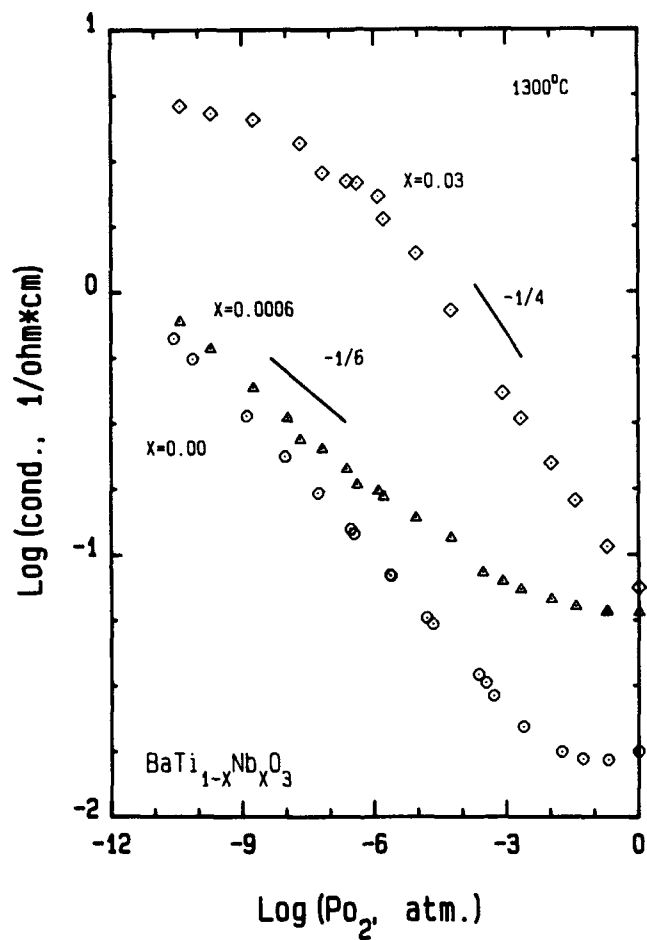
Figure 4.3 Log(σ) of $BaTi_{1-x}Nb_xO_3$, with x=0.00, x=0.0006 and x=0.03, as a function of log(P_{O_2}) at 1300°C.
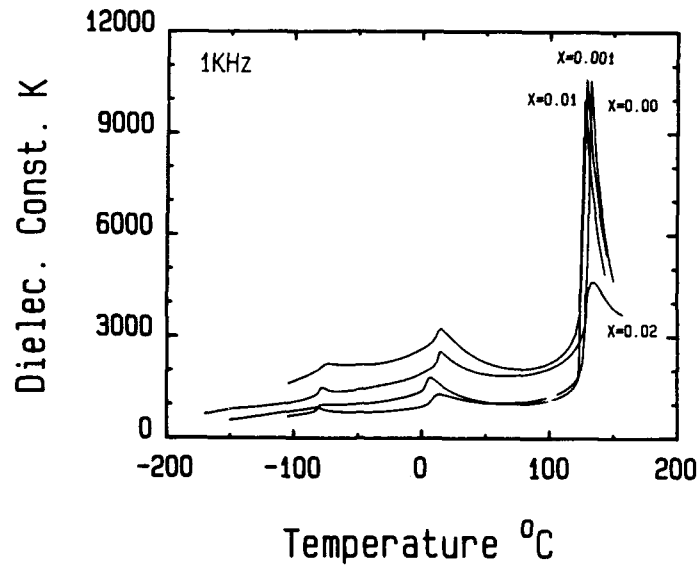
Figure 4.4 Temperature spectrum of dielectric constant for $BaTi_{1-x}Zn_xO_{3-x}$, measured at 1 kHZ.
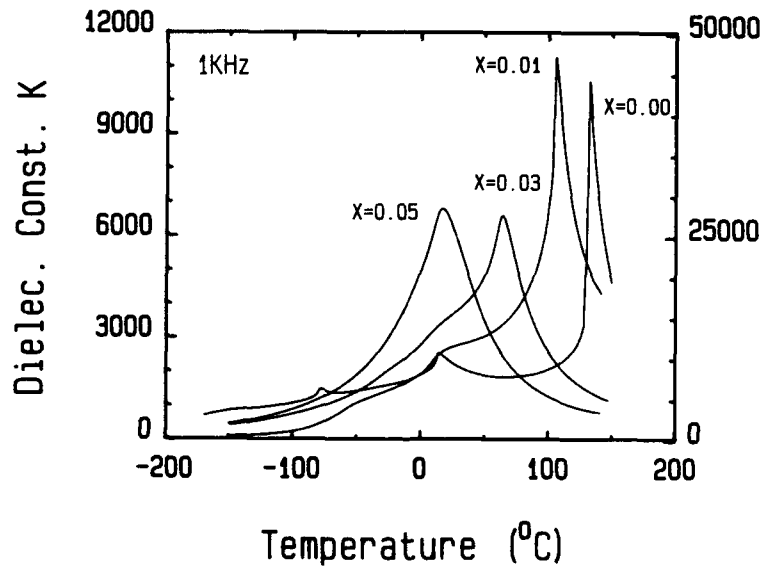
Figure 4.5 Temperature spectrum of dielectric constant for $BaTi_{1-x}Nb_xO_3$, measured at 1 kHZ.

81

transition from the paraelectric to ferroelectric phase become diffuse with increasing Nb substitution. This is common for donor doped BT.

4.1.1.3) Site Occupancy of Zn in BT

According to the $ZnO-TiO_2$ phase diagram (Figure 4.6) proposed by Dulin, F.H., et.al., (1960), a $ZnTiO_3$ line compound was observed to be stable above 560°C and to have a maximum stability temperature of about 945°C $\pm$ 25°C under hydrothermal conditions or about 925°C $\pm$ 25°C under dry conditions. It decomposes to form the orthotitanate and rutile. Whether Zn can go to the Ba site in our case due to an uncertainty in the Ba/Ti ratio is in question. Sinyakov, E.V., et.al., (1967) claimed that, in the system $(1-x)BT + xZnO$, the Curie temperature (Tc) was shifted to lower temperatures with increasing x (figure 4.7). There are two features which are in conflict with our findings. First, for the system $(1-x)BT + xZnO$, Sinyakov claimed that Zn occupied Ba sites. Second, up to x = 0.66, they reported that the Curie temperature dropped to ~80°C. We did not observe such a large shift. In order to clarify those contradictions, a series of experiments were carefully designed as follows:

Sample I. undoped $BaTiO_3$

Sample II. $BaTiO_3 + 0.005\ ZnO$

Sample III. $Ba_{0.995}Zn_{0.005}TiO_3$

Sample IV. $BaTi_{0.995}Zn_{0.005}O_3$

$Log(\sigma)$ vs $Log(P_{O_2})$ at 1200°C was measured for all these samples, and the results are shown in figure 4.8. As can be seen, there is no significant difference between samples I and III. However, samples II and IV are almost the same but different from sample I. This implies that Zn does not occupy the Ba site. The reasons are as follows: First, Zn substitution for Ba does not generate any charge imbalance, but Zn substitution for Ti will lead to the formation of oxygen vacancies. This in turn could result in the typical change in $Log(\sigma)$ vs $Log(P_{O_2})$ plot at constant temperature. Secondly, if Zn does occupy the Ba site and form a solid solution between $ZnTiO_3$ and BT, and the probability of Zn occupying Ba and Ti sites is the same, samples II and IV should behave differently in terms of the conductivity minimum shift. Apparently, this is not the case. Thirdly, if Zn can not be accommodated on the Ba site and the composition is formulated assuming that Zn occupies Ba sites, a Ti rich second phase would result since the cation nonstoichiometry would have been exceeded (Chan, N.H., et.al., 1982; Hu, Y.H., et.al., 1986). The SEM images of chemically etched polished
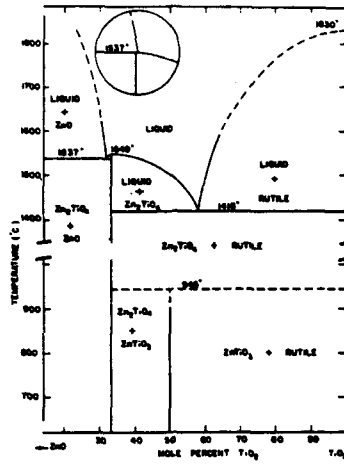
Figure 4.6 ZnO−TiO$_2$ Phase diagram. Inset shows alternative incongruent melting of Zn$_2$TiO$_4$ (from Ref. Dulin, F.H., et.al., 1960).
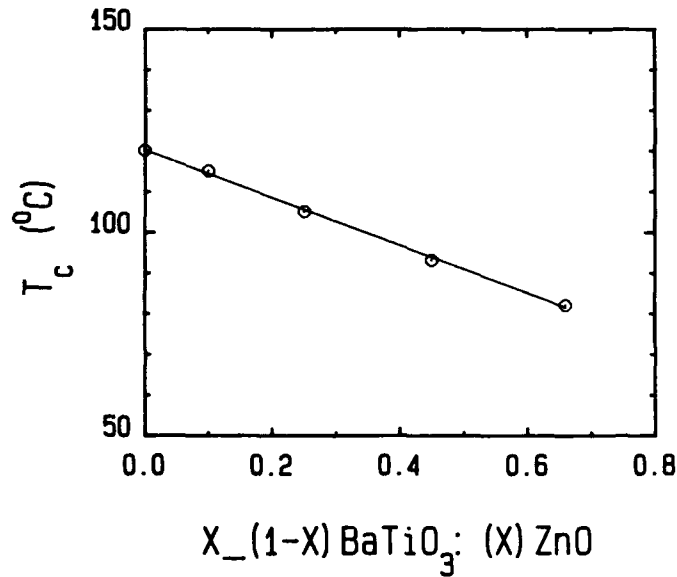
Figure 4.7 The Curie temperature shift with increasing x for the sample with formula (1-x) BT + x ZnO (from Ref. Sinyakov, E.V., et. al., 1967).
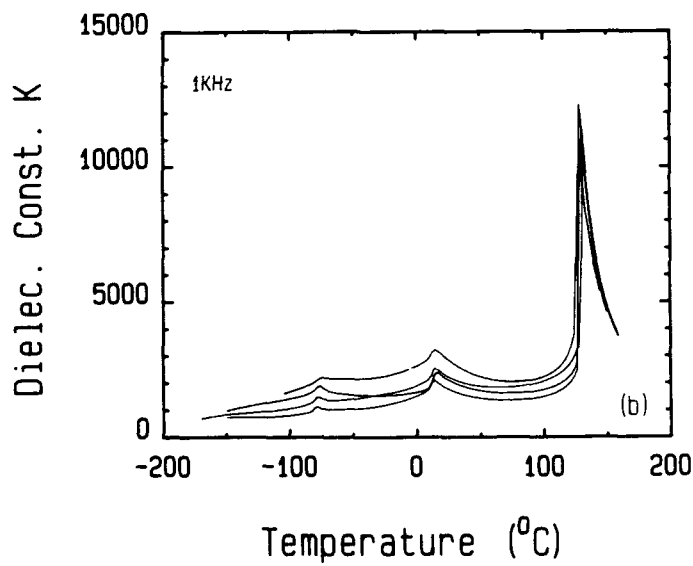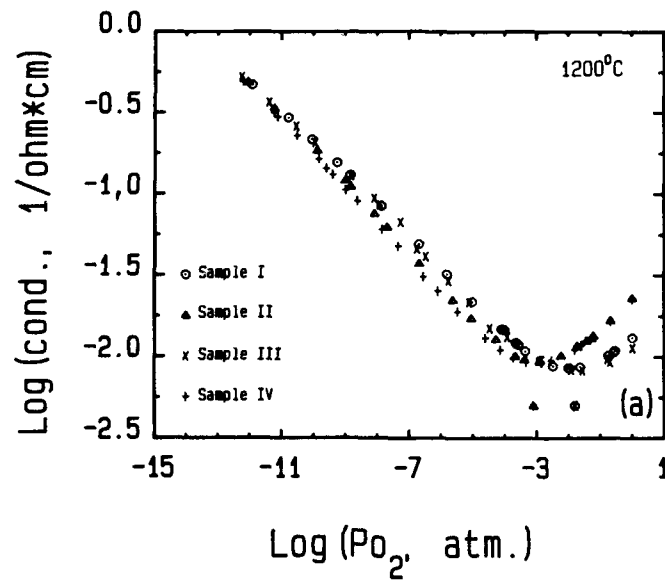
Figure 4.8 (a) Log(σ) of sample I through IV as a function of log(P_{O_2}). The minimum points are marked by the symbols corresponding to each sample. (b) Dielectric constant vs temperature for the same samples, measured at 1 kHz.

surfaces of samples II and III show different amounts of Ti rich second phase (Figure 4.9). Substitution of Ti by Zn results in the formation of a Ti rich second phase due to excess TiO_2 in the starting composition. The amount of excess TiO_2 in sample III is larger than that in the sample II, this therefore causes a large amount of Ti rich second phase which is what was observed experimentally.

In conclusion, Zn can only substitute for Ti as an acceptor which can be accommodated by the formation of oxygen vacancies. Zn substitution for Ti does not shift the Curie temperature by a large amount. In the case of Sinyakov's results, although they claimed to use barium titanate oxalate of special purity instead of analytical grade $BaCO_3$ and TiO_3, the Remeika method (Remeika, J.P., 1954) they used for growing single crystals from the melt of KF flux of analytical grade could introduce substantial foreign impurities. This could drastically affect the dielectric properties (Jaffe, B., et.al., 1971; Ceramic Source, 1986, 1988). It is reasonable to suspect that the large Curie temperature shift in their case could have resulted from impurities other than Zn.

4.1.2) Zn and Nb Co-doped BT

For this part of the work, samples with the general formula $BaTi_{1-x}(Zn_{1/3}Nb_{2/3})_xO_3$ were prepared using either the liquid mix technique for $x \leq 0.09$ or the conventional ceramic processing method for $x > 0.09$. Table 4.1 lists the experimental conditions for this series of samples. Calcined powders were cold-pressed into pellets at 77 MPa. Some samples were subsequently isostatically cold-pressed at 280 MPa. All of the samples were sintered in the temperature range of 1400 to 1600°C for 3 hours depending upon the value of x. The final fired ceramic products all reached 90 to 98% of theoretical density.

4.1.2.1) XRD, DSC and Microstructural Characterization

X-ray powder diffraction was carried out for a series of samples with different x values. NIST high purity Si powder was used as an internal standard. The lattice parameter was calculated from high angle reflections (Cullity, B.D., 1978). Figure 4.10 shows the lattice parameter against x at room temperature. The tetragonality decreases with increasing x value. Around $x = 0.1$, the structure becomes cubic. The typical tetragonal phase with ferroelectric domain structure in undoped BT (figure 4.11) turns into a cubic phase with ordered microchemical domains in undoped BZN. The detailed
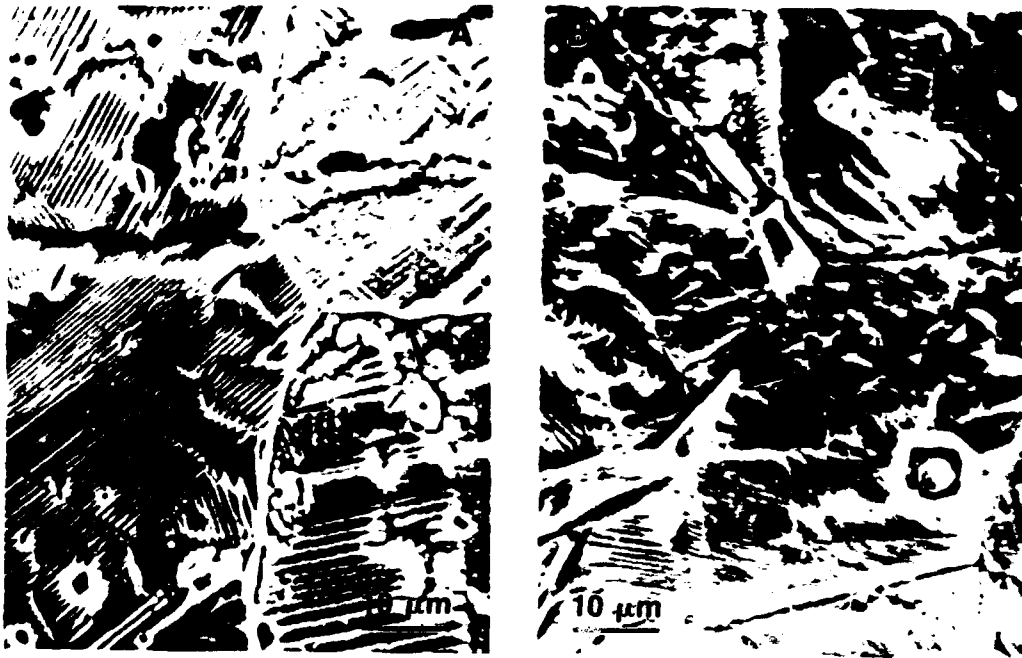
Figure 4.9 SEM SE images of sample II (A) and III (B), showing more Ti rich second phase in (B) than in (A).

Sample #	X	Grain size	sintering Temp.(°C) (for 3 hours)	calcining Temp. (°C)/hrs.
000	0.000	20~100 μm	1400	900/3
201	0.015	2~5 μm	1400	900/3
203	0.03	2~4 μm	1400	900/3
303	0.06	0.5~1 μm	1450	900/3
304	0.09	0.5~2 μm	1450	900/3
305	0.18	0.5~2 μm	1500	1000/10
401	0.3	2~4 μm	1500	1000/10
402	0.6	2~4 μm	1500	1000/10
403	0.9	2~6 μm	1560	1000/10
500	1.0	4~10 μm	1600	1000/20

Table 4.1 Experiments on Zn/Nb co-doped BT ($BaTi_{1-x}(Zn_{1/3}Nb_{2/3})_xO_3$)
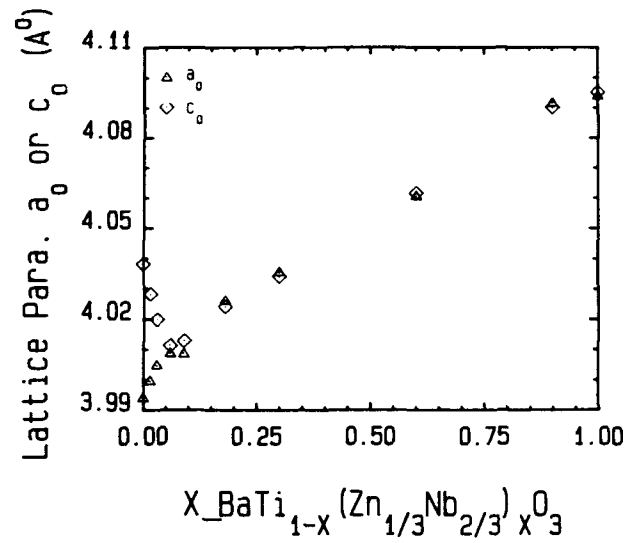
Figure 4.10 Lattice parameter change as a function of x in $BaTi_{1-x}(Zn_{1/3}Nb_{2/3})_xO_3$. Noticing that at room temperature, the loss of tetragonality is around x=0.09.
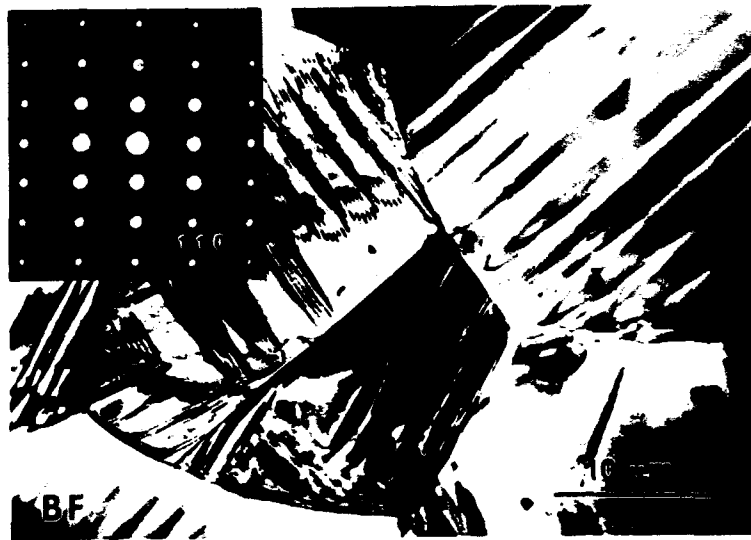
Figure 4.11 TEM bright field (BF) image and SAEDP of undoped BT in the tetragonal phase, showing a typical ferroelectric domain structure.

microstructural characterization has be discussed in the chapter 3. Figure 4.12 shows a typical DSC plot of heat flow of a crushed ceramic sample against a standard as a function of temperature. The latent heat at the Curie temperature was calculated from the area under the transition peak corresponding to each paraelectric to ferroelectric transition point. The calculated latent heat is plotted versus x shown in figure 4.13. This transition enthalpy decreases with increasing x, approaching zero at $x \cong 0.09$. It is well known that the first order phase transition is associated with a release of latent heat (Porter, D.A., et.al., 1984; Devonshire, A.F., 1954). Therefore one might be able to estimate the nature of the paraelectric to ferroelectric phase transition in this system. Above $x \cong 0.09$, the latent heat is smeared out and difficult to be detected because the heat flow curve at the transition point becomes a gradual change instead of a distinct peak. The lost of latent heat at about $x \sim 0.09$ is in agreement with dielectric measurements that will be discussed in the section 4.1.2.3..

4.1.2.2) High Temperature Equilibrium Electrical Conductivity

A series of $Log(\sigma)$ versus $Log(P_{O_2})$ plots at 1200°C for different x values is shown in figure 4.14(a). It is apparent that all of the curves are identical except that the absolute conductivity value decreases with increasing x value. The minimum of each curve depends on the relative acceptor level, specifically the Zn/Nb ratio in this Zn/Nb co-doped BT which is of no significant interest for the present study. However, the shape of the reduction and oxidation portion of the curves indicates that the same reduction and oxidation reaction can be applied to all these compositions with different x. It is therefore reasonable to assume that the BT-BZN solid solution has a similar defect structure. The Arrhenius plot of conductivity minimum for four selected x values is shown in figure 4.14(b). The activation energy increases with increasing x value. It is well known that BT is a large polaron type conductor (Choi, G.M. and Tuller, H.L., et.al., 1986). In the case of band type and large polaron conduction, this thermodynamic analysis using $Log(\sigma)_{min.}$ versus $1/T$ is valid for estimation of indirect band gap $E_g^{(o)}$ at 0 K (Long, S.A. and Blumenthal, R.N., 1971; Kofstad, P., 1983). For the BT-BZN solid solution, it is not fair to estimate the band gap from this analysis before the electrical conduction mechanism is clear. A detailed transport property study will be dealt with in chapter 5. Since the defect structure is essentially similar for all x values, the general trend of the phenomenological activation energy ($E_g^{(o)}$ + ΔH_{motion}) increasing with x is as expected.
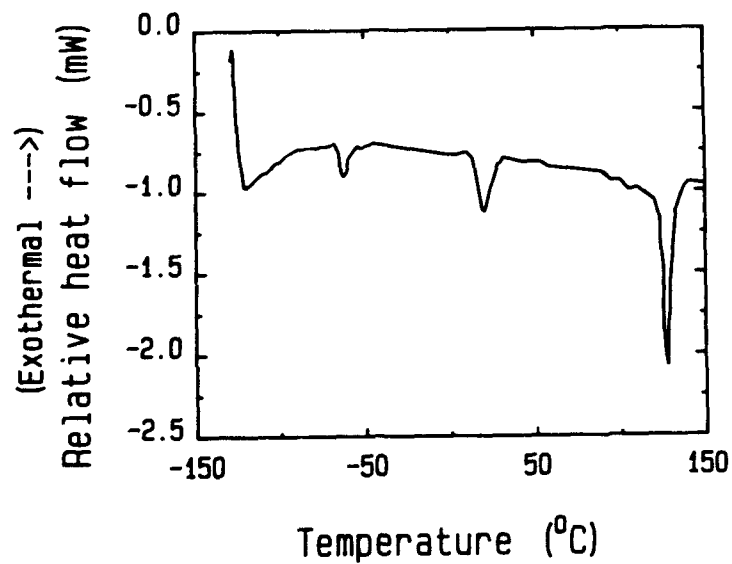
Figure 4.12 Relative heat flow as a function of temperature for undoped BT, showing three endothermal transition peaks corresponding to three first order phase transitions.

$X: Ba (Zn_{1/3}Nb_{2/3})_x Ti_{1-x}O_3$
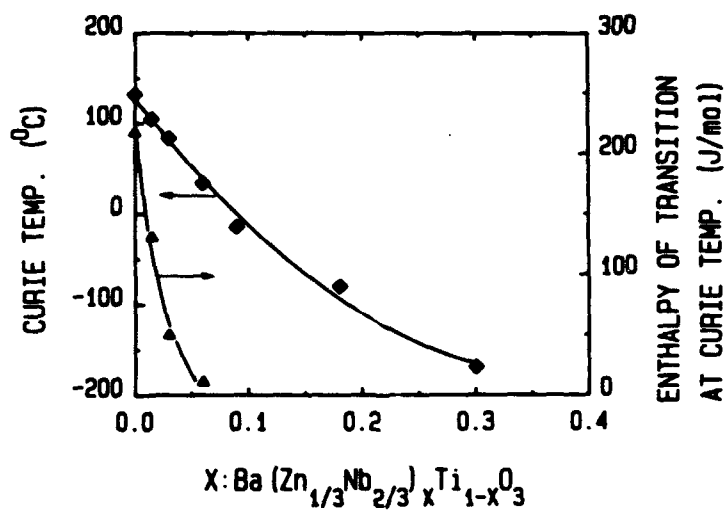
Figure 4.13 The Curie temperature obtained from temperature spectrum of dielectric constant and the enthalpy of transition at the Curie temperature determined from DSC measurements as a function of x in $BaTi_{1-x}(Zn_{1/3}Nb_{2/3})_xO_3$.
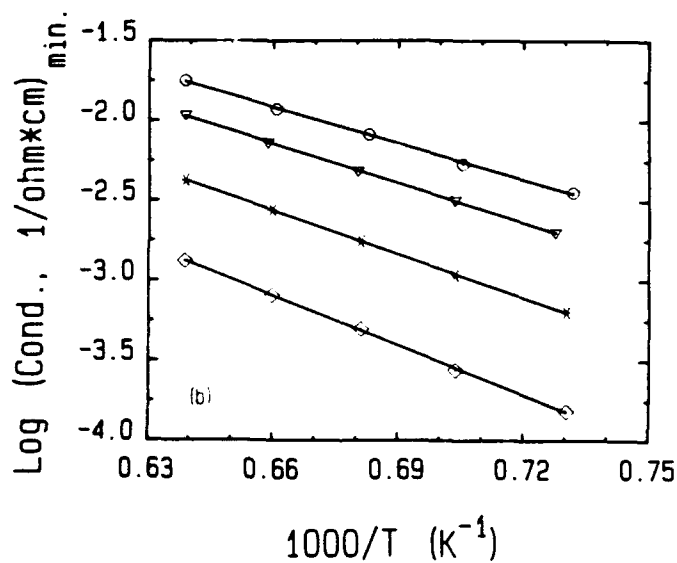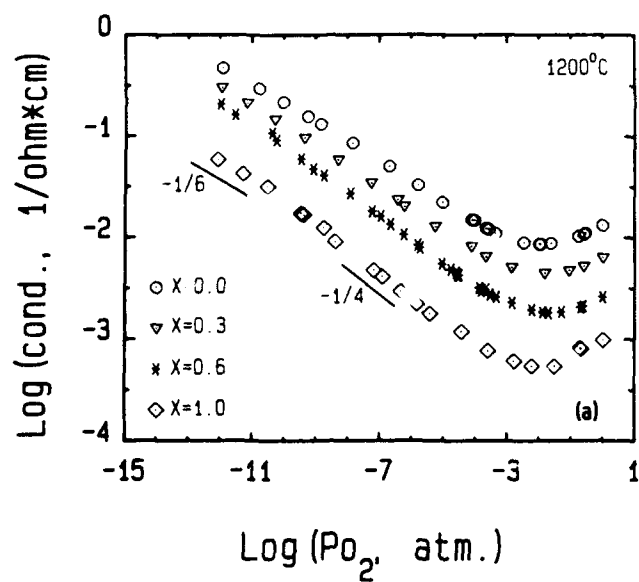
Figure 4.14 (a) Log (σ) vs log (P_{O_2}) for samples $BaTi_{1-x}(Zn_{1/3}Nb_{2/3})_xO_3$, showing the similar shape of profile. (b) Arrhenius plot of conductivity minimum of a series of samples in (a), showing a increase of phenomenological activation energy with x value which are 2.95 eV for x=0.00, 3.20 eV for x=0.30, 3.50 eV for x=0.60 and 4.28 eV for x=1.00.

91

Figure 4.15 shows 3 isothermal plots of Log(σ) versus Log(P_{O_2}) for 100%substitution of Ti by Zn/Nb with 1/2 ratio. A comparison of Log(σ) versus Log(P_{O_2}) at 1300°C for undoped BZN, acceptor doped and donor doped BZN is also shown in figure 4.16. Again, comparing with BT, it is obvious that both systems have the similar defect structure. The details will be discussed later in this chapter.

4.1.2.3) Dielectric Measurement

Dielectric relaxation measurements were carried out for a series of samples with different value of x in the frequency range from 100Hz to 100kHz and temperature range from -150°C to 200°C. The measurements were usually conducted during the cooling run to avoid the influence of ice formation on the samples with a lower dielectric constant and dissipation factor, such as the samples towards the BZN rich side. The cooling rate was -1°C/min.. The dielectric constant temperature spectra are shown in figure 4.17. As can be seen, with increasing x, the three transition points and three corresponding dielectric constant maxima move close together and finally coalesce at x $\cong$ 0.09 into a single broad maximum. The Curie temperature shifts to lower temperature with increasing x (figure 4.13). Finally an essentially temperature and frequency independent dielectric constant was observed.

4.1.3) Discussion of Results

A complete solid solution is formed between BT and BZN (general formula $BaTi_{1-x}(Zn_{1/3}Nb_{2/3})_{1-x}O_3$). The interesting properties are summarized as follows:

(1) The Curie temperature as determined from dielectric measurements decreases gradually as x increases. This is in agreement with DSC and XRD results.

(2) The three transition temperatures of BT coalesce.

(3) A single broad transition peak for x $\geq$ 0.09 results with a typical frequency relaxation phenomenon (see the inset in figure 4.17). This implies that the transition from paraelectric to ferroelectric could be second order. The latent heat obtained from DSC measurements is consistent with this result.

(4) At room temperature, progressing from BT to BZN, the typical tetragonal phase with ferroelectric domain structure finally turns into a paraelectric cubic phase with mixed microchemical ordered domain structure.

To fully understand why the system behaves this way, further experimental work is required which will be described in chapter 8. A qualitative and phenomenological

92
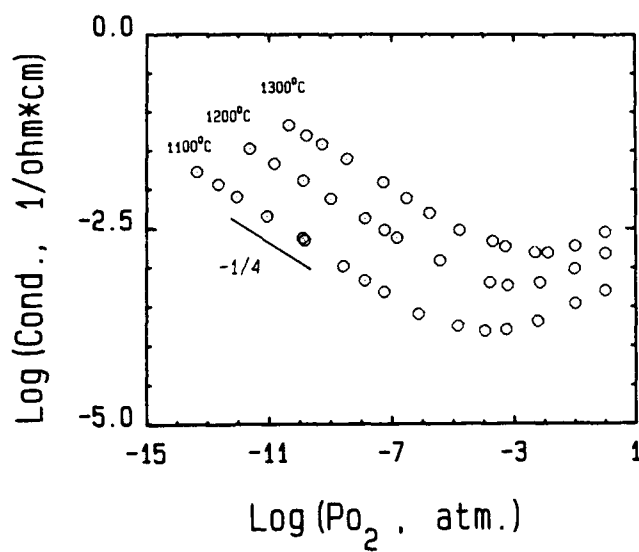
Figure 4.15 Log (σ) of stoichiometric BZN as a function of Log (P_{O2}) for three isotherms.
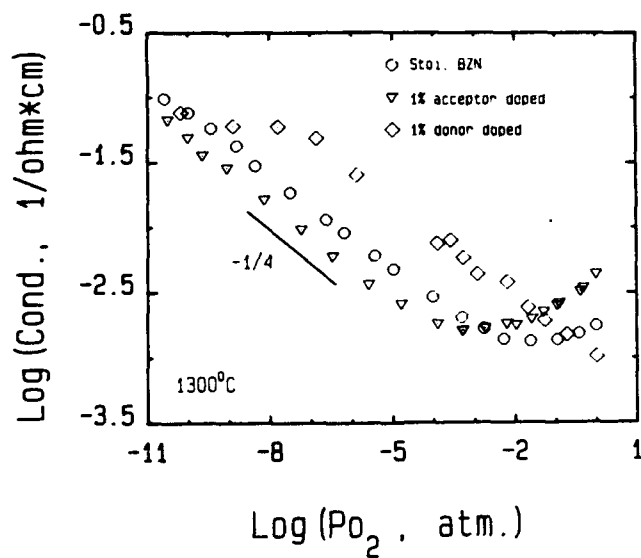
Figure 4.16 Log (σ) as a function of log (P_{O2}) for stoichiometric, 1% acceptor doped and 1% donor doped BZN. Measurement was taken at 1300°C.
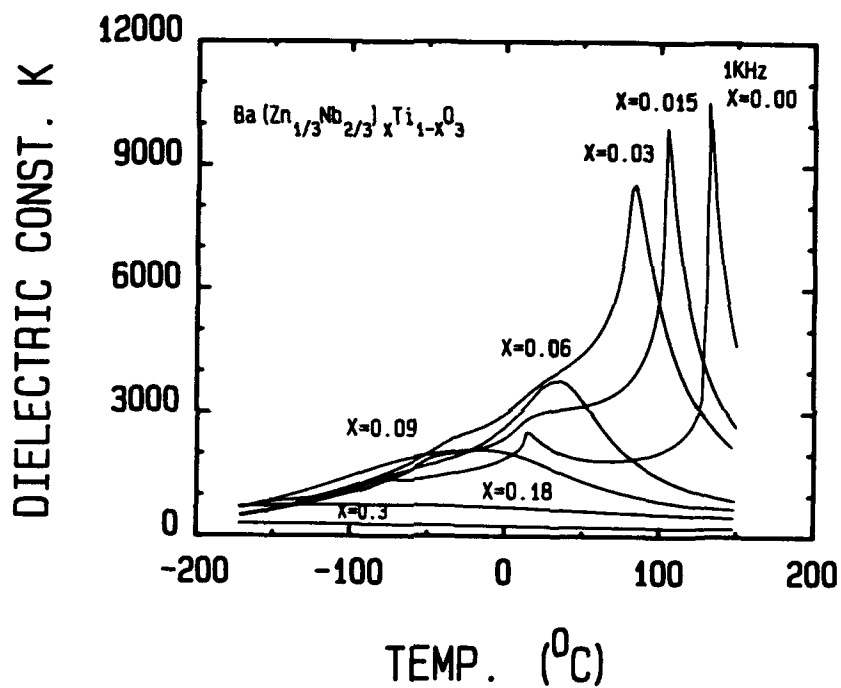
Figure 4.17 (I) Temperature spectra of dielectric constant for samples with general formula $BaTi_{1-x}(Zn_{1/3}Nb_{2/3})_xO_3$ at 1 kHz.
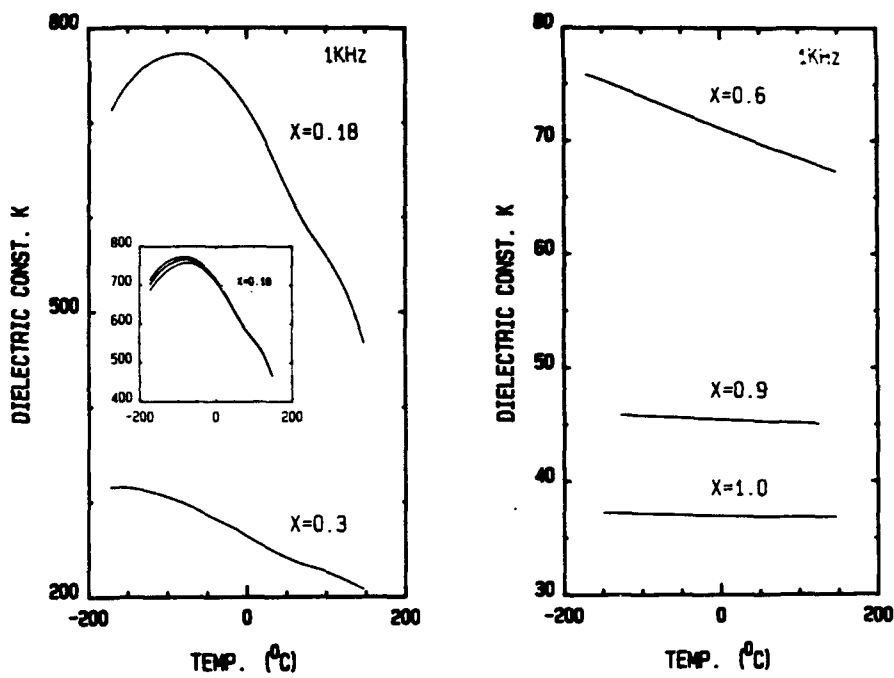
Figure 4.17 (II) Temperature spectra of dielectric constant for samples with general formula $BaTi_{1-x}(Zn_{1/3}Nb_{2/3})_xO_3$ at 1 kHz. Inset illustrates a typical frequency relaxation of dielectric constant of the sample with x=0.18.

95

explanation will be given here based on the experimental work from the open literature and our work. All discussions will be focussed on the various substitutional ions for Ti on the B sites with fixed Ba content as A site cation.

It is well known that the Curie temperature of BT doped with foreign ions on the B site generally decreases (table 4.2). Some cation substitutions do not change the Curie temperature as much, such as Mg^{+2} (Baxter, P., et.al., 1957) and Zn^{+2} (present work). A few ions can increase T_c, such as Si^{+2} (Marks, G.W., et.al., 1955) and Cu^{+2} (Sakudo, T., 1957). Very little work on the self-compensated doping case has been published; for example, $Mn_{1/3}Nb_{2/3}$, $Co_{1/3}Nb_{2/3}$, $Ni_{1/3}Nb_{2/3}$ (Sinyakov, E.V., et.al., 1960), and $Fe_{1/2}Ta_{1/2}$ (Nakamura, T., et.al., 1966) substitute for Ti with different solubility limits. The change in T_C may be explained in terms of the average ionic radius/electron polarizability of of the dopant ions, and the interaction between these ions and the oxygen and barium ions. Present ferroelectric theories can be divided into three categories: thermodynamic phenomenological theory, microscopic theory and mean field soft mode theory. The thermodynamic theory (for original paper see Devonshire, A.F., 1954; for review paper see Jona, F. and Shirane, G., 1962 and Mitsui, T., et.al., 1976) can explain most of the ferroelectric behavior for BT, but it is not very successful for doped cases. The soft mode theory is highly theoretical and can be very cumbersome (Mitsui, T., et.al., 1976 and Kittel, C., 1976). It is therefore not convenient to use for interpretation of experimental results. The best approach to use here is the microscopic theory first introduced by Devonshire (1949). Considering a perovskite material such as BT, the Ti ion is located in the center of the oxygen octahedron (figure 4.18), Devonshire assumed that due to thermal vibration, Ti might move off-center; a non-linear elastic restoring force applied to the off-center Ti would bring it back to the geometric center position. Upon decreasing temperature, if in a crystal the local field due to polarization increases faster than the restoring force, it would lead to an asymmetric shift in the ionic position, creating permanent polarization. Considering the Lorentz local field correction (Frölich, H., 1986)

$$E_L = E + P/3\epsilon_o \qquad (4.1)$$

where E stands for external field, E_L for Lorentz local field and P for polarization. He reached the polarization catastrophe condition by manipulating the Clausius-Mosotti

Table 4.2 Effect of selected dopants on T_C change in BT

element	$\dfrac{\Delta T_c}{mol.\%}$	solid sol. lim. mol%	references
Zr	- 5.3 °C	100	[1], [2]
Sn	+ 8.0 °C	100	[3], [4]
Hf	- 5.0 °C	100	[5], [6]
Si	+ 6.0 °C	~1	[7]
$Mn_{1/3}Nb_{2/3}$	~ - 20 °C	~1	[8]
$Co_{1/3}Nb_{2/3}$	~ - 25 °C	~1	[8]
$Ni_{1/3}Nb_{2/3}$	- 50 °C	< 2	[8]
$Fe_{1/2}Ta_{1/2}$	- 15 °C	100	[9]
$Zn_{1/3}Nb_{2/3}$	- 16 °C	100	[19]
Nb	- 26 °C	14	[10]
Ta	- 29 °C	14	[10]
Mo	+ ?	--	[11]
W	- 18 °C	0.8	[12]
Mg	- 2 °C	~1	[13]
Ni	- 8 °C	3?	[14]
Co	- 20 °C	> 10	[15]
Fe	- 40~- 75 °C	> 2.5	[14], [16], [17]
Al	+?	<< 5	[13]
$Mn_{1/2}Nb_{1/2}$	- 47 °C	> 3	[18]
$Mn_{1/2}Ta_{1/2}$	- 42 °C	> 3	[18]
$Co_{1/2}Nb_{1/2}$	- 64 °C	> 3	[18]
$Co_{1/2}Ta_{1/2}$	- 61 °C	> 3	[18]
$Ni_{1/2}Nb_{1/2}$	- 64 °C	> 3	[18]
$Co_{1/2}Ta_{1/2}$	- 68 °C	> 3	[18]
Cu	+ 3 °C	3?	[14]
Zn	~0 °C	$\leqq 1$	[19]
Ce	- 28 °C	> 3	[7]
Th	- 6 °C	< 5	[7]

References for table 2.2:

[1] Jonker, G.H., et.al., 1958.

[2] Verbitskaya, T.N., et.al., 1958.

[3] Normura, S., 1955.

[4] Jonker, G.H., et.al., 1955.

[5] Payne, W.H., et.al., 1965.

[6] Fesenko, E.G., 1961.

[7] Marke, G.W., 1955.

[8] Sinaykov, E.V., 1960.

[9] Nakamura, T., 1966.

[10] Subbarao, E.C., et.al., 1959.

[11] baxter, P., 1957.

[12] Ern, V. 1961.

[13] Baxter, P., 1957.

[14] Sakudo, T., 1957.

[15] Kudzin, A.Y., 1962.

[16] Nishioka, A., et.al., 1956.

[17] Ikushima, E.V., et.al., 1965.

[18] Sinyakov, E.V., et.al., 1960.

[19] Peng, P., present work.

equation (Frolich, H., 1986)

$$\epsilon_r = 1 + \frac{\frac{1}{\epsilon_o}(\Sigma\alpha_e/V + \alpha_i/V)}{1 - \frac{1}{3\epsilon_o}(\Sigma\alpha_e/V + \alpha_i/V)} \qquad (4.2)$$

where α_i is the ionic polarizability of Ti, V is the unit cell volume and α_e stands for the electronic polarizability of the Ba^{+2}, Ti^{+4} and O^{-2}. When the following equation holds,

$$1 = \frac{1}{3\epsilon_o}(\Sigma\alpha_e/V + \alpha_i/V) \qquad (4.3)$$

it leads to the polarization catastrophe and the Curie point is defined. By substituting the numeric data for BT into equation (4.3), Devonshire calculated the contribution to this catastrophe from Ti ionic polarizability to be 39%. Slater (1950) further considered the structural characteristics of BT, and recalculated the crystal local field based on the interaction between Ti^{+4} and O^{-2}. He found that the local field correction was much higher than the regular Lorentz local field correction. When the Ti^{+4} ion moves off-center, it causes to the surrounding O^{-2} ions to be polarized, and polarized O^{-2} ions can exert a back effect on the Ti^{+4} ion. This then gradually establishes a chain ionic polarization, therefore resulting in spontaneous polarization below T_c. In this case, the contribution of the Ti^{+4} ion to spontaneous polarization is only 1/6 of that with only Lorentz correction $(P/3\epsilon_o)$ without considering the electronic polarization chain reaction. Generally speaking, from a quantitative point of view, the contribution of polarization for ferroelectric behavior is 37% from Ti^{+4} (31% from ionic displacement, and 6% from electronic polarization); 69% from O_I^{-2} (see figure 4.18), 6% from O_{II}^{-2} and O_{III}^{-2}; and 2% from Ba^{+2}. Based on this argument, α_e versus r (ionic radius of B cation) is plotted in figure 4.19. The ionic radii are taken from Shannon and Prewitt (1969) with a six-fold coordination. For some transition metal ions, ionic radii are chosen based on the following argument. It is common practice that the crystal field stabilization energy in the oxygen octahedron is smaller than the electron pairing energy (see Table 4.3). The transition metal ions should be usually in their high spin state in the perovskite lattice (Burn, R.G., 1970). However, when the transition metal ions with

different radius are incorporated as acceptors into the octahedral position, there are two possible consequences. First, the lattice distortion will result in a large local electrical field. Second, oxygen vacancies generated by acceptor doping will prefer to locate near the dopant ions. This may lead to a reduction in the coordination number of the transition metal ions in the oxygen octahedra. As a result, the crystal field splitting energy will increase. All of these factors may cause a switch of spin state of these doped ions from high to low. Hence the low spin state ionic radii for some transition metal ions are used in the discussion. Now we are in a position to discuss figure 4.19. From table 4.2, comparing the change in T_c and the location of dopant ions in figure 4.21, it is clear that a doped metal ion with an ionic radius closer to that for the Ti^{+4} ion and with a higher α_e than Ti^{+4} ion will result in a larger Curie temperature shift in doped BT. This phenomenon may be understood as follows: (1) This discussion is only valid for fixed A site perovskite structure, and dopant ions only occupy B sites. Therefore the key points are the electronic polarizability α_e, ionic radius of the dopant ions and the interaction between the oxygen, A-site cation and dopant ions. (2) If a dopant ion has a similar ionic radius to the Ti^{+4} and a larger α_e than the Ti^{+4} ion, the local electric field inside the oxygen octahedron will be influenced to a large extent. The off-center behavior of the cation located in this position is also going to change, thus affecting T_c to a large extent. (3) If the ionic radius mismatch is too large, the effect on T_c will be small. For the dopant ions with a small α_e, the influence can be negligible. Comparing with the experimental data published in the open literature, these qualitative predictions appears to work satisfactorily.

The transition peak broadening can be understood from the following: (1) Three transition temperatures (i.e. from cubic to tetragonal, tetragonal to orthorhombic, orthorhombic to rhombohedral) coalesce which has been observed in the BT-BZ ($BaZrO_3$) system with a high temperature XRD study (Hennings, D., et.al., 1982). (2) A small grain with single ferroelectric domain microstructure can not compensate the large internal stress generated by the paraelectric to ferroelectric transition (Buessem, W.R., et.al., 1966; Pohanka, R.C., et.al., 1976; Arlt, G., et.al., 1985). The transition peak therefore broadens. (3) Chemical inhomogeneity in the material results in local microdomains with different transition temperatures which leads to a relaxor dielectrics with DPT (cross, L.E., 1987). In our case, the grain size is varied from $0.5\mu m$ to $100\mu m$ (see table 4.1). For high x values, the grain size is not small enough to satisfy reason (2), therefore this point is ruled out. Due to experimental limitations, up to this point,
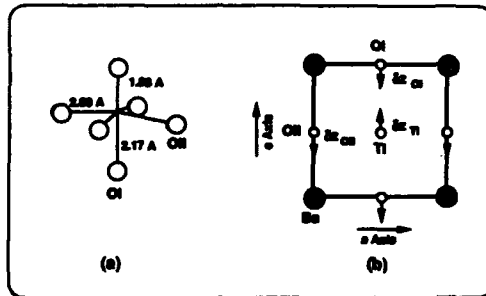
Figure 4.18 Atom arrangement of BT in ferroelectric tetragonal phase.
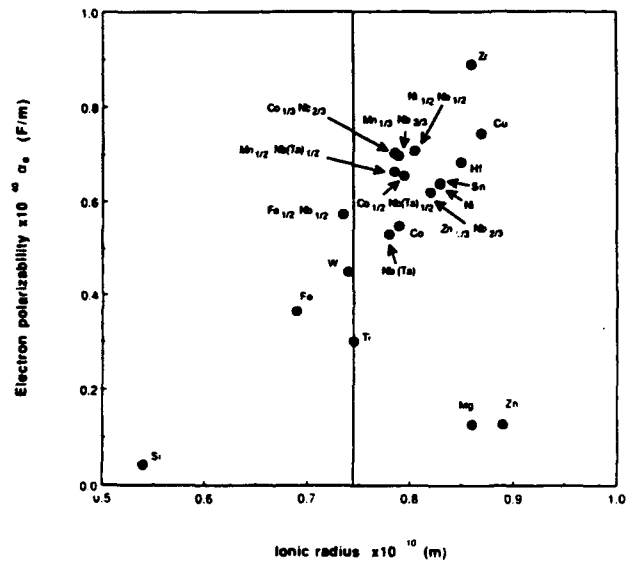
Figure 4.19 A plot of electron polarizability against ionic radius of selected cations.

101

ions	P ($\frac{1}{cm}$)	Δ ($\frac{1}{cm}$)
Mn^{+2}	25,500	7,800
Fe^{+2}	15,000	10,400
Co^{+2}	22,500	9,700
Ni^{+2}	--- ---	8,500
Cu^{+2}	--- ---	12,600
Ti^{+3}	--- ---	18,300
V^{+3}	--- ---	16,700
Cr^{+3}	--- ---	17,400
Mn^{+3}	28,000	18,900
Fe^{+3}	30,000	13,700

Data come from Dunitz, J.D., et.al., (1957) and He, F.C., (1979).

Table 4.3   Comparison of crystal field stabilization energy Δ and electron pairing energy P of selected transition metal ions in octahedral field.

we can only assume that the three phase co-existence near the Curie temperature and composition fluctuation may be the reasons for this behavior.

4.2) *Defect Structure of BZN*

4.2.1) Definition and Composition Design

To study the defect structure of a complex compound, it is necessary to first define the stoichiometric and nonstoichiometric compositions properly. The principles discussed in chapter 1 are applied here. Stoichiometric BZN is defined as $Ba(Zn_{1/3}Nb_{2/3})O_3$. Any compositional deviation away from this standard stoichiometric point is termed nonstoichiometry. For example, $Ba(Zn_{1/3}Nb_{2/3})_{1-x}M_xO_3$ can be considered as nonstoichiometric composition if $x \neq 0$. Table 3.1 used in chapter 3 lists the major compositions for the defect structure study. The purpose of this section is to discuss the results of the defect structure for stoichiometric BZN and compensation defects for various doping cases.

4.2.2) Stoichiometric BZN

High temperature equilibrium conductivity of stoichiometric BZN at 3 isotherms over a wide range of oxygen partial pressure is shown in figure 4.17. It is apparent that the experimental results are characterized by an oxygen deficient n-type region with the conductivity increasing with decreasing P_{O_2}; and an oxygen excess, p-type region with the conductivity increasing with increasing P_{O_2}; separated by a conductivity minimum at a P_{O_2} which is designated as the stoichiometric point assuming $\mu_e = \mu_h$. At higher temperatures and lower P_{O_2} ranges, the n-type conductivity curve tends to switch from a slope of $-\frac{1}{4}$ to $-\frac{1}{6}$. This slope change occurs when the electron concentration equals to the net acceptor level. With decreasing temperature, the minimum shifts to lower P_{O_2} due to the difference between the enthalpy of reduction and oxidation. However, compared with BT, the relative conductivity level is about 2 orders of magnitude lower, the minimum shift is not as large, and the intrinsic acceptor concentration seems to be quite high. Except for these facts and in spite of the detailed electrical transport properties which will be discussed later in this chapter, the defect structure of BZN seems to be very similar to that of the parent phase BT.

4.2.3) Acceptor Doped BZN

4.2.3.1) Zn Rich BZN (BZNZ)

As shown below, within the solubility limit, Zn incorporates into the Nb site as

an acceptor, Zn_{Nb}'''.

$$ZnO + BaO \rightarrow Ba_{Ba} + \tfrac{1}{3} Zn_{Zn} + \tfrac{2}{3} Zn_{Nb}''' + 2\,O_o + V_o^{\cdot\cdot} \qquad (4.4)$$
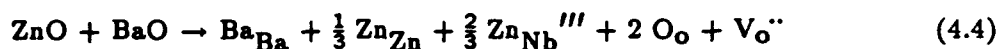
From high temperature equilibrium conductivity, this hypothesis is confirmed. Figure 4.18 shows the comparison between stoichiometric BZN and acceptor doped Zn rich BZN. The characteristic of acceptor doping indicates that Zn occupying the Nb site does behave as an acceptor in the crystal, and that the charge compensation species is the oxygen vacancy. The solubility limit for excess Zn on the B site is around 1%. Above that, excess Zn is expelled out to form a second phase, ZnO. Figure 3.6 shows a BSE micrograph and Zn X—ray map image of the 3% Zn rich composition. ZnO is clearly observed.

4.2.3.2) K Doped BZN (BKZN and BKZN')

The purpose to study K doped BZN is twofold. First, the ordering model for 1:1 type needs to be clarified which has been discussed in detail in chapter 3. Second, a study of A site acceptor doping in BZN is a necessity since (1) samples BZNZ only involve B site acceptor doping; (2) ordering behavior may drastically affect the defect compensation mechanism due to a complex structure. For example, as discussed in chapter 3, La doped into the A site resulted in the B site ratio self-adjustment by expelling a second phase instead of the generation of metal vacancies.

The two possibilities for K incorporation into the crystal lattice can be expressed as follows:

(A) $\tfrac{1}{2} K_2O + \tfrac{1}{3} ZnO + \tfrac{1}{3} Nb_2O_5 \rightarrow$

$\qquad K_{Ba}' + \tfrac{1}{3} Zn_{Zn} + \tfrac{2}{3} Nb_{Nb} + 2\tfrac{1}{2} O_o + \tfrac{1}{2} V_o^{\cdot\cdot}$ (BKZN) $\qquad (4.5)$

(B) $\tfrac{1}{2} K_2O + \tfrac{1}{2} Nb_2O_5 \rightarrow$

$\qquad K_{Ba}' + \tfrac{1}{3} Nb_{Zn}^{\cdot\cdot\cdot} + \tfrac{2}{3} Nb_{Nb} + 3 O_o$ (BKZN') $\qquad (4.6)$
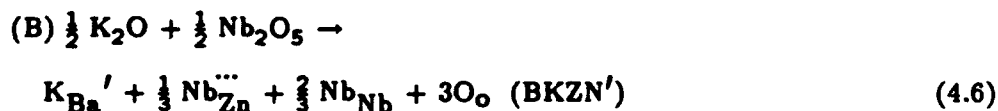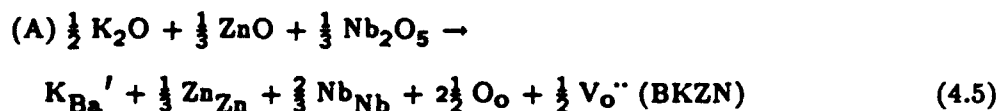
The first possibility would lead to oxygen vacancy compensation, and the second one may result in self-charge compensation and affect the complex ordering. The TEM study (Figure 3.4) indicated that the first possibility is correct. Additional evidence

gathered using EPMA is shown in figure 4.20. The small grained single phase microstructure for case (A) and large grained dense microstructure due to the existence of a low melting second phase for case (B) clearly supports case (A).

$$Ba_{1-x}K_x(Zn_{\frac{1-x}{3}}Nb_{\frac{2+x}{3}})O_3 \rightarrow Ba_{1-2x}K_x(Zn_{\frac{1-x}{3}}Nb_{\frac{2-2x}{3}})O_{3-3x} + x(BaNbO) \quad (4.6)'$$

$$BKZN' \qquad \rightarrow \qquad BKZN \qquad\qquad + \quad \text{second phase}$$
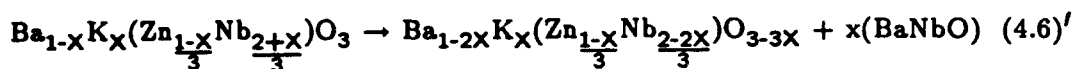
High temperature equilibrium conductivity of BKZN and BKZN' cannot be obtained with a reasonable reproducibility due to the volatility of potassium. However, the typical acceptor behavior could still be observed for these samples. It is therefore concluded that the compensation defect for K doped BZN is oxygen vacancies.

4.2.4) Donor Doped BZN

4.2.4.1) Nb Rich BZN (BZNN)

The high temperature equilibrium conductivity of BZNN ($Ba(Zn_{1/3}Nb_{2/3})_{1-x}Nb_xO_3$) with $x=0.01$ is shown in Figure 4.18, showing a typical heavily donor doped behavior. Since doped samples still maintain light yellow color and low conductivity, the compensation defect species cannot be electronic. The possible metal vacancy compensation defects are either V_{Zn}'' or V_{Nb}''''' or V_{Ba}''. In order to determine the correct compensating defect, a series of samples were designed as follows:

Sample composition	Concentration	Proposed defect	
A) $Ba(Zn_{1/3}Nb_{2/3})_{1-x}Nb_xO_3$	$x = 0.01$	compensation ?	(4.7)
B) $Ba_{1-\frac{x}{2}}(Zn_{1/3}Nb_{2/3})_{1-x}Nb_xO_3$	$x = 0.01$	V_{Ba}'' ?	(4.8)
C) $Ba(Zn_{\frac{1}{3}-\frac{x}{2(1-x)}}Nb_{2/3})_{1-x}Nb_xO_3$	$x = 0.01$	V_{Zn}'' ?	(4.9)

The basic principle is to check if there is a single phase formation for proper compensation defects design. The BSE images of these samples obtained from EPMA are shown in figure 4.21. Comparing the microstructures in the cases A, B and C, there are three points to be addressed. (1) Case B achieves the highest density and largest

Figure 4.20 BSE images of (A) $Ba_{0.9}K_{0.1}(Zn_{0.333}Nb_{0.667})O_3$ and (B) $Ba_{0.9}K_{0.1}(Zn_{0.3}Nb_{0.7})O_3$, showing a relative denser, larger grained microstructure with Nb rich second phase in case (B).

Figure 4.21 BSE images of (A) $Ba(Zn_{1/3}Nb_{2/3})_{1-x}Nb_XO_3$, (B) $Ba_{1-x\frac{x}{2}}(Zn_{1/3}Nb_{2/3})_{1-x}Nb_XO_3$, and (C) $Ba(Zn_{\frac{1}{3}-\frac{x}{2(1-x)}}Nb_{2/3})_{1-x}Nb_XO_3$ with x=0.01, showing the different grain size, density and

amount of second phase in three cases.

grain size with greatest amount of second phase. (2) Case A and C are almost identical except for less second phase in case C. (3) The second phase appears brighter in the BSE images compared with the matrix phase, indicating that the second phase has a higher average molecular weight than that of the matrix phase. A tentative composition (case A) was first made up to test if there is a metal vacancy compensation mechanism. Two possible metal vacancy compensation mechanisms were checked by designing case B and C. In figure 4.21 (B), a large amount of light color second phase in BSE image rules out the possibility of barium vacancy compensation because the vacant barium site has already been left out. However, it can not be due to the zinc vacancies either because this can only cause a second phase which appears darker in the BSE image. In case C, the sample with deliberately vacated zinc sites results in an almost single phase material which is somewhat of a contradiction to case B.

In order to solve this problem, a zinc/niobium vacancy model is proposed. Considering three cases, if V_{Zn}'' and V_{Nb}''''' with a ratio close to 1:2 act as charge compensation species for Nb rich donor doping, we would expect three effects caused by these vacancies. (1) the existence of these vacancies would destroy acceptor doped 1:1 type ordered microdomains and therefore destroy 1:1 type ordering. (2) V_{Zn}'' and V_{Nb}''''' with a ratio close to 1:2 might also enhance the B site ordering in the 1:2 ordering scheme. (3) ordering of these vacancies would result in a defect structure change. Experimentally, we observed (a) a mixture of two types of ordering in stoichiometric BZN which is associated with some degree of Zn loss; (b) an ordering scheme change favoring 1:2 type ordering upon Nb rich in BZN (chapter 3). Those results are in agreement with this model. For defect structure change in terms of cation vacancy concentration, we will discuss this in detail in the second part of this chapter. It seems that whenever there are vacant zinc sites, niobium would occupy them to form the donor centers; in the mean time, the system adjusts the amount of V_{Zn}'' and V_{Nb}''''' with a ratio close to 1:2 to compensate for $Nb_{Zn}^{...}$. As a consequence, 1:2 type ordering is promoted. However, why this system prefers high charge V_{Nb}''''' over lower charge V_{Ba}'' is still not clear at the moment. In addition, there is no direct evidence of ordered B site cation vacancies ordering or 1:2 ratio of these vacancies to support this model. Further experiments are required to clarify these problems. Nevertheless, it is clear that we have to look into the structural aspects in order to understand this peculiar phenomenon. The solubility limit for extra Nb incorporated into the lattice is estimated at about 9% based on TEM and EPMA analysis.

4.2.4.2) La Doped BZN

La doped BZN prefers the Zn/Nb ratio self-adjustment to compensate for the charge generated by La occupying the Ba site as a donor (chapter 3). BSE images for the following three cases are shown in figure 4.22.

Sample composition	Concentration	Proposed defect/Result	
A) $Ba_{1-x}La_x(Zn_{1/3}Nb_{2/3})O_3$	x = 0.01	? second phase	(4.10)
B) $Ba_{1-\frac{3x}{2}}La_x(Zn_{1/3}Nb_{2/3})O_3$	x = 0.01	V_{Ba}'' ? second phase	(4.11)
C) $Ba_{1-x}La_x(Zn_{\frac{1+x}{3}}Nb_{\frac{2-x}{3}})O_3$	x = 0.01	Zn/Nb ratio? single phase	(4.12)

The same design principle as in the section 4.2.4.1 applies here. The light colored second phase and dense large grained microstructure in case (A) and (B) clearly indicate that the compensating defects are not metal vacancies. Case (C) yields a single phase, small grained microstructure which implies that the Zn/Nb ratio self-adjustment is the charge compensation mechanism. The ordering behavior in all three cases is another clue to the defect charge compensation mechanism. Since the system has a preference for the Zn/Nb ratio self-adjustment, the following happens: (1) extra Nb is expelled out of the system to form a Nb rich second phase which appears brighter in the BSE image; (2) the charge imbalance in the 1:1 type ordered domains gets reduced and ordering is enhanced no matter whether the Zn/Nb ratio is preadjusted or not. In the case that the Zn/Nb ratio was not pre-adjusted in the starting composition, the system adjusts itself and ends up with the same ordering pattern and ejects a Nb rich second phase (Figure 3.3).

The high temperature equilibrium conductivity of stoichiometric BZN and BLZN with x = 0.05 and 0.10 at 1200°C are plotted in figure 4.23. The same conductivity curve is obtained for all three samples within the experimental error, clearly indicating that there is no charge imbalance generated in the system, and that the Zn/Nb ratio self-adjustment results in a self-compensated compound. The solubility of La substituting for Ba in BZN is about 10% as determined with TEM and EPMA analysis.

4.2.5) Brief Summary

Table 4.4 summarizes the results discussed in this section. The solubility limit

for K doped BZN could not be estimated due to volatility of the K ion. In this case, only a general trend for the defect compensation mechanism can be predicted.

As a comparison, compensation species for BT, the parent system of BZN are also listed in table 4.5. As can be seen in table 4.5, the ordering behavior in the complex case does change the defect structure. Other than that, the defect structures are quite similar for both cases.

Figure 4.22 BSE images of (A) $Ba_{1-x}La_x(Zn_{1/3}Nb_{2/3})O_3$, (B) $Ba_{1-\frac{3x}{2}}La_x(Zn_{1/3}Nb_{2/3})O_3$, and (C) $Ba_{1-x}La_x(Zn_{1+\frac{x}{3}}Nb_{\frac{2-x}{3}})O_3$ with x=0.01.
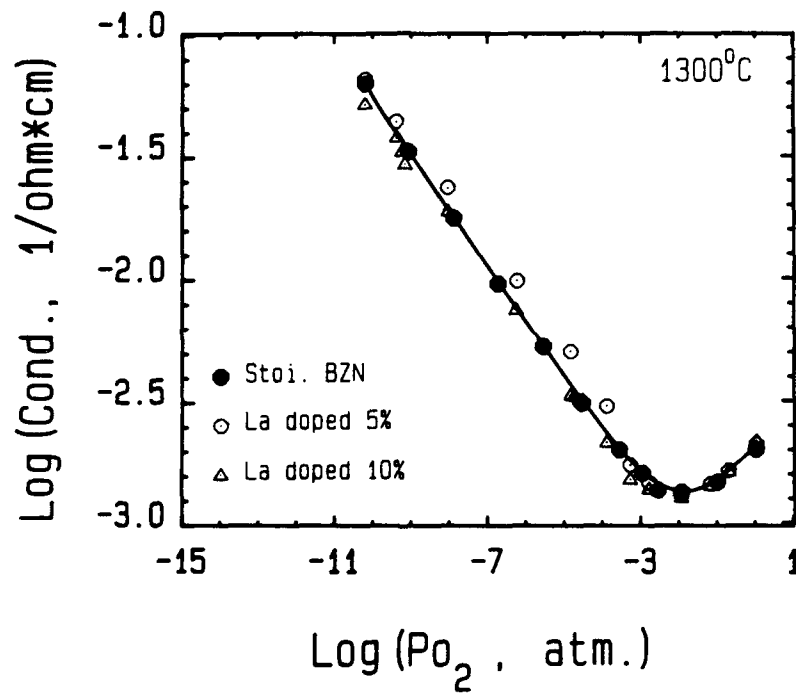
Figure 4.23 High temperature equilibrium conductivity as a function of P_{O_2} for stoichiometric BZN and La doped BZN ($Ba_{1-x}La_x(Zn_{\frac{1+x}{3}}Nb_{\frac{2-x}{3}})O_3$, with x=0.05 and 0.10) at 1200°C, showing essentially the same conductivity profile.

• acceptor doped on A site (K_{Ba}'):	$V_O^{..}$	solubility limit:?
• acceptor doped on B site (Zn_{Nb}'''):	$V_O^{..}$	solubility limit: ~1%
• donor doped on A site ($La_{Ba}^{.}$):	Zn/Nb ratio self-adjustment	solubility limit: ~10%
• donor doped on B site ($Nb_{Zn}^{...}$):	V_{Zn}'' & V_{Nb}'''''	solubility limit: ~9%

Table 4.4 Defect compensation species in doped BZN

Descriptions	BT	BZN
• acceptor doped on A site:	$V_O^{..}$ (K, ?)	$V_O^{..}$ (K, ?)
• acceptor doped on B site:	$V_O^{..}$ (Zn, 1%)	$V_O^{..}$(Zn, 1%)
• donor doped on A site:	V_{Ba}'' (La, 20%)*	Zn/Nb ratio self-adjustment (La, 10%)
• donor doped in B site:	V_{Ti}'''' (Nb, 12%)#	V_{Zn}'' & V_{Nb}'''''(Nb, 9%)

* Daniels, J., et.al., 1976.

Chan, H.M., et.al., 1985; Sabbarao, E.C., et.al., 1959.

Table 4.5 Comparison between defect compensation species in doped BZN and BT

113

Chapter 5 <u>ELECTRICAL</u> <u>TRANSPORT</u> <u>PROPERTIES</u> of <u>BZN</u>

Electrical transport mechanism of stoichiometric BZN will be discussed in this chapter. High temperature studies will be presented first, followed by low temperature measurement results.

5.1) *Hopping Conduction of Electrons and Holes*

5.1.1) High Temperature Equilibrium σ_{DC} and α

High temperature equilibrium DC conductivity of stoichiometric BZN at 3 isotherms over wide oxygen partial pressure range is shown in figure 4.15. Figure 5.1 shows the corresponding Seebeck coefficient measured under the same condition. A clear $-2.303k/4e$ slope at low oxygen partial pressure implies that the system either belongs to the band type or large polaron type of conductor or possesses the small polaron conduction with charge carrier mobility independent of carrier concentration.

In order to clarify the transport mechanism, the electronic conduction contribution must be determined. It is well known that the total conductivity σ_t is

$$\sigma_t = \sigma_i + \sigma_e + \sigma_h \qquad (5.1)$$

where i, e and h stand for ionic, electronic and hole conductivity, respectively. At reduced atmosphere within the certain Po_2 range, σ_h is negligible and σ_e is proportional to $Po_2^{-1/4}$ (chapter 2). We also assume that σ_i is independent of oxygen partial pressure which is reasonable at $-\frac{1}{4}$ region (in terms of constant concentration of ionic defect). The total conductivity can then be expressed as (Mehta, A., et.al.; 1989)

$$\sigma_t(T, Po_2) \cong \sigma_i(T) + \sigma_e^0(T) Po_2^{-1/4} \qquad (5.2)$$

Figure 5.2 shows the result of plotting σ_t against $Po_2^{-1/4}$ at constant temperature for n type conduction. The intercept is the ionic conductivity. Apparently, σ_i is essentially very small and can be neglected. Therefore the conduction is mainly of electronic nature.

The temperature dependence of DC conductivity and Seebeck coefficient at two

114
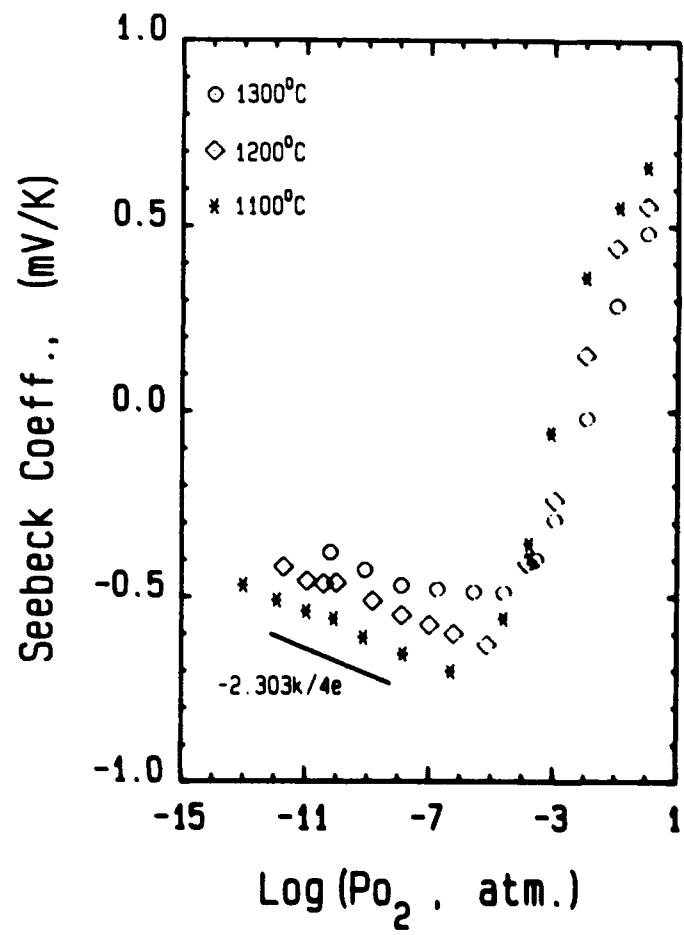
Figure 5.1 Three isotherms of Seebeck coefficient as a function of Po_2 for stoichiometric BZN.
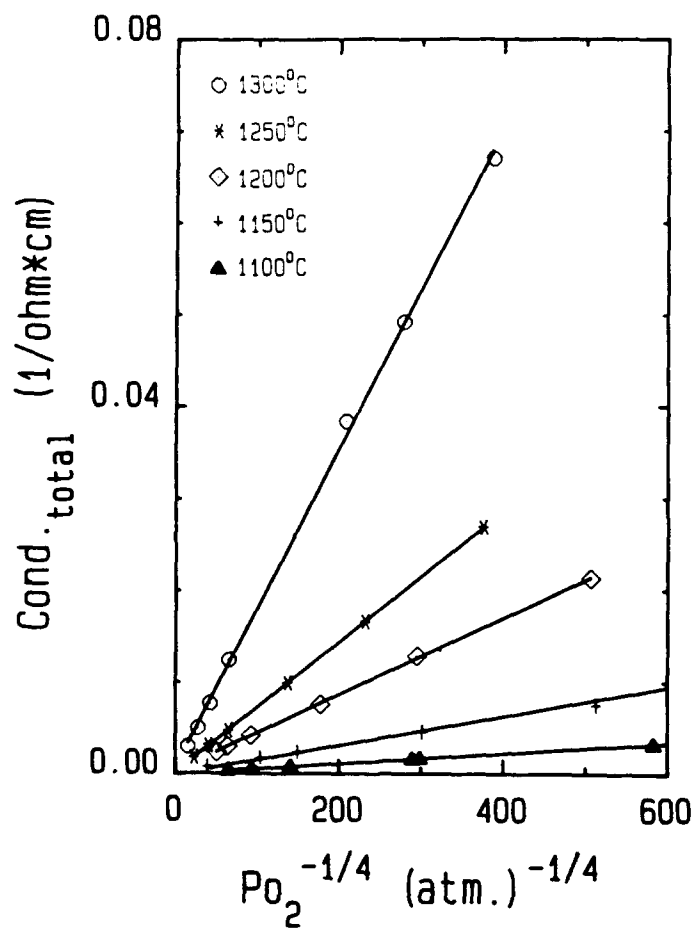
Figure 5.2 Total conductivity vs $Po_2^{-1/4}$ for stoichiometric BZN at n-type region for 5 isotherms. The intercepts, the ionic conductivity are as follows: $1.7*10^{-4}$ for 1300°C; $1.5*10^{-4}$ for 1250°C; $1.4*10^{-4}$ for 1200°C; $2.9*10^{-5}$ for 1150°C and $2.0*10^{-5}$ for 1100°C.

116

different oxygen partial pressures were measured, as shown in figure 5.3. As we discussed in the background section, conductivity can be written as Equation (1.19). Depending upon the charge carrier transport mechanism, the expression for n and μ can be different. In order to derive the energies of formation and motion for a charge carrier, we analyze those data by assuming either band type or small polaron conduction mechanism for both electron and holes. For band type conduction, equations (1.27), (1.28) are used for calculation. m^* is chosen as m^o as a first approximation. There are two types of small polaron: adiabatic and non-adiabatic (Adler, D., 1974; Bossman, A.J., 1970). Since we did not measure the Hall coefficient, it is impossible to distinguish between these two cases at present (Nagels, P., 1980). We choose the non-adiabatic small polaron model to calculate the transport parameters. The reasons will become clear after we get into the next section on AC conductivity and dielectric relaxation studies. The mobility of charge carriers for small polarons for adiabatic and non-adiabatic cases are (Nagels, P., 1980)

$$\mu_{adiabatic} = \frac{\mu_o{}^a}{T^{1/2}} \exp(- \Delta H_m{}^a/kT) \tag{5.3}$$

$$\mu_{non\text{-}adiabatic} = \frac{\mu_o{}^{na}}{T^{3/2}} \exp(- \Delta H_m{}^{na}/kT) \tag{5.4}$$

Taking equation (1.22) and proper A and n_o values for different conduction mechanisms into consideration, the electron and hole concentrations n and p and mobilities μ_e and μ_h can be calculated. The results for 1000°C are listed in table 5.1. It is obvious that the band model does not hold here because of the rather small mobility value ($\sim 10^{-3} \sim 4$ cm^2/Vsec.. A rough critical number of the charge carrier mobility for distinguishing between the band and the small polaron type conduction is about $0.1 \sim 1$ cm^2/Vsec.). Again based on the discussion in chapter 1, $\sigma \propto Po_2{}^{\pm 1/4}$. If we also consider non-adiabatic small polaron temperature dependence of pre-exponential term, the concentration of electrons or holes is

$$n(or\ p) = C\ Po_2{}^{\pm 1/4} \exp(- \Delta H^f{}_{O\ or\ R}/kT) \tag{5.5}$$

$$\sigma_{e\ or\ h} \propto \frac{1}{T^{3/2}} Po_2{}^{\pm 1/4} \exp\{-(\Delta H^f{}_{O\ or\ R} + \Delta H_m{}^{h\ or\ e})/kT\} \tag{5.6}$$

117
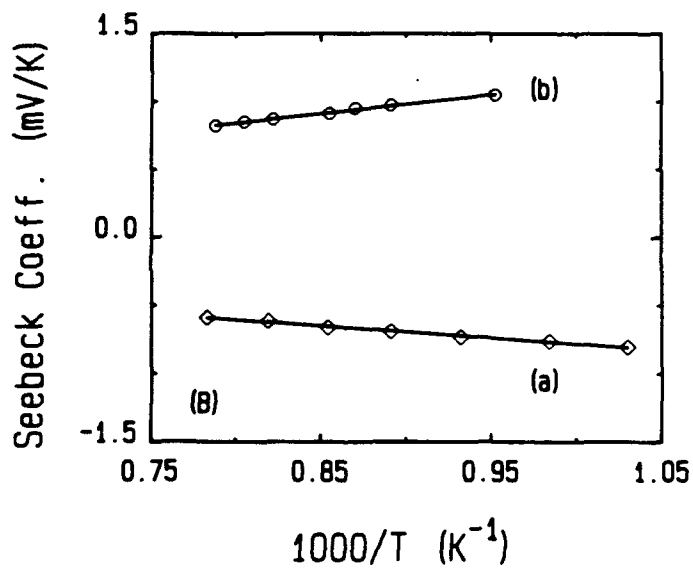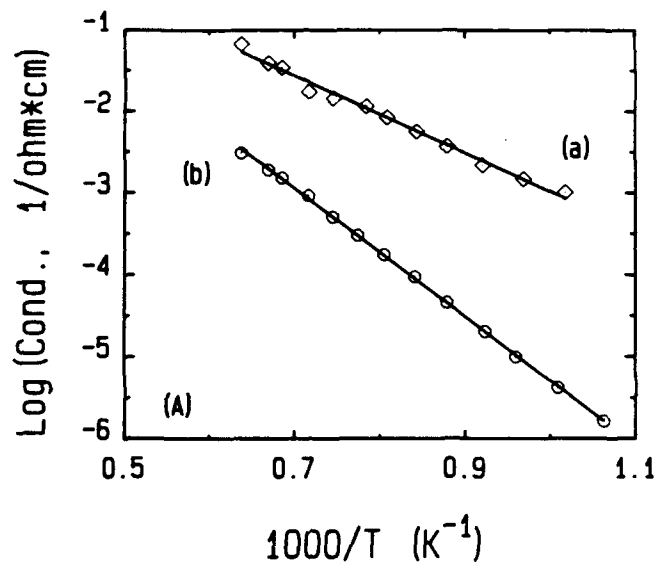
Figure 5.3 Arrhenius plot of high temperature equilibrium conductivity (A) and Seebeck coefficient (B) of stoichiometric BZN at (a) $V_{CO_2/CO}=0.471$ and (b) O_2.

T = 1000°C

Log(P_{O_2}) (atm.)	Log(σ) (s/cm)	α * (mV/°K)	model	Log n or p (1/cm³)	μ_e or μ_h ! (cm²/Vsec.)	Log N (1/cm³)	A
- 12.41	- 2.510	- 0.591	sp*	19.31	9.45×10^{-4}	22.29	0
			band+	19.37	8.24×10^{-4}	20.35	2
0.00	- 3.526	+ 0.820	sp	18.81	2.88×10^{-4}	22.94	0
			band	18.22	1.12×10^{-3}	20.35	2

* Sp stands for small polaron model. Here $N_c = N_{Nb}^{5+}$ and $N_v = N_O^{2-}$.

+ band stands for band type model. Here $N = 2(2\pi m^* kT/h^2)^{3/2}$,

m_e^* or $m_h^* = m_e^v$.

$|\alpha| = \dfrac{k}{e}$ (Ln[$\dfrac{N}{n \text{ or } p}$] + A). ! $\sigma = e\mu_c n + e\mu_h p$.

Table 5.1 Calculation of transport parameters of stoichiometric BZN.

119

where C is a temperature independent constant. + and O stand for hole case, − and R for electron case. This type of concentration relationship comes from equations (1.6) through (1.19) (see chapter 1). The conductivity therefore follows the relation where e is designated for electron and h for hole. Plotting $Log(\sigma T^{3/2}Po_2^{\pm 1/4})$ and $Log(n \text{ or } pPo_2^{\pm 1/4})$ as a function of $1/T$, we can get both energy for formation and motion. Figure 5.4 shows this calculation results for both n and p type conduction under two oxygen partial pressures. Using linear regression, concentrations and mobilities for electrons and holes can be determined as

$$n = 2.75*10^{25}Po_2^{-1/4}\exp\{- 2.33(eV)/kT\} \quad (cm^3) \qquad (5.7)$$

$$p = 1.70*10^{24}Po_2^{+1/4}\exp\{- 1.37(eV)/kT\} \quad (cm^3) \qquad (5.8)$$

$$\mu_e = \frac{871}{T^{3/2}}\exp\{- 0.33(eV)/kT\} \quad (cm^2/Vsec.) \qquad (5.9)$$

$$\mu_h = \frac{240}{T^{3/2}}\exp\{- 0.34(eV)/kT\} \quad (cm^2/Vsec.) \qquad (5.10)$$

The origin of small polaron for electrons is relatively straight forward. Each oxygen lost by reduction generates an oxygen vacancy and two electrons. These electrons may be bound to Nb^{+5} ($Nb^{+5} + e \rightarrow Nb^{+4}$) and form Nb^{+4}. This bound electron (Nb^{+4}) along with its lattice distortion forms the small polaron. On the other hand, for the case of oxidation, the origin of small polaron for holes is not so clear as that for electrons. According to the band structure estimation (Deleo, G., 1990; Harrison, W.A., 1980), the conduction band for stoichiometric BZN is believed to be Nb^{+5} $4d^0$ band and the valence band may be the O^{-2} $2p^6$ or the Zn^{+2} $3d^{10}$ band. Upon oxidation, filling an oxygen vacancy results in the formation of holes. These holes can be either bound to $Zn^{+2}(3d^{10}) + h \rightarrow Zn^{+3}(3d^9)$ or to $O^{-2}(2p^6) + h \rightarrow O^{-1}(2p^5)$ and drift under the external electric field via hopping conduction mechanism. At present, we could not differentiate between these possibilities. But the small polaron nature and p-type semiconduction imply that there must be a hole bound center of some sort. Hughes (Hughes, R.C., 1977) and Fowler et.al. (Edwards, A.H., Fowler, W.B., 1982) claimed that holes in amorphous SiO_2 are hopping through O^{-1} which means that this species is not impossible.

Until now it has been assumed that the mobilities are charge carrier concentration independent. As mentioned earlier, a -2.303k/4e slope in the n-type
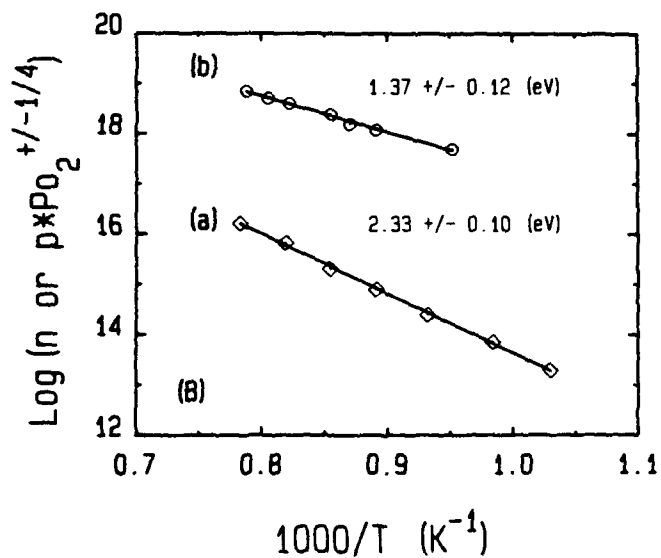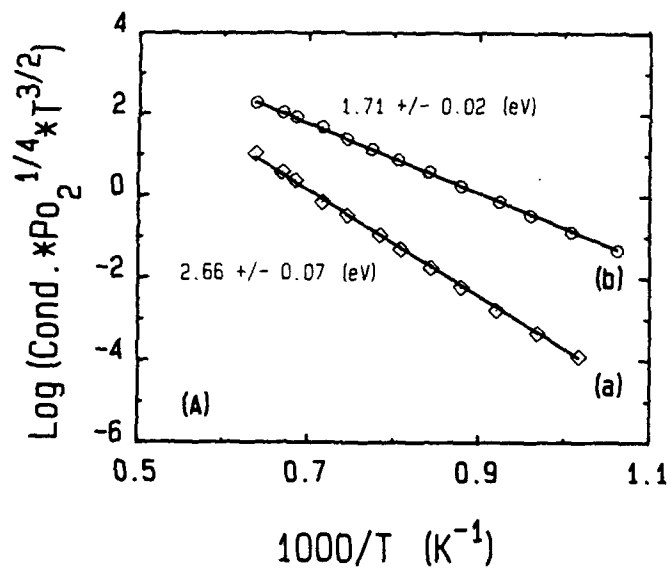
Figure 5.4 (A) $Log(\sigma T^{3/2} Po_2^{\pm\frac{1}{4}}, \dfrac{K^{3/2} atm.^{\pm\frac{1}{4}}}{ohm\ cm})$ and (B) $Log(nPo_2^{\pm\frac{1}{4}}, \dfrac{atm.^{\pm\frac{1}{4}}}{cm^3})$ vs 1000/T for stoichiometric BZN at (a) $V_{CO_2/CO}=0.471$ and (b) O_2. The energies in the plot correspond to the total (A) and formation (B) enthalpies for both cases.

region of the Seebeck coefficient against $Log(Po_2)$ at constant temperature could test this assumption. Here we will use Jonker's analysis to supply more proof. This analysis was first introduced by Jonker (Jonker, G.H., 1968) for a band type semiconductor with two types of charge carriers in a non-degenerate state. Later, others (Su, M.Y. et.al., 1990) used this method on small polaron case and were somewhat successful. The beauty of this analysis is that by plotting α versus $Log(\sigma)$, a "pear" shaped curve, usually referred to as a "Jonker pear", can be used to calculate several important transport parameters, such as mobility, density of states and band gap etc.. A peculiar feature of this "pear" is that it only depends on intrinsic parameters. Thus the validity of a simultaneous measurement of σ and α can be checked by their fit to the appropriate Jonker Pear. This fit is independent of doping, departure from stoichiometry, and other details of defect structure. However, this analysis cannot be used for any case where the charge carrier mobility is concentration dependent. The concentration dependent mobility is sometimes true for small polaron. The Jonker analysis will not be reviewed here, since we do not have to draw a conclusion for transport mechanisms based on that analysis and the -2.303k/4e slope in α versus $Log(Po_2)$ plot at n type region has already indicated the validity of the fundamental assumption. All we want to do here is to demonstrate a modified Jonker analysis for a single charge carrier and supply a more solid foundation for the analysis in this chapter.

As shown in equation (1.30) for single type charge carriers, in the small polaron case, $n_o \rightarrow n_o(e) = n_o(Nb^{+5})$, and $n_o(h) = n_o(O^{-2})$; $A=0$. Combining equations (1.30), (1.22) and taking the electron case as an example, α has the form

$$-\frac{k}{2.303e}\alpha = \log(\sigma) - \frac{k}{2.303e}\{\log[n_o(e)] + A\} - \log(\mu_e) - \log(e) \qquad (5.11)$$

If mobility is independent of concentration, we can get

$$\alpha \propto -\frac{2.303k}{e}\log(\sigma) \qquad (5.12)$$

Plotting α versus $\log(\sigma)$, a straight line with a slope of $2.303k/e=0.198$ is expected. The same principle applies to the hole case. By simultaneously measuring σ and α at two oxygen partial pressures for both n and p type charge carriers, which is essentially part of the two wings of the "Jonker pear", the experimental results are in an excellent

122

agreement with the theoretical prediction (figure 5.5). The analysis here therefore indicates that our discussion in this section is on a solid ground.

5.1.2) AC Conductivity, Dielectric Relaxation and Impedance Analysis

Additional experiments to support the transport mechanism in our system will be discussed in this section. AC conductivity, dielectric relaxation and complex plane impedance analysis were performed at relatively low temperature to provide additional support to the charge carrier transport mechanism discussed above. Measured samples were:

(a) Samples cooled under equilibrium condition from 1300°C at $V_{CO_2/CO}$= 0.471 ($Po_2(1300°C) = 3.98*10^{-11}$ atm.) to 500°C and then quenched to room temperature.

(b) Samples quenched to room temperature, after equilibrated at $V_{CO_2/CO}$=0.471, 1300°C.

(c) Samples quenched to room temperature, after equilibrated at O_2, 1300°C.

The measurements were carried out under the following conditions:

(1) Frequency range: 10 to 10^6 Hz; Temperature range: -150 to 500°C.

(2) Three probe with guard ring electrode design (figure 5.6) was used to eliminate surface conduction. Ag paste or Au evaporated electrodes, and the Au electrode with different sample thickness were also used to test for possible electrode polarization.

(3) Directly measured parameters were either Y/θ or C/G depending on either HP4274A, and HP4194A or GR 1616 measuring instrument. Where Y is complex admittance and θ is phase angle; C is capacitance and G is conductance.

AC conductivity frequency spectra for samples (a) and (b) are shown in figure 5.7a and 5.7b, and for case (c) in figure 5.8. $\log(\sigma_{AC})$ versus $\log(f)$ plot for case (c) yields a typical 0.8 slope. This clearly indicates the small polaron conduction for hole hopping process. For case (a) and (b), due to high electron concentration, this type of slope was not observed in the testing temperature and frequency range. The irregular increase of conductivity around 100 to 1kHz at higher temperature is due to the electrode polarization which is clarified using complex impedance analysis. It is therefore not possible to draw the conclusion for electron conduction mechanism based on the AC conductivity data alone. The temperature dependence of DC and AC conductivity at 10 kHz do not differ within the experimental error, which again indicates that the conduction is purely electronic (Nagels, P., 1980). One example is shown in figure 5.9 for case (b). The deviations between DC and AC conductivity for low frequency data at
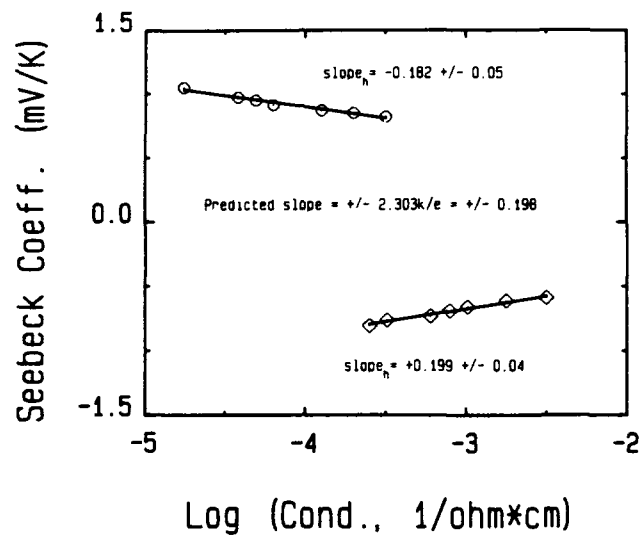
Figure 5.5 Jonker analysis of Seebeck coefficient and conductivity, showing the nature of concentration independent charge carrier mobility.
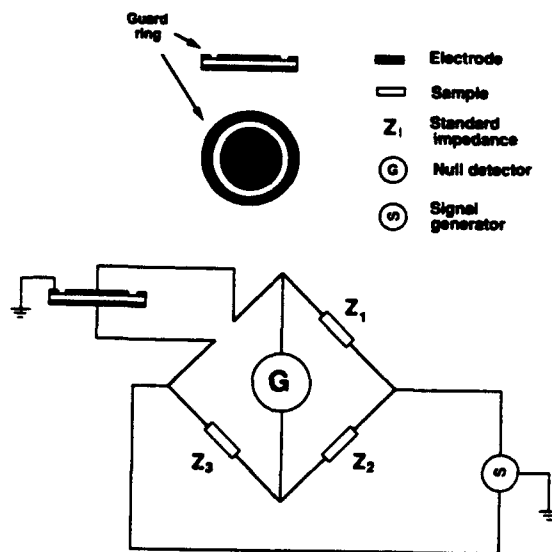
Figure 5.6 The electrode configuration of a three-probe electrode with guard ring. The testing circuit shows a way to eliminate the surface conduction.
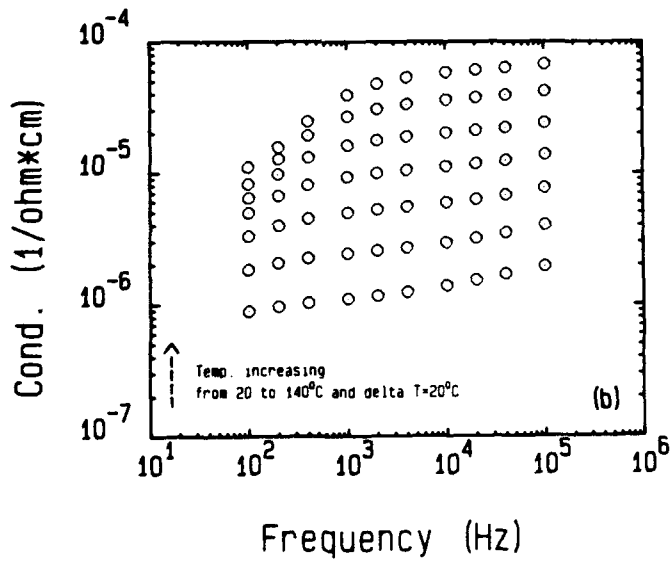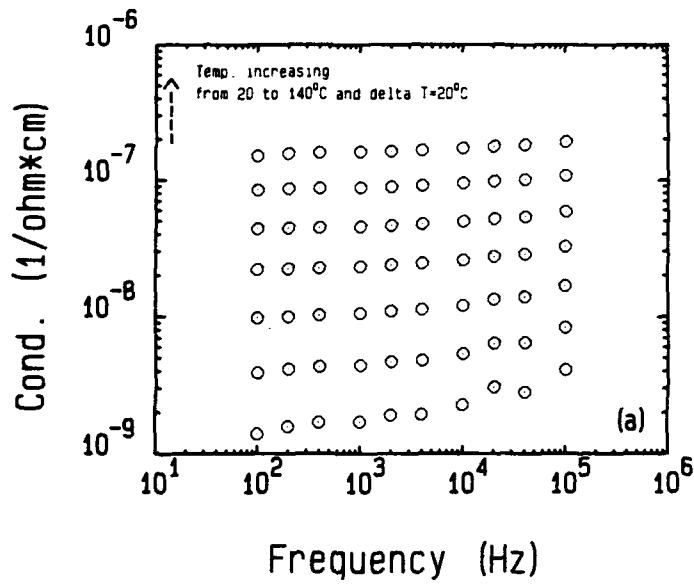
124

Figure 5.7 Log(σ_{ac}) vs log(f) for stoichiometric BZN equilibrated at 1300°C, $V_{CO_2/CO}$=0.471 and (a) cooled under the equilibrium condition, and (b) quenched to room temperature.
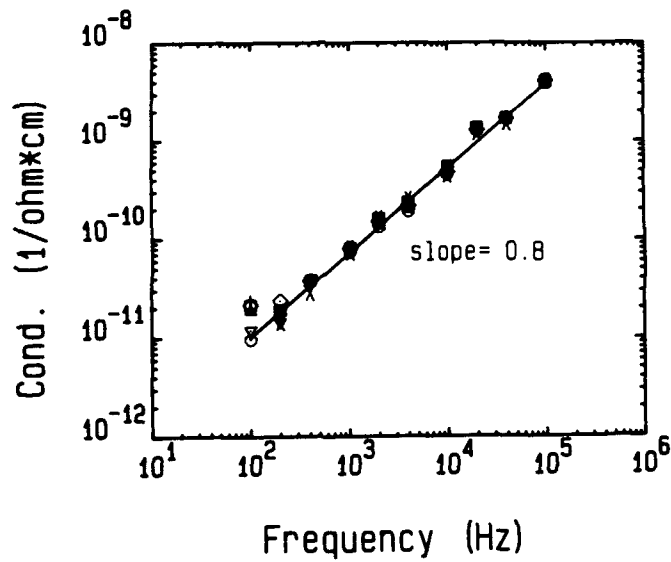
Figure 5.8 Log(σ_{ac}) vs log(f) for stoichiometric BZN equilibrated at 1300°C, O_2 and quenched to room temperature, showing a typical hopping type conduction.
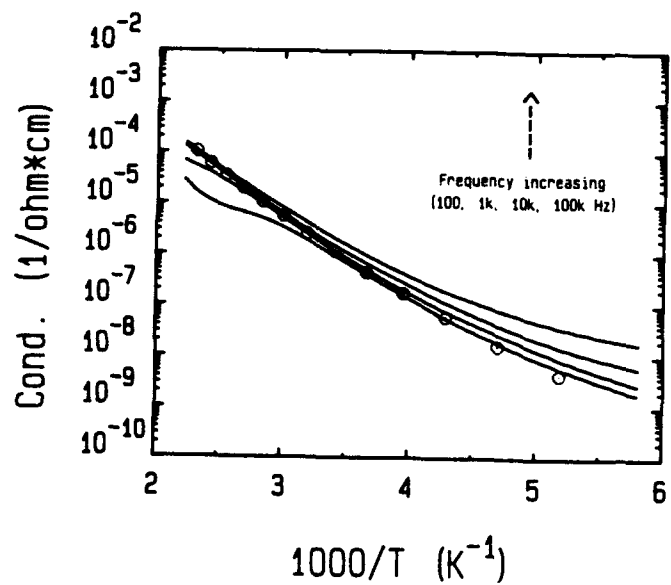
Figure 5.9 Arrhenius plot of DC (open circle) and AC (solid line) conductivity for stoichiometric BZN equilibrated at 1300°C, $V_{CO_2/CO}$=0.471 and quenched to room temperature.

126

high temperature and high frequency at low temperature are due to electrode polarization and small polaron nature of electronic conduction, respectively.

Low temperature DC conductivity was obtained using complex plane impedance analysis. Since low temperature DC conductivity is difficult to measure mainly because of large contact and bulk resistance, relatively easier measurement of dielectric properties in this case becomes feasible. Impedance analysis has the feature of separating the bulk and interface effects (such as grain boundary resistance and electrode resistance) and is therefore suitable for low temperature DC conductivity determination (see chapter 1). Figure 5.10a, b show two of such plots for samples (a) and (b) measured at 84°C in air. The impedance data were calculated from either Y/θ or C/G. The computer simulation based on the appropriate equivalent circuit was performed by the Cyber 850 main frame. Arrhenius plots of bulk DC conductivity obtained in this way for cases (a) and (b) are shown in figure 5.11 where non-adiabatic small polaron model is still used. The similar activation energy for both cases at low temperature indicates the same conduction mechanism. Comparing the two cases, the only difference is a higher electron concentration for the quenched case (b) which results in a higher level of σ. This is because part of the high temperature state gets quenched-in at low temperature. The linear relationship between $\log(\sigma T^{3/2})$ and $1/T$ gives an activation energy of about 0.47 eV. This obviously is not due to the thermally activated mobility only with a fixed electron concentration ($\Delta H_m(e)=0.33$ eV). It may be due to a hopping process along with some sort of trapping.

To clarify these issues, dielectric relaxation analysis was carried out for samples (a) and (b). Figure 5.12a shows a sample plot of dielectric dissipation factor $\tan\delta$ as a function of temperature at ten frequencies for sample (b). The typical single Debye type peak at lower temperature can be used to derive the activation energy for "dipole" hopping of a charge carrier around its bound center. The relatively broad single Debye peak may be due to the unsatisfied dilute solution criterion (electron concentration was calculated to be around 10^{21} cm^{-3} under quenched condition). The other possible high temperature peak could be due to electrode processes or Maxwell-Wagner type relaxation arising from macroinhomogeneity (Tien, Z.Y., et.al., 1967) which is of no current interest to us. The relaxation time τ of the bound charge carrier, i.e. the polaron, is plotted in figure 5.12b for sample(b). Using equation (1.30), the hopping energy is determined to be 0.32 eV. It is important to point out that the hopping energy is in an excellent agreement with that determined at high temperature using the

127
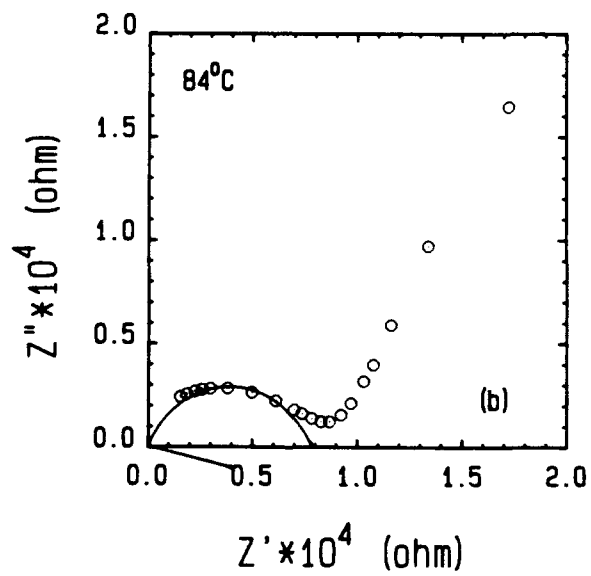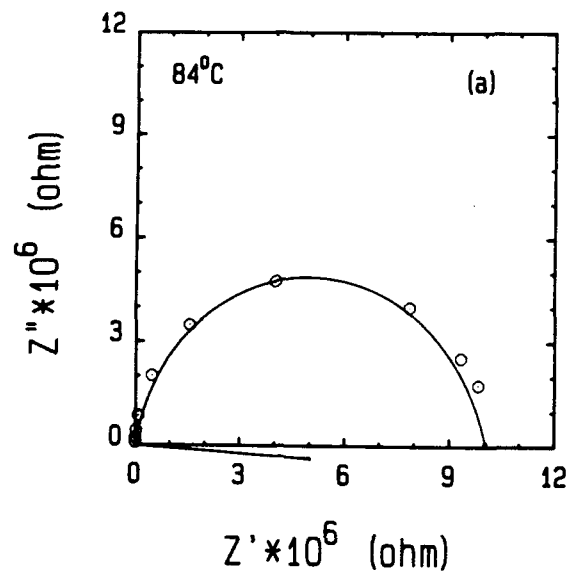
Figure 5.10 Samples of impedance plot (Z'' vs Z') for stoichiometric BZN equilibrated at 1300°C, $V_{CO_2/CO}=0.471$ and (a) cooled under the equilibrium condition; (b) quenched to room temperature. Samples were measured at 84°C.
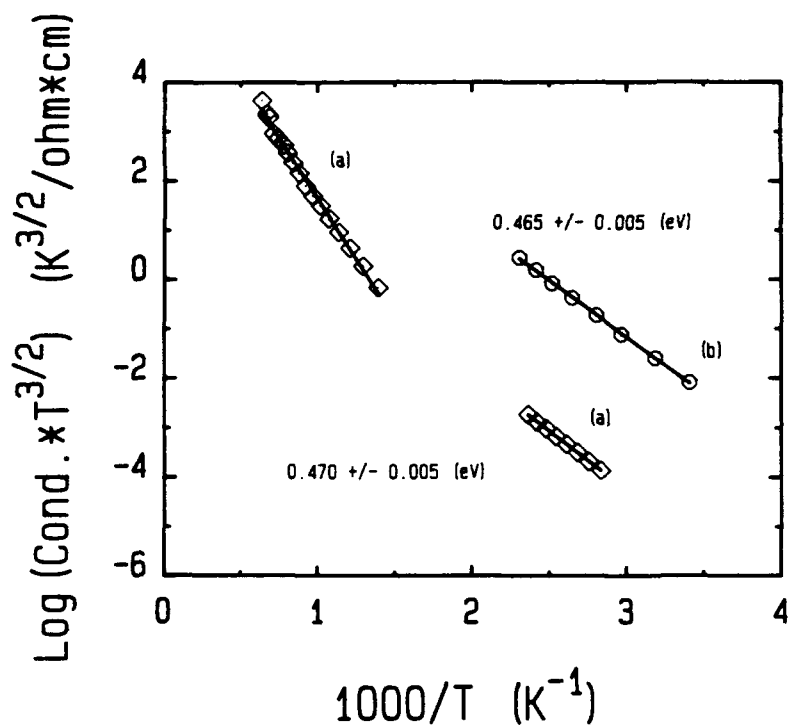
Figure 5.11 Log($\sigma_{dc}T^{3/2}$) vs 1000/T for stoichiometric BZN measured at $V_{CO_2/CO}$=0.471 and cooled under equilibrium condition (a). For low temperature cases, measurements were conducted on the samples equilibrated at 1300°C, $V_{CO_2/CO}$=0.471 and cooled under equilibrium condition (a) and quenched to room temperature (b). The DC conductivity was determined using complex plane impedance analysis.
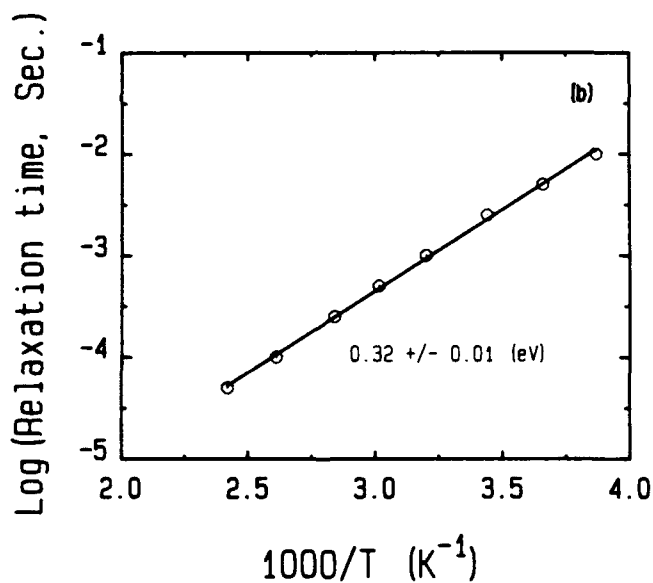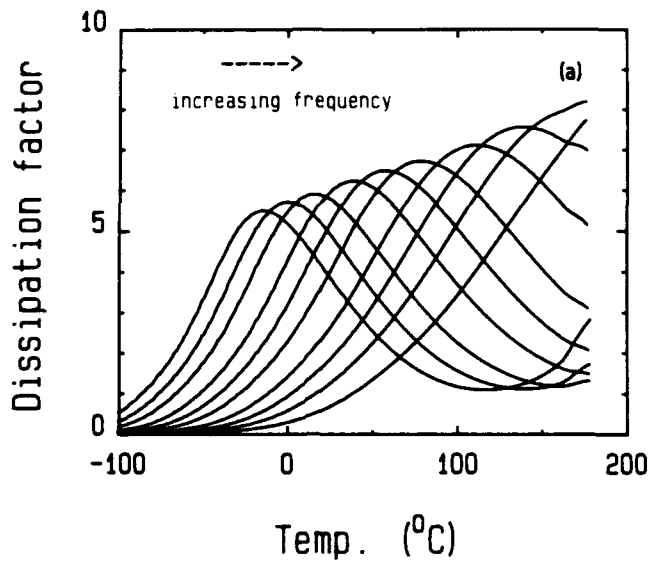
Figure 5.12 (a) A sample plot of temperature spectrum of dissipation factor for stoichiometric BZN equilibrated at 1300°C, $V_{CO_2/CO}$=0.471 and quenched to room temperature, showing a typical Debye type relaxation (scanning frequencies are 100, 200, 400, 1k, 2k, 4k, 10k, 20k ,40k, and 100kHz). (b) Arrhenius plot of relaxation time for the same sample .

combination of DC equilibrium conductivity and Seebeck coefficient. This therefore provides strong support for the non-adiabatic small polaron model. This type of analysis is also useful for distinguishing between the adiabatic and the non-adiabatic small polaron model if there is no Hall measurement available.

It is common practice that the occurrence of dielectric relaxation can be attributed in general to the presence of either macroscopic or microscopic inhomogeneities in the sample. Macroscopic inhomogeneities having dimensions that are large compared to a lattice constant, can be located either at the surface of the sample, e.g. high-ohmic layers directly underneath the measuring electrode, or in the bulk, e.g. grain boundary layers. Microscopic inhomogeneities consist of either single center or small groups of centers. These centers can be introduced into lattice by either incorporation of impurities and redox reactions or correspond to native defects. We have already discussed the dielectric relaxation originating from the microscopic inhomogeneity. Although relaxation due to macroscopic inhomogeneities is of no interest for the present purpose, we should, however, be able to recognize these effects in order to exclude them from our experimental results. Surface effects manifest themselves in an apparent dielectric constant which is a function of the thickness of the sample, whereas in the case of bulk effects, the dielectric constant is independent of this parameter. Bulk effects due to macroscopic inhomogeneities in general have the features that the $\tan(\delta)$ peak frequency or temperature position is a function of dopant concentration, while the magnitude of $\tan(\delta)$ is independent of temperature. This contrasts with the behavior found in general for the case of bulk effects due to microscopic inhomogeneities. In order to eliminate these possibilities, a series of additional experiments have been designed:

(1) I-V characteristic of samples with different electrodes was carried out to make sure that the OSC level (oscillation level) for actual measurements is correct.

(2) Ag paste and evaporated Au electrode were tested on the same sample to see if there is any electrode polarization effect.

(3) Same samples with different thicknesses were measured to check if the same bulk properties were measured.

The testing results are summarized as follows:

(1) The OSC level of all our measurements was chosen from 0.1 to 1 V which was proven to be within the ohmic range by I-V characteristic testing. Experimental results

131

on the same sample with different OSC levels within this range did not show any difference. This also means that the weak field approximation for dielectric relaxation measurements is valid.

(2) Different electrodes did generate different electrode polarization. It appears that the Ag electrode gives rise to a more serious electrode polarization problem. For example, figure 5.13 shows the impedance plot for the same sample with Au or Ag electrode. It is clear that data obtained with the Ag electrode are not reliable.

(3) All the calculations and analyses are based on the samples measured using Au electrode. In order to justify this electrode, after a measurement at one thickness the sample was ground and measured again. This thickness varying method did not reveal any difference in terms of measured C/G values. For example, the ratio of thickness of two samples with the same cross sectional area is 1.58; the measured ratio for capacitance C and conductance G is in the range of 1.5~1.6. Figure 5.14 illustrates the impedance plot for two samples with thickness ratio 1.58. The $Z'(\omega=0)$ ratio is about 1.6. Dissipation factors of these samples were also measured and compared. The $\tan(\delta)$ peak position for the same frequency is located at the same temperature, and the peak magnitude is similar.

As discussed above, it is quite clear that what we have measured can be reasonably attributed to the bulk properties caused by microscopic inhomogeneity.

5.2) Enthalpy of Oxidation/Reduction

Reduction and oxidation reactions of stoichiometric BZN can be expressed as equations (1.1) and (1.9), respectively. For convenience they are written below:

For reduction: $O_O = \frac{1}{2}O_2 + V_O^{\cdot\cdot} + 2e'$ (1.1)

For oxidation: $\frac{1}{2}O_2 + V_O^{\cdot\cdot} = O_O + 2h^{\cdot}$ (1.9)
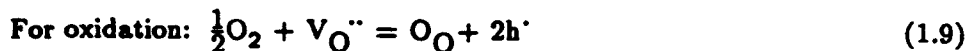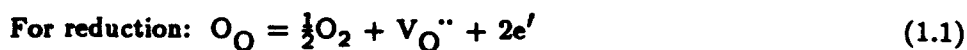
Corresponding mass action relation are expressed by equations (1.13) and (1.14), respectively.

$$K_R = \frac{[V_O^{\cdot\cdot}]n^2 P_{O_2}^{-1/2}}{[O_O]} = K_R' \exp(-\Delta H_R/kT)$$ (1.13)
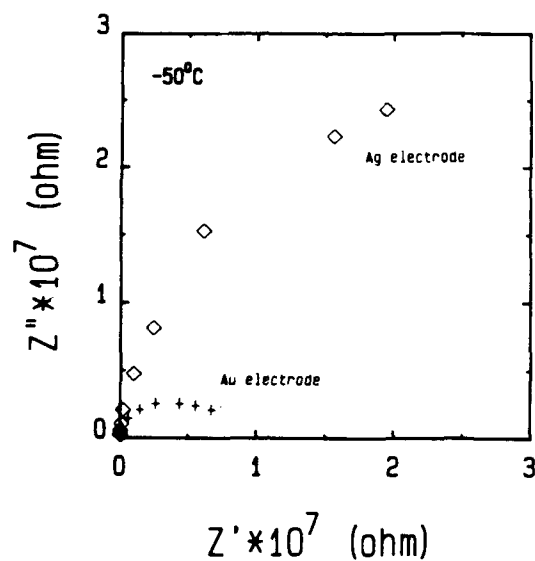
Figure 5.13 Impedance plot of stoichiometric BZN equilibrated at 1300°C, $V_{CO_2/CO}$=0.471 and quenched to room temperature with either Ag or Au electrode, showing different electrode process.
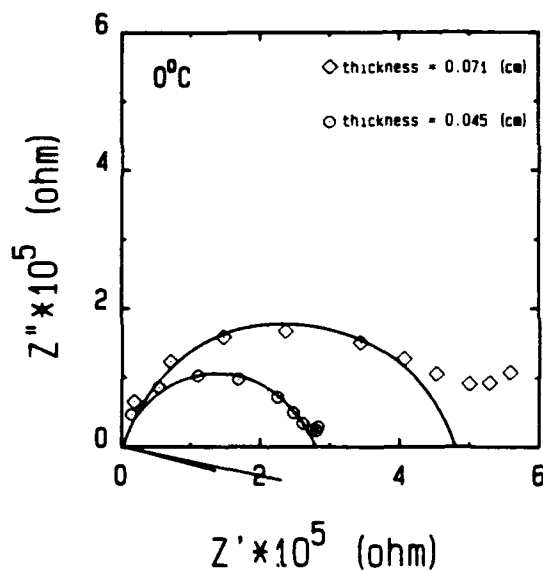
Figure 5.14 Impedance plot of stoichiometric BZN equilibrated at 1300°C, $V_{CO_2/CO}$=0.471 and quenched to room temperature with different sample thickness, showing the same ratio for the impedance and thickness between samples.

$$K_O = \frac{[O_O]p^2}{[V_O\text{\textquotedblright}]P_{O_2}^{-1/2}} = K_O{}'\exp(-\Delta H_O/kT) \tag{1.14}$$

From these equations, if the oxygen vacancy concentration is fixed by some intrinsic acceptor level, we can get

$$n \propto \exp(-\Delta H_R/2kT) \tag{5.13}$$

and $\quad p \propto \exp(-\Delta H_O/2kT) \tag{5.14}$

The enthalpy of reduction and oxidation can be therefore determined from equations 5.13 and 5.14 as

$$\Delta H_R = 4.66 \pm 0.2 \text{ eV and } \Delta H_O = 2.74 \pm 0.3 \text{ eV.}$$

5.3) *Band Gap and Optical Absorption*

The indirect band gap at zero degree kelvin of stoichiometric BZN may be obtained by manipulating equations (1.6), (1.11), (1.1), (1.13), (1.9), (1.14) and (5.13), (5.14) based on the experimental data

$$\begin{aligned} K_R K_O &= (np)^2 = \kappa_i^2 \\ &= K'_R K'_O \exp\{-(\Delta H_R + \Delta H_O)/kT\} = K'^2_i \exp(-2E_g{}^{(o)}/kT) \end{aligned} \tag{5.15}$$

Therefor $\quad E_g{}^{(o)} = \dfrac{\Delta H_R + \Delta H_O}{2} = 3.70 \pm 0.25 \text{ eV} \tag{5.16}$

Considering the non-adiabatic small polaron model and equivalent mobilities for electron/hole, the Arrhenius plot of conductivity minimum corrected for mobilities yields an energy 3.82 ± 0.11 eV (see figure 4.14b). Such a result is expected in this type of analysis.

Optical absorption studies were also carried out on stoichiometric BZN in the wave length range from 500nm to 200nm at room temperature using a Cary 2300 optical spectrometer. No additional information was gathered. It is well known that

the band gap determined by optical absorption can be different from that determined by conductivity measurements. Measurement of band gap by optical absorption is able to detect the presence of both direct and indirect band gap, while that by conductivity can only reveal the indirect band gap. As shown in figure 5.15, optical threshold energy $h\omega = E_g \pm h\Omega$, where Ω is the frequency of an emitted phonon. The $h\omega$ can be large or smaller than E_g depending on the temperature (Kittel, C., 1986). However, the phonon energy is characteristically small (0.01−0.03 eV) in comparison with the energy gap. Theoretically speaking, we do not expect the energy value by optical measurement to vary significantly from that by conductivity. From figure 5.16, the absorption edge is not sharp enough to determine the band gap. From the onset to the end of the absorption intensity, energy is located around 3.2~4.0 eV. Although these data are not ideal, the energy range obtained by the optical absorption is still a good reference. Nevertheless, the general trend is satisfactory.
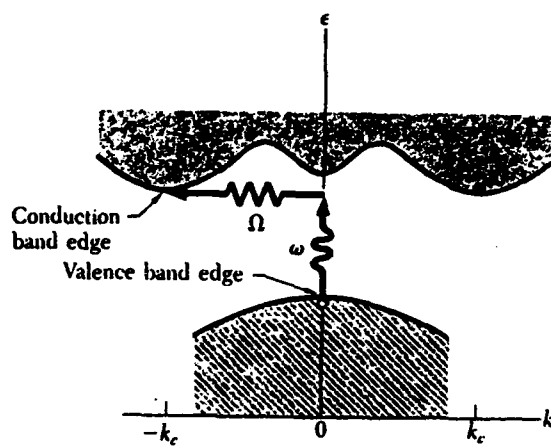
Figure 5.15 Energy associated with indirect process showing indirect band gap determined by optical absorption.
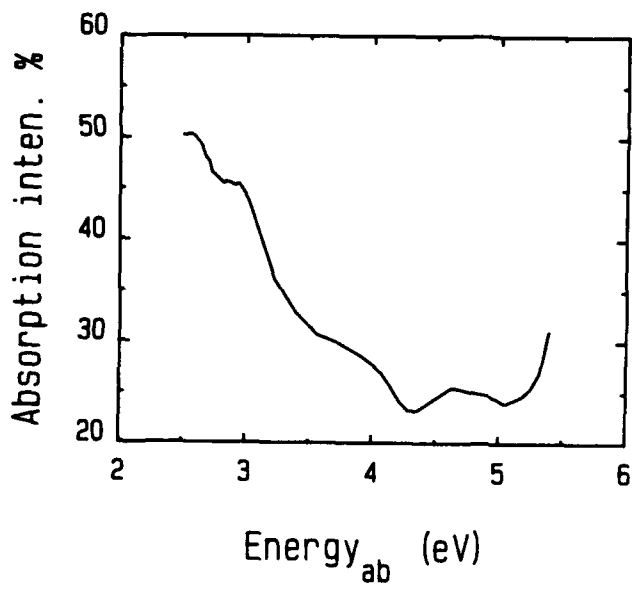
Figure 5.16 Relative diffuse absorption intensity as a function of absorption energy for stoichiometric BZN sintered at 1600°C for 3 hours and furnace cooled.

6.1) *Defect Model of BZN*

Now we are in a position to draw a defect diagram and to computer simulate the experimental data for BZN. First of all, we will go through some basic discussion before deriving the defect diagram.

(1) Schottky defect for intrinsic ionic disorder.

(2) B site cations are treated as an identical one cation with effective valence $+4$ for continuous phase no matter whether it is in its disordered or 1:2 ordered state. The Schottky disorder may be written as

$$nil = V_{Ba}'' + V_{B}'''' + 3V_{O}^{\cdot\cdot} \tag{6.1}$$

and the Mass Action relation is

$$K_s = [V_{Ba}''][V_{B}''''][V_{O}^{\cdot\cdot}]^3 \tag{6.2}$$

(3) Similar to its parent BT, high $V_{O}^{\cdot\cdot}$ levels in intrinsic stoichiometric BZN can be attributed to following possible sources:

(a) Intrinsic disorder.

(b) Deviation from ideal Ba/B ratio.

(c) Deviation from ideal Zn/Nb ratio.

(d) Zn loss during high temperature sintering.

(e) naturally occurred acceptor impurities.

The ABO_3 perovskite structure can be viewed as a close-packed cubic array of composition AO_3, with the B cations in all available octahedral sites having only oxygen as nearest neighbors (figure 4.18). There is clearly no room for O_I''. The Schottky disorder does generate $V_{O}^{\cdot\cdot}$ along with V_{Ba}'' and V_{B}''''. However, the lack of cation diffusion in this type of structure implies that this type of disorder cannot be large. Thus a significant intrinsic source of $V_{O}^{\cdot\cdot}$ caused by Schottky disorder is unlikely. With regard to the Ba/B ratio, it has been shown that very small solubility limit in

BT($\sim$100ppm, Hu, Y.H. et.al., 1985; Sharmar, R.K., et.al., 1981). In the case of BZN, we did try to put Ba into B site without any success. It is also unlikely for ions as small as Zn or Nb to occupy Ba sites. This effect is not favorable either. Factors (c) through (e) are playing an important role for generating oxygen vacancies. Because of uncertainty in the Zn/Nb ratio during sample preparation, ZnO loss during high temperature sintering and unavoidable acceptor type impurities, charge neutrality requires corresponding oxygen vacancies to compensate these defects. As we mentioned at the first part of this chapter, loss of ZnO during sintering may cause the Nb ion to exchange its position between Zn and Nb sites. The resulting $V_{Zn}{}''$ and $V_{Nb}{}'''''$ are treated as one B site vacancy $V_B{}''''$. The relation between these defects is either

$$2[V_O^{..}] = [A'] + 3[Zn_{Nb}{}'''] + 4[V_B{}''''] \qquad (6.3)$$
$$\text{or} \quad 3[Nb_{Zn}^{...}] + 2[V_O^{..}] = [A'] + 4[V_B{}'''] \qquad (6.3)'$$

Therefore, stoichiometric BZN may be either acceptor doped or donor doped depending on the actual Zn/Nb ratio, and how much ZnO is lost during the sintering.

Now we ought to ask ourselves a question: up to what degree can we attribute the $V_O^{..}$ to a Zn/Nb ratio deviation plus $V_B{}''''$ due to processing, such as an error in weighing chemicals and high temperature ZnO loss? From the slope transition point of stoichiometric BZN in figure 6.1, $[V_O^{..}]$ is estimated to be in the neighborhood of 1500 ppm (atom) using equation (1.22) and can be as low as 665 ppm. Considering the starting chemicals and processing technique that were used, it is not reasonable to attribute such a high $[V_O^{..}]$ to impurities alone. Taking $[A']$ as 200 ppm, for example, and assuming there is no Zn evaporation problem, we could end up with acceptors ($[Zn_{Nb}{}''']$) from the Zn/Nb ratio deviation in the range of $\sim$340 ppm. In fact, the Zn loss after high temperature sintering could be in the vicinity of a few thousand ppm or higher (chapter 3). Because the conductivity vs Po_2 plot of all stoichiometric BZN samples produced from different batches are always located in between the two curves as shown in figure 6.1, in spite of the variation in the Zn/Nb ratio, it is clear that the ZnO loss during sintering is a major source for the increase of oxygen vacancies. One further point needs to be mentioned here. If there is a vacant Zn site, the system tends to shift Nb onto Zn sites creating $V_{Zn}{}''$ and $V_{Nb}{}'''''$. 1:2 type ordering is therefore enhanced which was observed experimentally. However, unlike deliberately making Nb rich and
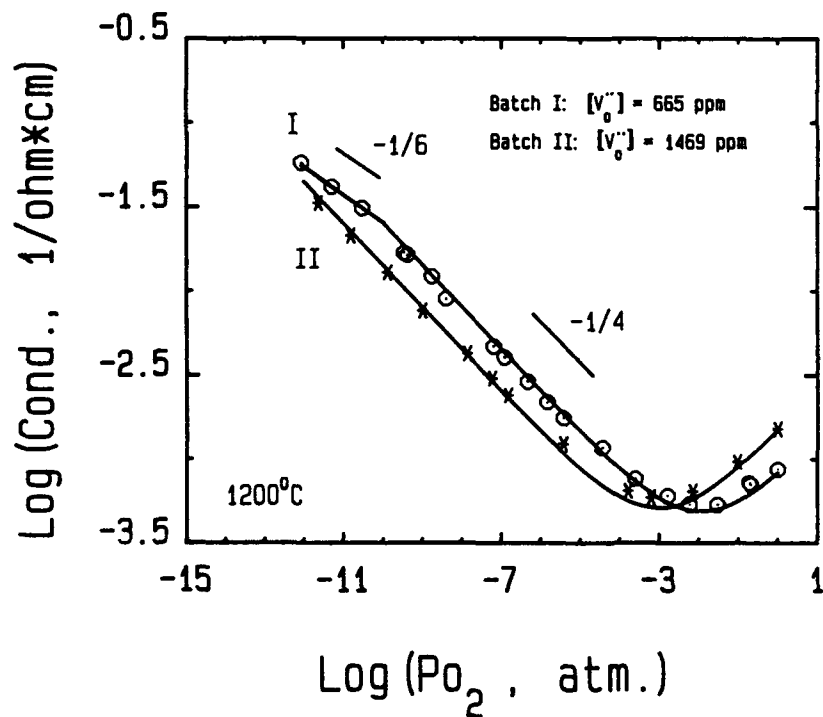
Figure 6.1 Computer simulation of two batches stoichiometric BZN with the same starting formula based on the non-adiabatic small polaron model at 1200°C, showing the different concentration level of oxygen vacancy.

139

Zn deficiency in the starting formula where overall B site cations remain unity, the ZnO loss from stoichiometric BZN causes a change of the A/B ratio which will result in the increase of oxygen vacancy concentration. Now we can draw two conclusions based on the above discussion. One is that stoichiometric BZN may be in its either acceptor doped or donor doped state. We are inclined to favor that stoichiometric BZN is always in its acceptor state based on the experimental results (figure 6.1), because there are certain experimental limitations which lead to these results. (1) ZnO is the lightest chemical in the starting formula which results in the largest error during the weighing process. (2) The Zn loss at high temperature is the largest source of $V_O^{..}$. It usually buries the "mistake" of Zn/Nb ratio if Zn/Nb < 1/2 by accident. The other conclusion is that the intrinsic $[V_B'''']$ is always higher than $[V_{Ba}'']$.

Based on these conditions, we now may draw the defect diagram as follows:

(1) "stoichiometric"_acceptor doped BZN. The overall charge neutrality condition is either

$$p + 2[V_O^{..}] = [A'] + 3[Zn_{Nb}'''] + 2[V_{Ba}''] + 4[V_B''''] + n \qquad (6.4)$$

or $\quad 3[Nb_{Zn}^{...}] + p + 2[V_O^{..}] = [A'] + 2[V_{Ba}''] + 4[V_B''''] + n \qquad (6.4)'$

Because of fixed high intrinsic $V_O^{..}$ level by acceptors, the mass action relation for Schottky disorder (6.1) can be rewritten as

$$[V_{Ba}''][V_B''''] = K_s/[V_O^{..}]^3 \qquad (6.5)$$

due to ZnO loss during the sintering, as mentioned before, $[V_B'''']$ is quite high in general. This leads to very small $[V_{Ba}'']$, which becomes a minority defect. We will not draw it in this part of the defect diagram. For simplicity, we assume that ZnO loss can be ignored during the defect chemistry measurement. The initial $[V_B'''']$ can therefore be combined into a starting acceptor level which fixes $[V_O^{..}]$. In fact, this assumption is reasonable considering small ZnO loss below 1300°C and the sensitivity of $\log(\sigma)$ vs $\log(Po_2)$ plot which would shift if there was a continuous loss of ZnO during the measurement (Chan, N.H., et al., 1982). By analogy with BT (chapter 1), and considering the majority defects in this system as e', A', Zn_{Nb}''', V_B'''', $h^.$, $Nb_{Zn}^{...}$ and

$V_O^{..}$, the $V_O^{..}$ can be expressed as either

$$2[V_O^{..}] \cong [A'] + 3[Zn_{Nb}'''] + 4[V_B''''] \tag{6.6}$$

$$\text{or} \qquad 2[V_O^{..}] \cong [A'] + 4[V_B''''] - 3[Nb_{Zn}^{...}] \tag{6.6}'$$

The defect diagram of "stoichiometric"_acceptor-doped BZN is shown in figure 6.2(a).

(2) Donor doped BZN. The overall charge neutrality condition in this case is either

$$p + 2[V_O^{..}] + [D^{.}] = [A'] + 3[Zn_{Nb}'''] + 2[V_{Ba}''] + 4[V_B''''] + n \tag{6.7}$$

$$\text{or} \quad p + 3[Nb_{Zn}^{...}] + 2[V_O^{..}] + [D^{.}] = [A'] + 2[V_{Ba}''] + 4[V_B''''] + n \tag{6.7}'$$

The discussion here is divided into two parts: lightly doped and heavily doped cases. For the lightly doped case, the defect diagram is quite straightforward. Analogous to BT (chapter 1). The donor impurity is compensated by electrons. For small donor concentrations, the donor compensates the acceptors which is equivalent to reducing the acceptor level (figure 1.6). The defect diagram does not look too much different from the acceptor doped case except the -1/6 to -1/4 slope transition point moves towards high oxygen partial pressure and the minimum point shifts to higher oxygen partial pressure with increasing donor content. This trend continues until the -1/6 sloped line reaches the minimum point. Upon increasing the donor level, the transition point from -1/6 slope to flat where electron concentration is equal to donor concentration moves towards lower oxygen partial pressure (figures 4.16, 6.2(b) and 1.6). The majority defect $V_O^{..}$ now will decrease as -1/2 slope because

$$n = [D^{.}] \tag{6.8}$$

From equation (2.1), $[V_O^{..}] \propto P_{O_2}^{-1/2}$

and from equation (6.2), $[V_{Ba}''][V_B''''] \propto P_{O_2}^{3/2}$. The minority defects start increasing till they eventually hit the donor level and the electronic compensation turns

141
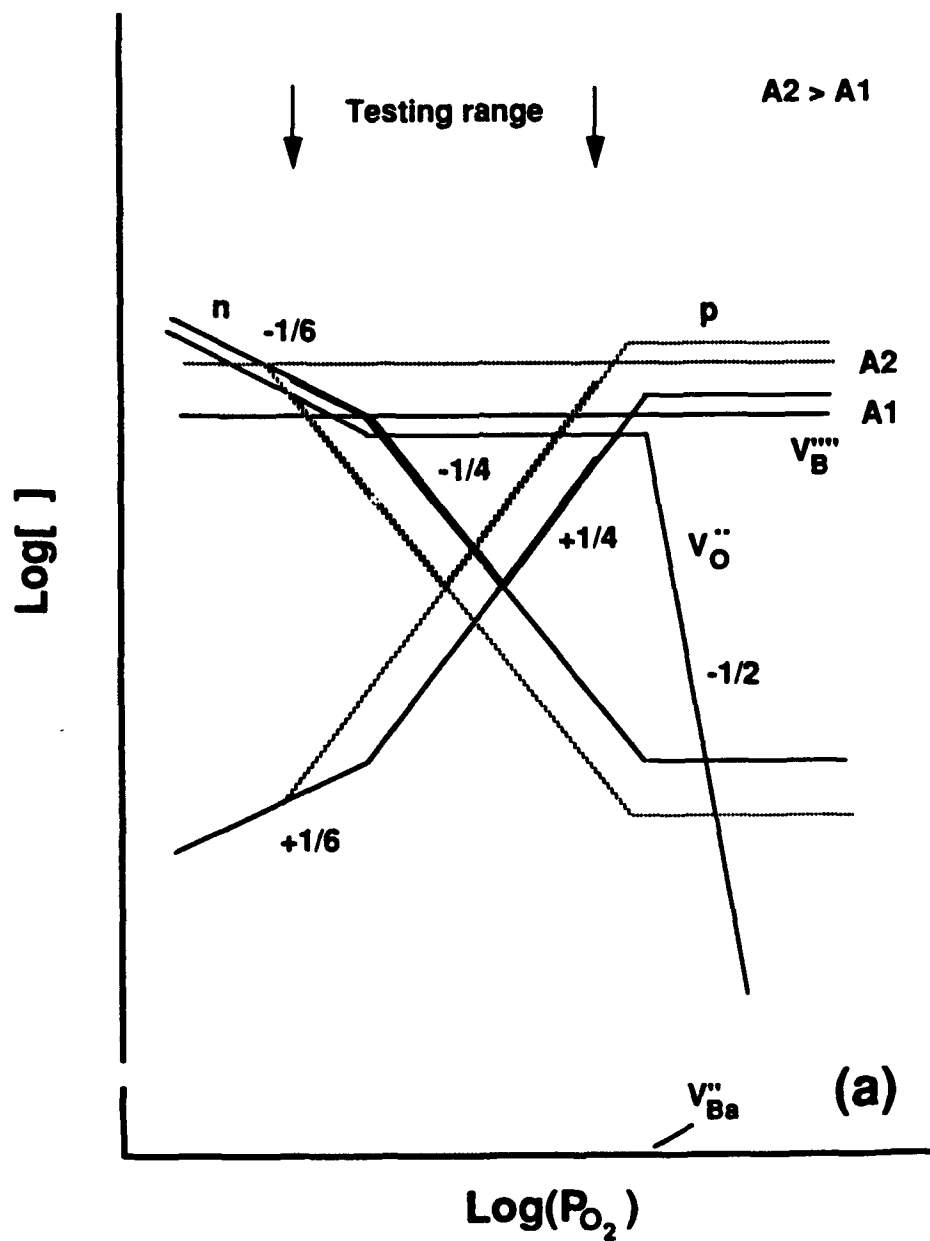
Figure 6.2a Defect model of stoichiometric_acceptor doped BZN

142
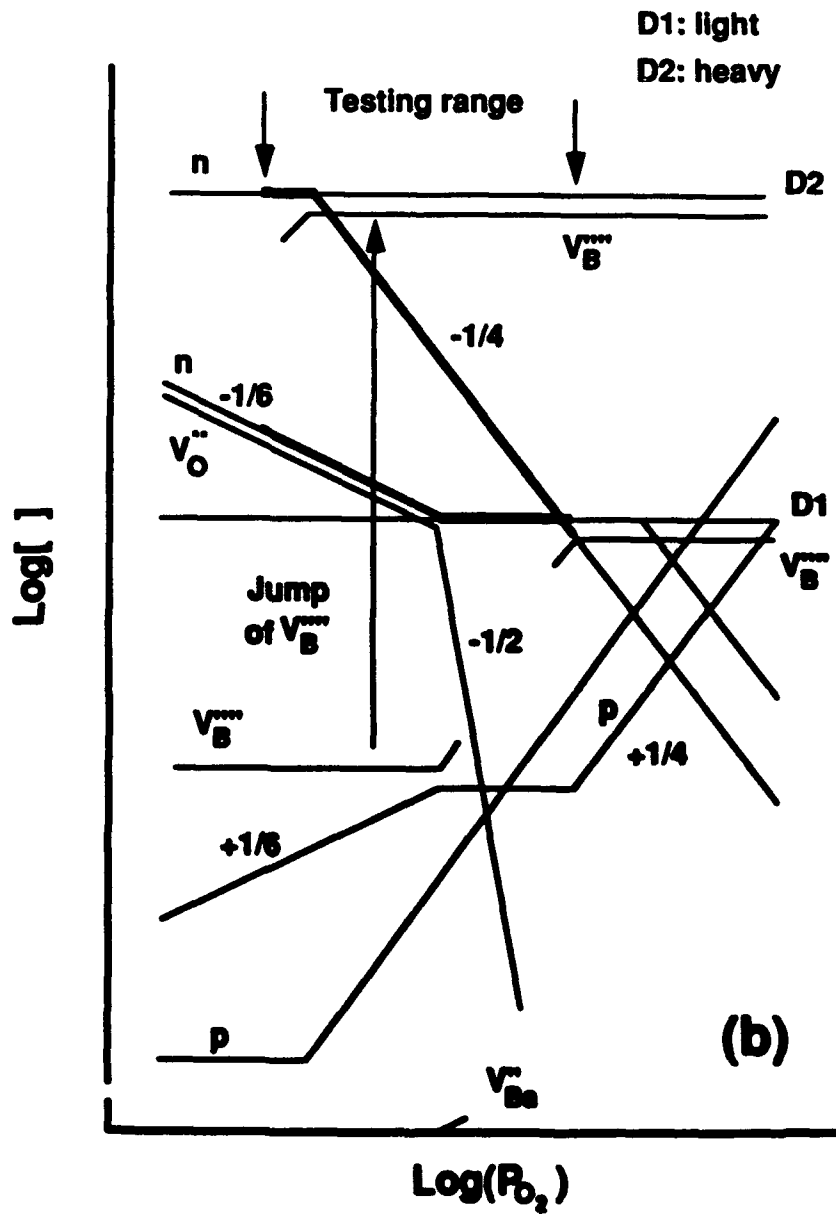
Figure 6.2b Defect model of donor doped BZN

into the ionic compensation case. For the heavily doped case, the situation becomes very complicated. First, the donors are no longer compensated by electrons. They are compensated by metal vacancies. The original minority defects in the lightly doped case now become majority defects which introduces great difficulty into the defect diagram construction because of the multi-component nature in BZN. Second, since $[V_B'''']$ is always higher than $[V_{Ba}'']$, it is $[V_B'''']$ that first reaches the donor level and then is fixed by the donor. But there is no simple arithmetic relation in terms of the slope of concentrations as a function of $log(Po_2)$. Third, in order to observe this vacancy compensation mechanism in the testing oxygen partial pressure range (marked in figure 6.2b), $[V_B'''']$ must increase abruptly. The same situation exists in BT (figure 4.3 and Daniels, J. et.al., 1976). Over the past half century, there has been no satisfactory model which can explain this peculiar phenomenon. We intend to interpret this behavior based on the ordering of B site cations and vacancies in BZN. The ordering lowers the formation energy of vacancies V_{Zn}'' and V_{Nb}''''' and increases the vacancy concentration drastically. This is in agreement with the elimination of the 1:1 type ordering in Zn rich_acceptor doped BZN and the promotion of the 1:2 type ordering in Nb rich_donor doped BZN. However, there is no evidence of any kind of ordering or defect complex formation in heavily donor doped BT but it does show the same behavior as BZN. This may mean: (1) this explanation is not correct; (2) the interpretation is somewhat true but current characterization techniques are not sensitive enough to detect any ordering or defect complex in heavily donor doped BT. Further experiments, especially for heavily donor doped BT, are required which will be discussed in chapter 8.

6.2) *Computer Simulation*

After determining the defect model, we can now calculate the defect concentration for majority defects and mass action constants for reduction and oxidation. Finally we will simulate the experimental data to check if the model is correct.

The calculation is based on the following equations. For convenience, we rewrite those equations here (the simulation is only for stoichiometric and acceptor doped cases at present).

For reduction: $\quad O_O = \frac{1}{2}O_2 + V_O^{\cdot\cdot} + 2e'$ \hfill (1.1)
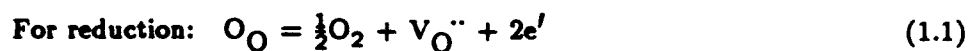
(a) $n = 2[V_O^{\cdot\cdot}]$ \hfill (1.1)'

$$n = \{2K_R[O_O]\}^{1/3} P_{O_2}^{-1/6} \text{ and } [O_O] = N_o - [V_O^{\cdot\cdot}] \qquad (6.9)$$

Where N_O is total number of oxygen site.

$$p = K_i^{\frac{1}{3}} \{2K_R[O_O]\}^{-1/3} P_{O_2}^{+1/6} \qquad (6.10)$$

(b) $2[V_O^{\cdot\cdot}] \cong [A'] + 3[Zn_{Nb}{}'''] + [V_B{}''''] = \text{constant} \qquad (6.11)$

or $\quad 2[V_O^{\cdot\cdot}] \cong [A'] + [V_B{}''''] - 3[Nb_{Zn}^{\cdots}] = \text{constant} \qquad (6.11)'$

$$n = \{\frac{K_R[O_O]}{[V_O^{\cdot\cdot}]}\}^{1/2} P_{O_2}^{-1/4} \text{ and } [O_O] = N_o - [V_O^{\cdot\cdot}] \qquad (6.12)$$

$$p = K_i^{\frac{1}{2}} \{\frac{K_R[O_O]}{[V_O^{\cdot\cdot}]}\}^{-1/2} P_{O_2}^{+1/4} \qquad (6.13)$$

For oxidation, $\quad \frac{1}{2}O_2 + V_O^{\cdot\cdot} = O_O + 2h^{\cdot} \qquad (1.9)$

(a) $2[V_O^{\cdot\cdot}] \cong [A'] + 3[Zn_{Nb}{}'''] + [V_B{}''''] = \text{constant} \qquad (6.14)$

or $\quad 2[V_O^{\cdot\cdot}] \cong [A'] + [V_B{}''''] - 3[Nb_{Zn}^{\cdots}] = \text{constant} \qquad (6.14)'$

$$p = \{\frac{K_O[V_O^{\cdot\cdot}]}{[O_O]}\}^{1/2} P_{O_2}^{+1/4} \text{ and } [O_O] = N_o - [V_O^{\cdot\cdot}]_o + \frac{p}{2} \qquad (6.15)$$

where $[V_O^{\cdot\cdot}]_o$ denotes the starting oxygen vacancy concentration which is fixed by acceptor level initially.

$$n = K_i^{\frac{1}{2}} \{\frac{K_O[V_O^{\cdot\cdot}]}{[O_O]}\}^{-1/2} P_{O_2}^{-1/4} \qquad (6.16)$$

(b) $p \cong [A'] + 3[Zn_{Nb}{}'''] + [V_B{}''''] = \text{constant} \qquad (6.17)$

or $\quad p \cong [A'] + [V_B{}''''] - 3[Nb_{Zn}^{\cdots}] = \text{constant and } n = \text{constant} \qquad (6.17)'$

$$[V_O^{\cdot\cdot}] = \frac{[O_O]p^2}{K_O}P_{O_2}^{-1/2} \qquad (6.18)$$

Practically, case (b) cannot be observed due to current limitation of available oxygen partial pressure.

Based on these equations, a computer optimization program was developed to simulate the mass action constants K_R, K_O and K_i.

$$K_R = 2.79*10^{48}\exp(-4.66/kT) \quad (cm^{-6}atm.^{\frac{1}{2}}) \qquad (6.19)$$

$$K_O = 2.25*10^{51}\exp(-2.74/kT) \quad (cm^{-6}atm.^{\frac{1}{2}}) \qquad (6.20)$$

$$K_i = 7.92*10^{49}\exp(-3.70/kT) \quad (cm^{-6}) \qquad (6.21)$$

This calculation was carried out on the Cyber 850 main frame. The unavoidable starting acceptor level was calculated using the transition point from -1/6 to -1/4 slope which depends on the processing condition. Figure 6.1 illustrates the $log(\sigma)$ versus $log(P_{O_2})$ of samples coming from two different batches with same starting formula. It shows the different acceptor level due to processing condition such as the uncertainty in Zn/Nb ratio and evaporation of ZnO etc.. Finally, the equilibrium conductivity of stoichiometric BZN at 3 isotherms based on this defect model are calculated in figure 6.3 and 1% acceptor doped BZN in figure 6.4. The experimental results and theoretical calculation are in excellent agreement.
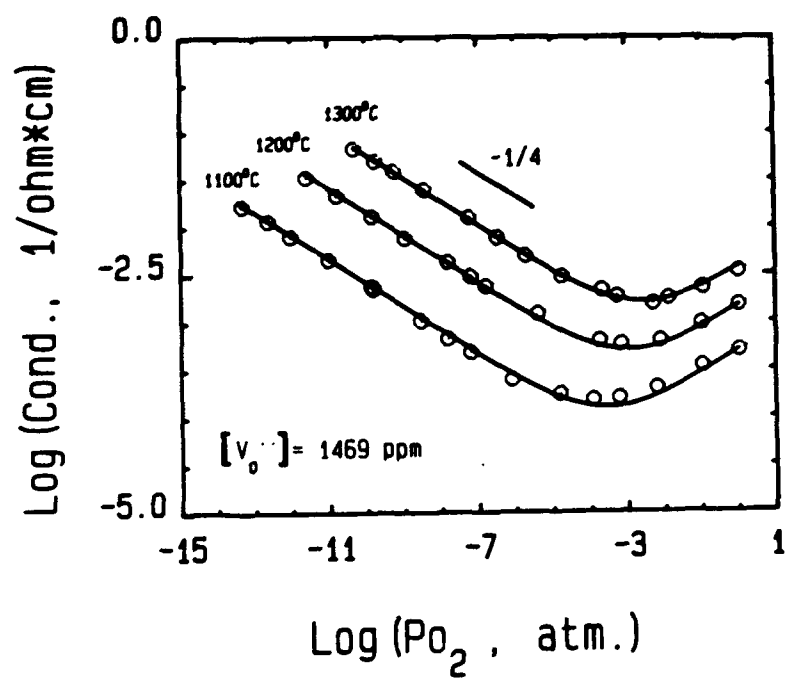
Figure 6.3 Computer simulation os 3 isotherms of $\log(\sigma)$ vs log (Po_2) plot for stoichiometric BZN based on the non-adiabatic small polaron model.
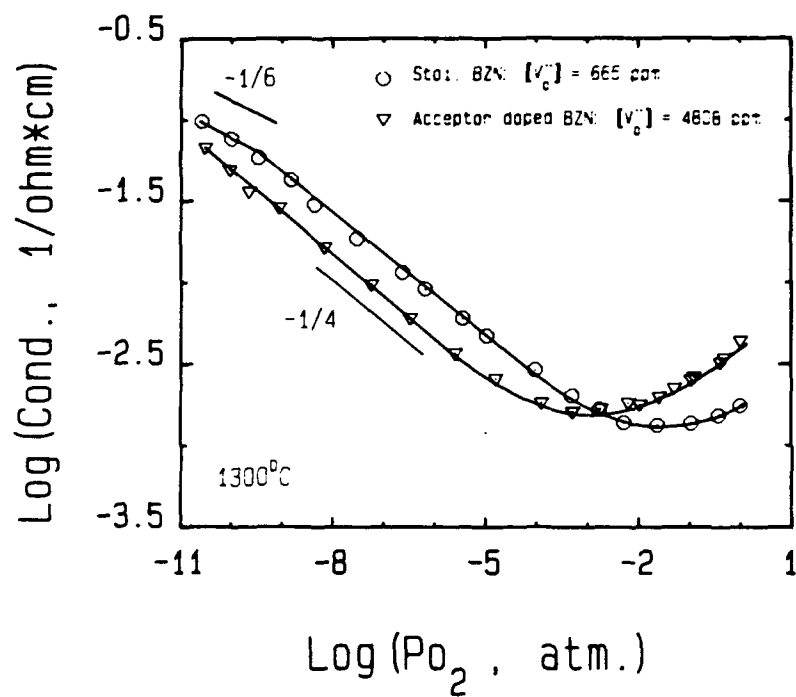
Figure 6.4 Computer simulation of log(σ) vs log (Po$_2$) plot for stoichiometric and 1% acceptor doped BZN based on the non-adiabatic small polaron model at 1300°C.

A systematic study combining dielectric properties, microstructural characterization and defect chemistry/electrical transport properties of the model system BZN has been carried out. This work is believed to be the first attempt on this type of self-compensated complex perovskite system. The main results of this work are briefly summarized below:

(1) Dielectric properties

(a) Stoichiometric perovskite BZN is a paraelectric material with dielectric constant $\epsilon_r \cong 40$, unload dielectric loss quality factor $Q \cong 10^5$ and temperature coefficient at resonant frequency $\tau \cong 10$ ppm.

(b) From the parent system, simple perovskite BT to Complex perovskite BZN, a complete solid solution is formed. With increasing Zn and Nb co-doping into the Ti site in a 1/2 ratio, the resulting BT shows three distinguished features. First, the Curie temperature shifts to lower temperatures; second, three transition temperatures in BT (cubic-tetragonal-orthorhombic-rhombohedral) coalesce; and lastly, the transition becomes more diffuse showing a typical 2nd order phase transition compared with 1st order in undoped BT.

(c) The dielectric properties are interpreted using a phenomenological approach. The Curie temperature shift may be related to the relative ionic radius and polarizability of cations which are substituted for Ti in BT. The diffuse ferroelectric to paraelectric transition may be attributed to the three ferroelectric phases co-existing near the Curie temperature and compositional fluctuation on a nano-scale.

(2) Microchemical ordering

(a) Stoichiometric BZN contains a mixture of 1:1, 1:2 type ordered microdomains and a disordered matrix. The disordered matrix belongs to the space group Pm3m. The 1:1 type of ordered phase belongs to Fm3m and the 1:2 type to P3̄m1.

(b) The 1:1 type ordered microdomains (2~4 nm in size) are randomly distributed, and can be directly imaged with TEM using the CDF technique. The degree of ordering cannot be controlled by heat treatment because of the charge imbalance between the 1:1 ordered and disordered or the 1:2 ordered regions, but can be promoted by La doping to

reduce the charge effect by bringing the Zn/Nb ratio closer to 1:1. K doped into Ba site does not destroy 1:1 type ordering, the system favors oxygen vacancy compensation instead.

(c) The 1:2 type ordering is believed to be consistent with the chemical composition, and therefore can be enhanced by high temperature annealing treatments.

(d) The type of ordering in non-stoichiometric BZN depends on the Zn/Nb ratio. If the Zn/Nb ratio is greater than $\frac{1}{2}$, it prefers 1:1 type ordering; if the Zn/Nb ratio is less than $\frac{1}{2}$, it favors 1:2 type ordering. Up to the present understanding, Zn rich BZN favoring 1:1 type ordering is consistent with the charge imbalance model. On the other hand, Nb rich BZN preferring 1:2 type ordering can be related to the change of defect structure.

(3) Defect chemistry and electrical transport properties

(a) The defect structure of stoichiometric BZN is closely related to its parent phase BT. The so-called "stoichiometric BZN" (or referred to as undoped BZN) is always an acceptor doped material because of unavoidable acceptor impurities, uncertainty in the Zn/Nb ratio and ZnO loss during high temperature processing. Typical "intrinsic" oxygen vacancy concentration in a stoichiometric BZN is estimated to be around 1500 (ppm atom). The intrinsic ionic disorder may be well described by Schottky disorder. Except for high $V_O^{\cdot\cdot}$ concentrations, the B-site cation vacancies concentration is always higher than the A-site cation vacancy concentration due to Zn loss at high temperatures during processing. The defect compensation species for various dopants in BZN are as follows:

Acceptor doped on A site	------	$V_O^{\cdot\cdot}$	(1:1 ordering)
Acceptor doped on B site	------	$V_O^{\cdot\cdot}$	(1:1 ordering)
Donor doped on A site	------	Zn/Nb ratio self adjustment (enhancement of 1:1 ordering)	
Donor doped on B site	------	V_{Zn}'' and V_{Nb}''''' (enhancement of 1:2 ordering)	

(b) Stoichiometric BZN has very small ionic non-stoichiometry. The ionic conductivity is usually 2~3 orders of magnitude lower than the corresponding electronic conductivity.

(c) The defect diagram in concentration and oxygen partial pressure space at constant temperature was constructed based on the experimental data. There is no obvious difference between BZN and BT. For the heavily donor-doped case where metal vacancies are the defect compensation species, the concentrations of V_{Zn}'' and V_{Nb}''''' must have an abrupt change in order to fit the data using the present defect model. This feature is also present in BT. This behavior may be correlated to the 1:2 type ordering in BZN case. Zn and Nb vacancies promote 1:2 ordering, and this ordering in turn lowers the formation energy of the vacancies. The exact mechanism for the heavily donor doped case is not clear at present.

(d) The indirect band gap at 0 K for stoichiometric BZN was determined to be 3.70 ± 0.25 eV. The other thermodynamic parameters, such as mass action constants for intrinsic electronic disorder K_i, for oxidation K_O and for reduction K_R were determined as follows:

$$K_i = 7.92*10^{49}\exp(-3.70 \text{ eV}/kT) \ (\text{cm}^{-6})$$

$$K_O = 2.25*10^{51}\exp(-2.74 \text{ eV}/kT) \ (\text{cm}^{-6}\text{atm.}^{\frac{1}{2}})$$

$$K_R = 2.79*10^{48}\exp(-4.66 \text{ eV}/kT) \ (\text{cm}^{-6}\text{atm.}^{\frac{1}{2}})$$

(e) Both electrons and holes conduct by a small polaron mechanism. The thermally activated hopping energies for electrons and holes are 0.33 eV and 0.34 eV, respectively. The mobility for both charge carriers is in the neighborhood of 10^{-4} (cm^2/V-sec.) at 1000°C. All calculations have been based on the non-adiabatic small polaron model.

(f) Finally, a computer simulation based on the proposed defect model, thermodynamic and electrical transport parameters determined from experiments was carried out for stoichiometric and acceptor doped BZN. The defect concentrations and conductivities were calculated. The computer simulation yielded an excellent agreement between theoretical calculations and experimental observations.

In conclusion, a self-consistent picture of the phase transition, ordering and defects along with their migration in BZN was obtained.

151

The combined study of microstructure and defect chemistry on self-compensated complex perovskite is still in its early stages. This work is a preliminary study on the model system barium zinc niobate. In order to obtain a better understanding of the structure, defects and property relationship, further research is needed. The suggestions for future study on this subject will be basically divided into two parts: direct extension of this work and related studies applied to the general self-compensated complex perovskites.

8.1) *Direct Extension of This Work*

As a direct extension of this work, the following aspects are important and interesting:

(1) One of the main purposes of this work is to study the relationship between microwave properties and microstructure/defect chemistry. Due to experimental limitation, we could not conduct these experiments in the present work. The measurement of high frequency properties of a series of BZN samples is an essential task. The conditions, such as different dopant species, doping levels, heat treatment, redox treatment and microstructural development, will have direct impact on the high frequency properties. A complicated microstructure is believed to degrade the high frequency properties especially the Q factor of BZN when used as a microwave resonator.

(2) This work reveals a rather interesting ordering behavior of BZN. The ordering type depends on the Zn/Nb ratio and ordering degree depends on the doping or heat treatment or the Zn/Nb ratio. Whether or not this is generally true for BZN is an immediate request for the investigation. Acceptor or donor doping, such as Al^{+3} as an acceptor and W^{+6} as a donor in the B-site, could be worth studying. In the case of the A-site, Sr^{+2} doping may increase the probability for the A-site cation to switch into the B site which is expected to affect the ordering behavior.

(3) The heavily donor doped BZN and BT behave similarly. Up to now, there is not a satisfactory model that can interpret both cases. In the present study, an ordering-vacancy model was proposed for BZN that provides a logical link between the ordering phenomenon and defect chemistry. However, whether this model can be

applied to BT is a question remaining to be solved. A systematic defect chemistry and microstructural study of heavily doped BT is suggested. Upon heavily donor doping, such as Nb in Ti site up to 14 mol.%, we speculate that the degree of defect complex or some sort of ordering should increase with increasing amounts of doping. This may be the only way to attribute the abrupt increase in vacancy concentration for BT.

(4) The defect model of BZN is closely related to that of BT. However, in the microwave resonator manufacture where BZN is used as a microwave resonator material, a small amount of Mn is often added as a sintering aid to get a high density, pore free body and to reduce sintering temperature. As mentioned in chapter 4, this kind of transition metal ion would introduce complication into the defect structure. How does this relate to the ordering phenomenon and microwave property? This is another direct extension of the present work.

(5) In this work, we have demonstrated that from BT to BZN, the dielectric properties show a transition from the paraelectric to ferroelectric state. The gradual change from first order to second order or DPT indicates the possible existence of a superparaelectric state (Yao, X., 1987; 1989). The field induced phase transformation in terms of both conventional dielectric measurement and dynamic observation of this superparaelectric domains using in-situ hot-electric field stage in TEM could be of very much interest (Randall, C.A., et.al., 1987).

8.2) *Additional Studies*

Several more studies, as suggested below, would provide more information in terms of applying this combination study to general self-compensated complex perovskite systems.

(1) This work is currently restricted to BZN, a nice model system but not the best microwave resonator candidate material. The combination, such as BZN-BZT, BZN-BMN and BZT-BMT, is often used to reduce the temperature coefficient of a resonator. The ordering behavior could be quite interesting in these systems. A study of the microstructure, defect chemistry of these systems is of more general meaning for the microwave resonator manufacturing industry.

(2) The complex microchemical ordering phenomenon should be solved in general. A re-investigation of all self-compensated complex perovskites of the general formula $A(B'_{1/3}{}^{+2}B''_{2/3}{}^{+5})O_3$ and $A(B'_{2/3}{}^{+3}B''_{1/3}{}^{+6})O_3$ is an important issue. Both

theoretical and experimental work are needed. Theoretical energy calculations for ordering, computer modeling, especially for 1:1 type of ordering in 1:2 type of chemical composition will benefit a great deal for the prediction of ordering behavior in various system. Experimental verification using TEM in particular will clear the possible confusion generally caused by XRD technique. Some advanced characterization technique, such as SAXS (Small Angle X-ray Scattering) and atom probe in FIM (Field Ion Microscopy), can offer information about chemical composition characteristics and atom packing sequence of microscopic regions (down to $\sim$10 Å in size). SAXS can overcome the superimposing problem encountered in high resolution FEG-STEM (Field Emission Gun Scanning Transmission Electron Microscopy) where the information from the microdomains is interfered with by the surrounding matrix. In our case, since the differences in Zn and Nb packing due to ordering is too subtle (the ionic radii of these two ions are similar), HRTEM failed to provide the detailed information about atom type except atom packing sequence. FIM, on the other hand, can provide the atom packing sequence with explicit information about the atom type. It is therefore a hopeful experimental approach to finally reveal the chemical composition in 1:1 type of ordered microdomains and supply the solid evidence for the ordering model.

(3) All the information gathered for the current system can be directly/indirectly applied to lead-based relaxor type ferroelectric systems where a wide range of application in electronic industry has been found. The same kind of approach needs to be used to explore the structure, defect chemistry and property relationship for lead based systems.

(4) It is very fortunate for us to dig into the details in the BZN system. All self-compensated complex perovskites located near the "Y" axis in the perovskite space can be investigated using the same approach. The correlation between various systems needs to be studied based on carefully selected model systems, such as BZN, BCN $(Ba(Co_{1/3}Nb_{2/3})O_3)$, PMN, PSW, SZN $(Sr(Zn_{1/3}Nb_{2/3})O_3)$, SSN and LCN $(La(Co_{1/3}Nb_{2/3})O_3)$ etc.. Finally, we could complete our trip along the "Y" axis in the perovskite space and end up with a clear picture of this type of compound on the relationship between microstructure, defects, electrical transport properties.

REFERENCES

Adler, D., (1974): "Electrical Transport: General Concepts", in *Electrical Conductivity in Ceramics and Glass, Pt. A, p.1, ed. by Tallan, N.M., Marcell Dekker, Inc., New York.* (1975): "The Imperfect Solid—Transport Properties", in *Treatise on Solid State Chemistry, Vol. 2, Defects in Solid, p.237, ed. by Hannay, N.B.,*

Amelinckx, S. and Landuyt, J.V., (1976): "Electron Microscopy in Mineralogy", p.168, *ed. by Wenk, H.R., Springer-Verlag, Berlin.*

Arlt, G., Hennings, D. and De With, G., (1985): "Dielectric Properties of Fine-Grained $BaTiO_3$ Ceramics", *J. Appl. Phys.*, 58, p.1619.

Atkin, R.B., Holman, R.L. and Fulrath, R.M., (1971): "Substitution of Bi and Nb Ions in Lead Zirconate-Titanate", *J. Am. Ceram. Soc.*, 54, p.114.

Baxter, P., Hellicar, N.J. and Lewis, B., (1957): "Effect of Additives of Limited Solid Solution on Ferroelectric Properties of Barium Titanate Ceramics", *J. Am. Ceram. Soc.*, 42, p.465.

Blasse, G., (1965): *"New Compounds with Perovskites-like Structures"*, *J. Inorg. Nucl. Chem.*, 27, p.993.

Blumenthal, R.N. and Seitz, M.A., (1974): "Experimental Techniques", in *Electrical Conductivity in Ceramics and Glass, Pt.A, p.35, ed. by Tallan, N.M., Marcel Dekker, Inc., New York.*

Bosman, A.J. and Van Daal, H.J., (1970): "Small Polaron Versus Band Conduction in Some Transition-Metal Oxides", *Advs. in Phys.*, 19, p.1.

Bube, R.H., (1974): "Electronic Properties of Crystalline Solids_An Introduction to Fundamentals", p.233, *Academic Press, New, York.*

Buessem, W.R. and Kahn, M., (1971): "Effect of Grain Growth on Distribution of Nb in Barium titanate Ceramics", *J. Am. Ceram. Soc.*, 54, p.458.

Buessem, W.R., Cross, L.E. and Goswami, A.K., (1966): "Phenomenological Theory of High Permittivity in Fine-Grained $BaTiO_3$", *J. Am. Ceram. Soc.*, 49, p.33.

Buerger, M.J., (1978): "Elementary Crystallography", p.475, *MIT Press, Boston.*

Bunget, I. and Popescu, M., (1987): "Physics of Solid Dielectrics", *Materials Science Monographs?*

Burns, R.G., (1970): "Mineralogical Applications of Crystal Field Theory:, *Cambridge Univ. Press, London.*

Cahn, J.W. and Kalonji, G., (1982): "Symmetry in Solid State Transformation Morphologies", *Proc. of an Inter. Conf. on Solid-Solid Phase Transformations, ed. by Aaronson, H.I., Laughlin, D.E., Sekerica, R.F. and Waiman, C.M., p.3, AIME, New York.*

Catlow C.R.A. and Lewis, G.V., (1986): "Defect Studies of Doped and Undoped $BaTiO_3$ Using Computer Simulation Techniques", *J. Phys. Chem. solid*, 47, p.89.

Ceramic Source, (1986), *Vol.1, p.270 and* (1988), *Vol. 3., p.203, Am., Ceram. Soc..*

Chan, H.M., Harmer, M.P., Bhalla, A. and Cross, L.E., (1985): "TEM of the Relaxor Material $Pb(Sc_{1/2}Ta_{1/2})O_3$", *Jpn. J. Appl. Phys.*, 24, p.550.

155

Chan, H.M., Harmer, M.P. and Smyth, D.M., (1985): "Compensation Defects in Highly Donor-Doped Barium Titanate", *J. Am. Ceram. Soc.*, 69, p.507.

Chan, N.H., Sharma, R.K. and Smyth, D.M., (1981): a. "Nonstoichiometry in Undoped $BaTiO_3$", *J. Am. Ceram. Soc.*, 64, p.556. b. "Nonstoichiometry in $SrTiO_3$", *J. Electrochem. Soc.*, 128, p1763. (1982): "Nonstoichiometry in Acceptor-Doped $BaTiO_3$", *J. Am. Ceram. Soc.*, 65, p.197. (1984): "Defect Chemistry of Donor Doped $BaTiO_3$", *ibid*, 67, p285.

Chang, E.K., Harmer, M.P. and Smyth, D.M., (1989): "Non-stoichiometry and Transport in Strontium Ferrate $Sr_2Fe_2O_2$", *Submitted to the J. Solid State Chem.*.

Chen, J., Chan, H.M. and Harmer, M.P., (1989): "Ordering Structure and Dielectric Properties of Undoped and La/Na doped $Pb(Mg_{1/3}Nb_{2/3})O_3$", *J. Am. Ceram. Soc.*, 72, p.593.

Choi, G.M., Tuller, H.L. and Goldschmidt, D., (1986): "Electronic Transport Behavior in Single-Crystalline $Ba_{0.03}Sr_{0.97}TiO_3$", *Phys. Rev. B*, 34, p.6972.

CRC Handbook, (1986), p. B208, 67th ed., CRC press Inc., Florida.

Cross, L.E., (1990): "Agile Piezoelectric Sensors", *Am. Ceram. Soc. the 92nd Annual Meeting*, (61-*SIII*-90), Dallas, Texas. (1988): "New Ceramic Materials for Electronics and Photonics", *Am. Ceram. Soc. the 90th Annual Meeting*, (160-*B*-88), Cincinnati, Ohio. (1987): "Relaxor Ferroelectrics", *Ferroelectrics*, 76, p.124. (1984): "Dielectric Piezoelectric and Ferroelectric Components", *Ceram. Bulletin*, 63(4), p.586.

Cullity, B.D., (1978): "Elements of X-Ray Diffraction", 2nd ed., *Addison-Wesley, Lodon*.

Daniels, J. and Härdtl, K.H., (1976): "Electrical Conductivity and High Temperature Donor-Doped $BaTiO_3$ Ceramics", *Philips, Res. rept.*, 31, p.489.

Deleo, G.G., (1990), *Private Communication*.

Desu, S.B. and O'Bryan, H.M., (1985): "Microwave Loss Quality of $Ba(Zn_{1/3}Ta_{1/3})O_{1/3}$ Ceramics", *J. Am. Ceram. Soc.*, 68, p.546.

Devonshire, A.F., (1949): "Theory of $BaTiO_3$", *Phil. mag.*, 40, p.1140. (1954): "Theory of Ferroelectrics", *ibid.*, Suppl. 3, p.85.

Dulin, F.H. and Rase, D.E., (1960): "Phase Equilibria in the System $ZnO-TiO_2$", *J. Am. Ceram. Soc.*, 43, p.125.

Dunitz, J.D. and Drgel, L.E., (1957): "Electronic Properties of Transition Metal Oxide: I. Distortions from Cubic Symmetry", *J. Phys. Chem. Solids*, 3, p.20; "II. Cation Distribution Amongst Octahedral and Tetrahedral Sites", *ibid*, 3, p.318.

Edington, J.W., (1975): "Practical Electron Microscopy in Materials Science", p43, *Mcmillan Press, London*.

Edwards, A.H. and Fowler, W.B., (1982): "Theory of the Peroxy-Radical Defect in a-SiO_2", *Phys. Rev. B*, 26, p.6649.

Elliott, S.R., (1987): "AC Conduction in Amorphous Chalcogenide and Pnictide Semiconductors", *Advs. in Phys.*, 36, p.135.

Ern, V. and Newnham, R.E., (1961): "Effect of WO_3 on Dielectric Properties of Barium Titanate Ceramics", *J. Am. Ceram. Soc.*, 44, p.199.

Fesenko, E.G. and Prokopalo, O.I., (1961): "Some Data on the Phase Diagram of the $BaTiO_3-BaHfO_3$ System", *Sov. Phys.-Crst.*, 6, p.373.

Fresia, E.J., Katz, L. and Ward, R., (1959): "Cation Substitution in Perovskite—Like Phases", *J. Am. Ceram. Soc.* 81, p.4783.

Fröhlich, H., (1986): "Theory of Dielectrics", *2nd ed., Clarendon Press, Oxford.*

Galasso, F.S., (1969): "Structure, Properties and Preparation of Perovskite-Type Compounds", *Pergamon, Press, New York.*

Galasso, F.S., Barrante, J.R. and Katz, L., (1961): "Alkaline Earth-Tantalum Oxygen Phases Including Crystal Structure of an Ordered Perovskite Compound $Ba_3SrTa_2O_9$", *J. Am. Chem. Soc.*, 83, p.2830.

Galasso, F.S. and Pyle, J., (1963): a. "Ordering in Compounds of the $A(B'_{0.33}Ta_{0.33})O_{0.33}$ Type", *Inorg. Chem.*, 2, p.482. b. "Preparation and Study of Ordering in $A(B'_{0.33}Nb_{0.67})O_3$ Perovskites", *J. Phys. Chem.*, 67, p.1561.

Glass, A.M., (1988): "Materials for Photonic Switching and Integration Processing", *MRS Bulletin, p.16, August.*

Glass, A.M. and Lines, M.E., (1977): "Principles and Applications of Ferroelectric and Related Materials", *Clarendon Press, Oxford.*

Goodnough, J.B. and Longo, J.M., (1970): "Crystallographic and Magnetic Properties of Perovskite and Perovskite Related Compounds", *Landolt-Bornstein, New series, Group III, Vol. 4a, Springer-Verlag, New York.*

Griffiths, A.J. and Kemmler-Sack, S., (1980): "Perovskite Phases in the System 1. AO-UO_3, 2. in the System A_2BUO_3 with A, B=Ba, Sr, Ca", *Z. Anorg. Allg. Chem.*, 466, p.116.

Hägemann, H.J, (1980): "Akzeptorionen in $BaTiO_3$ und $SrTiO_3$ und ihre Auswirkung auf die Eigenschaften von Titanatkeramiken", *PhD Dissertation.*

Han, Y.H., Appleby, J.B. and Smyth, D.M., (1987): "Calcium as an Acceptor-Impurity in $BaTiO_3$", *J. Am. Ceram. Soc.*, 70 p.96.

Härdtle K.H. and Hennings, D., (1972): "Distribution of A-site and B-site Vacancies in (Pb, La)(Ti, Zr)O_3 Ceramics", *J. Am. Ceram. Soc.*, 55, p.230.

Harmer, M.P., Bhalla, A., Fox, B. and Cross, L.E., (1984): "Electron Microscopy of Ordered Domains in Lead Scandium Tantalate $Pb(Sc_{0.5}Ta_{0.5})O_3$", *Mater. Lett.*, 2, p.278.

Harmer, M.P., Chen, J., Peng, P., Chan, H.M. and Smyth, D.M., (1989): "Control of Microchemical Ordering in Relaxor Ferroelectric and Related Compounds", *Ferroelectrics*, 97, p.263.

Harrison, W.A., (1980): "Electronic Structure and Properties of Solids", *Freeman W.H. and Company, San Franscisco.*

He, F.C., (1979): "Structural Chemistry", *Education Press, Beijing, p.185, (in Chinese).*

Hennings, D. and Härdtl, K.H., (1970): "The Distribution of Vacancies in Lanthana-

Doped Lead Titanate", *Phys. Stat. Sol.* (a), 3, p.465.

Hennings, D., Schnell, A. and Simmon, G., (1982): "Diffuse Ferroelectric Phase Transitions in Ba(Ti$_{1-y}$Zr$_y$)O$_3$ Ceramics", *J. Am. Ceram. Soc.*, 65. p.539.

Herbert, J.M., (1982): "Ferroelectric Transducers and Sensors", *Electrocomponent Science Monographs Vol.3, Gordon and Breach Science Publishers, New York.*

Hu, Y.H., Harmer, M.P. and Smyth, D.M., (1985): "Solubility of BaO in BaTiO$_3$", *J. Am. Ceram. Soc.*, 68, p.372.

Hughes, R.C., (1977): "Time-Resolved Hole Transport in a-SiO$_2$", *Phys. Rev. B*, 15, p.2012.

Ikushima, H. and Hayakawa, S., (1965): "Electrical Properties of Ag Doped Barium Titanate Ceramics", *Jpn. J. Appl. Phys.*, 4, p.328.

Iveronova, V.I. and Katsnelson, A.A., 91977): "Modern problems of Short-Range Order", *in Order-isorder Transformations, ed. by Warunawt, P., p.180, Spinger-Verlag, Berlin.*

Jacobson, A.J., Collins, B.M and Fender, B.F., (1976): "Powder Neutron and X-ray Diffraction Determination of Structure of Ba(Zn$_{1/3}$Ta$_{2/3}$)O$_3$: Investigation of Perovskite Phases in System Ba(Zn$_{1/3}$Ta$_{2/3}$)O$_3$ and Preparation of Ba$_2$TaCdO$_{5.5}$ and Ba$_2$CeInO$_{5.5}$", *Acta Cryst.*, B32, p.1083.

Jaffe, B., Cook, W.R. and Jaffe, H., (1971): "Piezoelectric Ceramics", *Academic Press, New York.*

Jain, H., (1990): *Private communication.*

Jiang, S.J., (1979): "Electrostrictive Ceramics for Transducer Applications", *PhD dissertation, Penn. State. Univ..*

Jona, F. and Shirane, G., (1962): "Ferroelectric Crystals", *Pergamon Press, New York.*

Jonker, G.H., (1968): "The Application of Combined Conductivity and Seebeck Effect Plots for the Analysis of Semiconductor Properties", *Philips, Res. Rept.*, 23 p.131.

Jonker, G.H., (1955): "Capacitor Materials with High Dielectric Constant", *Philips Tech. Rev.* 17, p. 129.

Jonker, G.H. and Kwestroo, (1958): "The Ternary Systems BaO-TiO$_2$-SnO$_2$ and BaO-TiO$_2$-ZrO$_2$" , *J. Am. Ceram. Soc.*, 41, p. 390.

Kakegawa, K., Wakabayashi, T. and Sasaki, Y., (1986): "Preparation of Ba(Mg$_{1/3}$Nb$_{2/3}$)O$_3$ by Using Oxine", *J. Am. Ceram. Soc.*, 69, C82.

Kato, J., Yakotani, Y. and Kagata, H., (1989): "Resistance to Reduction of Lead-Based Perovskite and Its Application to Multilayer capacitor with Copper Electrode", *Ferroelectrics*, 95, p.127.

Katz, L. and Ward, R., (1964): "Structure Relations in Mixed Metal Oxides", *Inorg. Chem.*, 3, p.205.

Kawashima, S., et. al., (1978): "Low Microwave Loss Ceramics and Method of Manufacturing the Same", *US patent*, 4,121,941.

Kawashima, S., Nishida, M., Ueda, I. and Ouchi, H., (1983): "Ba(Zn$_{1/3}$Ta$_{2/3}$)O$_3$ Ceramics with Low Dielectric Loss at Microwave frequency", *J. Am. Ceram. Soc.*, 66,

p.421.

Kikuchi, R., (1974): "Superposition Approximation and Natural Iteration Calculation in Cluster Variation Method", *J. Chem. Phys.*, 60, p.1971.

Kittel, C., (1986): "Introduction to Solid State Physics", *John-Wiley & Sons, Inc., New York.*

Kofstad, P., (1983): "Non-stoichiometry Diffusion and Electrical Conductivity in Binary Metal Oxides", *R.E. Krieger Company, Florida.*

Kröger, F.A. and Vink, H.J., (1956): "Relations between the Concentrations of Imperfections in Crystalline Solids", *in Solid State Physics, ed. by Seitz, F. and Turnbull, D., Vol.3, p.307, Academic Press, New York.*

Kudzin, A.Y., (1962): "Dielectric Parameters of Monocrystals of Barium titanate Containing a Trace of Cobalt", *Sov. Phys-Crst.*, 7, p.646.

Lecomte, J., Loup, J.P., Hervieu, M. and Raveau, B., (1981): "Non-stoichiometry and Electrical Conductivity of Strontium Niobates with perovskite Structure: I. Defect Structure of $Sr(Sr_{1/3}Nb_{2/3})O_3$", *Phys. Stat. Sol.*, 65, p.743. "II. Ionic Conductivity of $Sr(Sr_{1/3+x}Nb_{2/3-x})O_{3-3X/2}$", *ibid.*, 66, p.551. (1982): "III. Thermodynamic Data for $Sr(Sr_{1/3+x}Nb_{2/3-x})O_{3-3X/2}$", *ibid.*, 69, p.359.

Levinson, L.M., (1988): "Electronic Ceramics—Properties, Devices and Applications", *Marcel Dekker, Inc., New York.*

Liu, D.H. and Yao, X., (1989): *Unpublished work at Lehigh and Xi'an Jiaotong Univ..*

Long, S.A. and Blumenthal, R.N., (1971): "Ti-Rich Non-stoichiometric $BaTiO_3$: I. High Temperature Electrical Conductivity Measurement", *J. Am. Ceram. Soc.*, 54, p.515. "II. Analysis of Defect Structure", *ibid.*, 54, p. 577.

Macdonald, J.R., (1987): "Impedance Spectroscopy_Emphasizing Solid Materials and Systems", *John-Wiley and Sons, New York.*

Marks, G.W. and Monson, L.A., (1955): "Effect of Certain Group IV Oxides on Dielectrical Constant and Dissipation Factor of $BaTiO_3$", *Ind. Eng. Chem. Soc.*, 47, p.1611.

Matsumo, K., Hinga, T., Takada, K., and Ichimura, H., (1986): "$Ba(Mg_{1/3}Ta_{1/3})O_{1/3}$ Ceramics with Ultra-Low Loss at Microwave Frequencies", *Proc. of 6th IEEE Int. Symp. on Ferroelectric, June 8-11, Lehigh Univ.*

McSweeney, R., Zuk, K., (1988): "The Dielectric Properties and Grain Size Dependence of $Ba(Ti_{0.915}Zr_{0.085})O_3$: 0.15 m/o MnO_2 Ceramics with Controlled Deviations From Stoichiometry", *Am. Ceram. Soc. 90th Annual Meeting*, (16-*EP*-88), *Cincinnati, Ohio.*

McSweeney, R., Zuk, K. and Williamson, D., (1987): "Square Loop Ba(Ti, Zr)O_3 capacitors Based on Alkoxide Derived (Ti, Zr)O_2 Powders", *The first International Congress on Ceramic Powder Processing Science*, (103-*BP-87F*), Orlando, FL.

Mehta, A., (1989): "Defects and Transport in LiNbO_3", *PhD Dissertation, Lehigh Univ.*.

Mitsui, T., et. al., (1976): "An Introduction to the Physics of Ferroelectricity", *Gorden and Beach Scientific Pub., New York.*

Mott, N.F. and Davis, E.A., (1979): "Electronic Process in Non-Crystalline Materials", *Clarendon Press, Oxford.*

Nagels, P., (1980): "Experimental Hall Effect Data for a Small-Polaron Semiconductor", *in The Hall Effect and Its Applications, ed. by Chien, C.L. and Westlake, C.R., p.253, Plenum Press, New York.*

Nakamura, T. and Nomura, S., (1966): "Dielectric Properties in BaTiO_3-BaSnO_3 and BaTiO_3-Ba(Fe$_{1/2}$Ta$_{1/2}$)O_3 System", *Jpn. J. Appl. Phys.*, 5, *p.*1191.

Newnham, R.E., (1989): "Electroceramics", *Rep. prog. Phys.*, 52, *p.*123. (1975): "Structure—Property Relations", *Springer-Verlag, New York*, (1975).

Nishioka, A., Sekikawa, K. and Owoki, M., (1956): "Effect of Fe$_2$O$_3$ on the Properties of BaTiO_3 Single Crystals", *J. Phys. Soc. Jpn.*, 11, *p.*180.

Normura, S., (1955): "Dielectric Properties of Titanate Containing Sn^{+4} ions ", *J. Phys. Soc. Jpn.*, 10, *p.*112.

Ouchi, H., Nagano, K. and Hayakawa, S., (1965): "Piezoelectric Properties of Pb(Mg$_{1/3}$Nb$_{1/3}$)$O_{1/3}$-PbTi$O_{1/3}$-PbZr$O_{1/3}$ Solid Solution Ceramics", *J. Am. Ceram. Soc.*, 48, *p.*630.

Padel, L.,Poix, P. and Michel, A., (1972): "Préparation et Étude Cristallographique du Systéme Ba$_2$(UMg)O_6−Ba$_2$(U$_{2/3}$Fe$_{4/3}$)O_6", *Revue de chimie minerale*, 9, *p.*337.

Parkash, O., Peng, P., Jain, H. and Smyth, D.M., (1990), b. *unpublished work at Lehigh Univ.*.

Parkash, O., Prasad, C.D. and Kumar, D., (1990): a. "Dielectric Relaxation Behavior of the System Sr$_{1-x}$La$_x$Ti$_{1-x}$Co$_x$)O_3 (x<0.40)", *J. Mater. Sci.*, 25, *p.*487.

Pauling, L., (1924): "The Crystal Structures of Ammonium Fluoferrate Fluo-Aluminate and Oxyfluomolybdate", *J. of Am. Chem. Soc.*, 46, *p.*2738.

Payne, W.H. and Tennery, V.J., (1965): "Dielectrical and Structural Investigations of the System BaTiO_3-BaHfO_3", *J. Am. Ceram. Soc.*, 48, *p.*413.

Pechini, M., (1967): "Method of Preparing Lead and Alkaline Earth Titanates and Niobates and Coatings Using the Same to Form a Capacitor", *US Patent*, 3,330,697.

Peng, P., Parkash, O., Jain, H. and Smyth, D.M., (1990): "Dielectric Relaxation Behavior of the System Sr$_{1-x}$La$_x$Ti$_{1-x}$M$_x$)O_3 (M=Cr, Co and Ni)", *to be published.*

Pohanka, R.C., Rice, R.W. and Walker, Jr. B.E., (1976): "Effect Internal Stress on the Strength of BaTiO_3", *J. Am. Ceram. Soc.*, 59, *p.*71.

Porter, D.A. and Easterling, K.E., (1984): "Phase Transformation in Metals and

Alloys", *Van Nostrand reinhold Co. Ltd.*.

Randall, C.A., Barber, D.J. and Whatmore, R.W., (1987): "In-situ TEM Experiments on Perovskite Structured Ferroelectric Relaxor Materials", *J. Micro.*, 145, p.275.

Raymond, M.V., (1990): *unpublished work at Lehigh Univ.*.

Remeika, J.P., (1954): "A Method for Growing $BaTiO_3$ Single Crystals", *J. AM. Chem. Soc.*, 76, p.940.

Reynaud, P.F., (1976): "Mise en Evidence Par Diffraction Electronique de la Mise en Ordre des Atomes de Nickel en Excés par Rapport à La Stoechiométrie dans Les Alliages $\beta'-Ni_2Al$", *J. Appl. Cryst.*, 9, p.263.

Roy, R., (1964): "Multiple Ion Substitution in the Perovskite Lattice", *J. Am. Ceram. Soc.*, 37, p.581.

Sabatier, R., Wathle, M., Besse, J. and Baud, G., (1971): "Perovskites Oxyfluorees et Oxygenees Lacunaires du Mo^{VI} et du W^{VIn}", *J. Inorg. Nucl. Chem.*, 33, p.1597.

Sakudo, T., (1957): "Effect of Iron Group on the Dielectric Properties of $BaTiO_3$ Ceramics", *J. Phys. Soc. Jpn.*, 12, p.1050.

Scott, J.F. and De Araujo, C.A.P., (1989): "Ferroelectric Memories", *Science*, 246, p.1400.

Setter, N., (1980): "The Role of Positional Disorder in Ferroelectric Relaxors", *PhD Dissertation, Penn. State. Univ.*, (1980).

Shannon, R.D. and Prewitt, C.T., (1969): "Effective Ionic Radii in Oxides and Fluorides", *Acta Cryst.*, B25, p.925.

Sharma, R.K., Chan, N.H. and Smyth, D.M., (1981): "Solubility of Ti_2O in $BaTiO_3$", *J. Am. Ceram. Soc.*, 64, p.448.

Shewmon, P.G., (1983): "Diffusion in Solids", *J. Williams Book Company, OK.*

Sinyakov, E.V., Dudnik, E.F. and Hlerova, S.A., (1967): "Influence of Mechanical Pressure on Polarization Process in $BaTiO_3$ Single Crystals and in Solid Solutions of $BaTiO_3$-ZnO", *Sov. Phys._Solid State*, 8, p.2278.

Sinyakov, E.V. and Stafiichik, E.A., (1960): "$BaTiO_3$ Based Solid Solution of Niobates and Tatalates of Transition Metals", *Sov. Phys._Solid State*, 2, p.66.

Slater, J.C., (1950): "The Lorentz Correction in Barium Titanate", *Phys. Rev.*, 78, p.748.

Sleight, W., Longo, J.M. and Ward, R., (1962): "Compounds of Osmium and Rhenium with the Ordered Perovskite Structure", *Inorg. Chem.*, 1, p.245.

Smith, P.W., (1988): "Photonic Switching: Present Research and Future Prospects", *SPIE*, Vol.881, p.30.

Smyth, D.M., (1984): "The Role of Impurities in Insulating Transition Metal Oxides", *Prog. Solid St. Chem.*, 15, p.145. (1985): "Defects and Order in Perovskite-related Oxides", *Ann. Rev. Mater. Sci.*, 15, p.329. (1989): "Defects and Structural Changes in Perovskite Systems: From Insulators to Superconductors", *Cryst. Latt. Def. and Amorph. Mat.*, 18, p.355.

Spence, J.C.H., (1981): "Experimental High-resolution Electron Microscopy", *Oxford*,

Clarendon Press.

Steward, E.G. and Booksby, H.P., (1951): "Pseudo-cubic Alkaline-earth Tungstates and Molybdates of the R_3MX_3 Type", *Act. Cryst.*, 4, p.503.

Su .M.Y., Elsbernd, C.E. and Mason, T.O., (1990): "Jonker 'Pear' Analysis of Oxide Superconductors", *J. Am. Ceram. Soc.*, 73, p.415.

Subbarao, E.C. and Shirane, G., (1959): "Dielectrical and Structural Studies in the System $Ba(Ti, Nb)O_3$ and $Ba(Ti, Ta)O_3$", *J. Am. Ceram. Soc.*, 42, p.279.

Takada, K., (1989), *Private Communication*.

Takada, K., Chang, E.K. and Smyth, D.M., (1987): "Rear Earth Additions to $BaTiO_3$", in *Adv. in Ceram.*, *Vol*.19, *Multilayer Ceramic Devices*, p.147.

Tamura, H., Konoike, T, Sakab, Y and Wakino, K, (1984): "Improved High-Q Dielectric Resonator with Complex Perovskite Structure", *J. Amer. Cer. Soc.* 67, C59.

Tamura, H., Sagala, D.A. and Wakino, K, (1986): "Lattice Vibrations of $Ba(Zn_{1/3}Ta_{2/3})O_3$ Crystal with Ordered Perovskite Structure", *Jpn. J. Appl. Phys.*, 25, p.787.

Tanner, L.E. and Leamy, H.J., (1977): "The Microstructure of Order-Disorder Transitions", in *Order-Disorder Transformations*, ed. by *Warunawt, P.*, p.180, *Spinger-Verlag, Berlin*.

Tendeloo, G.V. and Amelinckx, S., (1974): "Group-Theoretical Considerations Concerning Domain Formation in Ordered Alloys", *Acta Cryst.*, A30, p.431.

Tennery, V.J. and Hang, K.W., (1969): "Structural and Dielectric Properties of $Ba(Zn_{1/3}Nb_{2/3})O_3$", *J. Am. Ceram. Soc.*, 53, p.118.

Tien, Z.Y. and Cross, L.E., (1967): "Dielectric Relaxation in $SrTiO_3$ Solid Solution Containing Lathania", *Jpn. J. Appl. Phys.*, 6, p.459.

Timari,, P.S., Pandey, D. and Groves, P., (1989): "The Infuence of a Powder Processing Technique on Chemical Homogeneity and the Diffuse Phase Transition Behavior of $Ba_{0.9}Ca_{0.1}TiO_3$ Ceramics", *J. Phys. D: Appl. Phys.*, 22, p.837.

Treiber, V. and Kemmler-Sack, S., (1982): "Über Ordnungs-Unordnung Sphänomenebei Sauerstoff Perowskiten vom Typ $A_3^{2+}B^{2+}M_2^{5+}O_9$", *J. Solid State Chem.*, 43, p.51.

Uchikoba, F., Sawamura, K., (1989): "Control of Valence Structure in $Pb(Mg_{1/3}Nb_{2/3})O_3$", *Ferroelectrics*, 93, p.387.

Uchino, K., (1987): "Materials and Applications of Actuators", *Am. Ceram. Soc. 89th Annual Meeting*, (31-e-87), *Pittsburgh, PA*.

Vecchio, K.S., (1988): "Analytical Electron Microscopy and In-situ Fatigue Study of Al-Li Based Alloys", *PhD Dissertation, Lehigh Univ.*.

Verbitskaya, T.N., Zhdanov, G.S. Venevtsev, Y. N. and Solov'ev, S.P., (1958): "   ", *Kristallografiya*, 3, p.189.

Wakino, K, (1989): "Recent Development of Dielectrical Resonator Materials and Filters in Japan", *Ferroelectrics*, 91, p.80.

Wakino, K., Sagala, D.A. and Tamura, H., (1985): "Far Infrared Reflection Spectra of

$Ba(Zn_{1/3}Ta_{2/3})O_3 - BaZrO_3$ Dielectric Resonator Material", *Jpn. J. Appl. Phys.*, 24, *Suppl. 2, p.1042.*

Watton, R., (1989): "Ferroelectric Materials and Devices in Infrared Detection and Imaging", *Ferroelectrics*, 91, *p.87.*

Williams, D.B., (1984): "Practical Analytical Electron Microscopy in Materials Science", *Philips Instruments Inc., NJ.*

Wimmer, J.M. and Bransky, I., (1974): "Electronic Conduction", *in Electrical Conductivity in Ceramics and Glass, Pt. A, p.1, ed. by Tallan, N.M., Marcell Dekker, Inc., New York.*

Yao, X., (1987): *Private communication.*

Yao, X., Chen, Z.L. and Cross, L.E., (1984): "Polarization and Depolarization Behavior of Hot-Pressed Lead Lanthanum Zirconate Titanate Ceramics", *Ferroelectrics*, 54, *p.163.*

Yoshioka, H., (1987): "Ordering of Cations in $Ba(Mg_{1/3}Nb_{2/3})O_3$ and $Ba(Zn_{1/3}Nb_{2/3})O_3$", *Bull. Chem.Soc. Jpn.*, 60, *p.3433.*

Zhang, X.W., Han, Y.H., Lal, M. and Smyth, D.M., (1987): "Defect Chemistry of $BaTiO_3$ with Additions of $CaTiO_3$", *J. Am. Ceram. Soc.*, 70, *p.180.*

Zhang, X.W., Wang, Q. and Gu, B.L., (1990): a. "A Study for Predetermination of the Order-Disorder Transitions in $A(B'B'')O_3$ Perovskite Type Ceramics", *Submitted to J. Am. Ceram. Soc..* b. *private communication.*

APPENDICES

I. List of $A(B'_{2/3}B''_{1/3})O_3$ Compounds

Compound	a(Å)	b(Å)	c(Å)	Structure	References
$Ba(Er_{2/3}W_{1/3})O_3$	8.386			$(NH_4)_3FeF_6$ type*	1
$Ba(Eu_{2/3}W_{1/3})O_3$	8.605			$(NH_4)_3FeF_6$ type	1
$Ba(Fe_{2/3}U_{1/3})O_3$	8.232			$(NH_4)_3FeF_6$ type	2
$Ba(Gd_{2/3}W_{1/3})O_3$	8.411			$(NH_4)_3FeF_6$ type	1, 3
$Ba(In_{2/3}U_{1/3})O_3$	8.512			$(NH_4)_3FeF_6$ type	2
$Ba(In_{2/3}W_{1/3})O_3$	8.321			$(NH_4)_3FeF_6$ type	1
$Ba(La_{2/3}W_{1/3})O_3$	8.580			$(NH_4)_3FeF_6$ type	3
$Ba(Lu_{2/3}W_{1/3})O_3$	?			?	1
$Ba(Nd_{2/3}W_{1/3})O_3$	8.513			$(NH_4)_3FeF_6$ type	1
$Ba(Sc_{2/3}U_{1/3})O_3$	8.490			$(NH_4)_3FeF_6$ type	2
$Ba(Sc_{2/3}W_{1/3})O_3$	8.240			$(NH_4)_3FeF_6$ type	4, 1
$Ba(Y_{2/3}U_{1/3})O_3$	8.700			$(NH_4)_3FeF_6$ type	2
$Ba(Y_{2/3}W_{1/3})O_3$	8.374			$(NH_4)_3FeF_6$ type	1
$Ba(Yb_{2/3}W_{1/3})O_3$	?			?	1
$Pb(Fe_{2/3}W_{1/3})O_3$	?			?	5, 6
$Pb(Sc_{2/3}W_{1/3})O_3$	8.???			$(NH_4)_3FeF_6$ type#	7
$Sr(Cr_{2/3}Re_{1/3})O_3$	8.010			$(NH_4)_3FeF_6$ type	8
$Sr(Cr_{2/3}U_{1/3})O_3$	8.000			$(NH_4)_3FeF_6$ type	2
$Sr(Fe_{2/3}Re_{1/3})O_3$	7.890			$(NH_4)_3FeF_6$ type	8
$Sr(Fe_{2/3}W_{1/3})O_3$	3.945		3.951	? tetragonal	9, 3
$Sr(In_{2/3}Re_{1/3})O_3$	8.297			$(NH_4)_3FeF_6$ type	8
$La(Co_{2/3}Nb_{1/3})O_3$	5.580	5.580	7.890	? tetragonal	3
$La(Co_{2/3}Sb_{1/3})O_3$	5.570	5.570	7.890	? tetragonal	3

* $(NH_4)_3FeF_6$ type stands for 1:1 type ordering scheme [10]. Most structural work is based on the XRD data unless otherwise indicated.

\# This ordering has been observed using both XRD and TEM techniques [7].

? This means that either there are no data currently available or the conclutions are based on the XRD data. We feel that all of those compounds with "?" mark should be re-examined using TEM technique.

II. List of $A^{+2}(B'^{+2}_{2/3}B''^{+5}_{1/3})O_3$ Compounds

Compounds	a(Å)	b(Å)	c(Å)	Structure XRD TEM	References
$Ba(Ca_{1/3}Nb_{2/3})O_3$	5.920		7.250	$Ba(Sr_{1/3}Ta_{2/3})O_3$ type(X)*	11
$Ba(Ca_{1/3}Ta_{2/3})O_3$	5.895		7.284	$Ba(Sr_{1/3}Ta_{2/3})O_3$ type(X)	12,13,14
$Ba(Cd_{1/3}Nb_{2/3})O_3$	4.168			?	11
$Ba(Cd_{1/3}Ta_{2/3})O_3$	4.167			?	15
$Ba(Co_{1/3}Nb_{2/3})O_3$	4.09			?	16
$Ba(Co_{1/3}Ta_{2/3})O_3$	5.776		7.082	$Ba(Sr_{1/3}Ta_{2/3})O_3$ type(X)	15,17
$Ba(Cu_{1/3}Nb_{2/3})O_3$	8.040		8.400	? tetragonal	3
$Ba(Fe_{1/3}Nb_{2/3})O_3$	4.085			?	11
$Ba(Fe_{1/3}Ta_{2/3})O_3$	4.100			?	16
$Ba(Mg_{1/3}Nb_{2/3})O_3$	5.770		7.080	$Ba(Sr_{1/3}Ta_{2/3})O_3$ type(X)	3,11,16
$Ba(Mg_{1/3}Ta_{2/3})O_3$	5.782		7.067	$Ba(Sr_{1/3}Ta_{2/3})O_3$ type(X)	14,15,18
$Ba(Mn_{1/3}Nb_{2/3})O_3$	?			?	1
$Ba(Mn_{1/3}Ta_{2/3})O_3$	5.819		7.127	$Ba(Sr_{1/3}Ta_{2/3})O_3$ type(X)	19
$Ba(Ni_{1/3}Nb_{2/3})O_3$	4.074			?	6,11,17
$Ba(Ni_{1/3}Ta_{2/3})O_3$	5.758		7.052	$Ba(Sr_{1/3}Ta_{2/3})O_3$ type(X)	14,15,17
$Ba(Pb_{1/3}Nb_{2/3})O_3$	4.260			?	11
$Ba(Pb_{1/3}Ta_{2/3})O_3$	4.250			?	15
$Ba(Zn_{1/3}Nb_{2/3})O_3$	4.094			?	6,11,16 20
$Ba(Zn_{1/3}Nb_{2/3})O_3$	8.188			$(NH_4)_3FeF_6$ type(E)	20
$Ba(Zn_{1/3}Nb_{2/3})O_3$	5.782		7.097	$Ba(Sr_{1/3}Ta_{2/3})O_3$ type(E,X)	20,21,22
$Ba(Zn_{1/3}Ta_{2/3})O_3$	5.782		7.097	$Ba(Sr_{1/3}Ta_{2/3})O_3$ type(E,X)	14,15,16 20,21,22
$Ca(Ni_{1/3}Nb_{2/3})O_3$	3.880			?	6
$Ca(Ni_{1/3}Ta_{2/3})O_3$	3.930			?	17
$Pb(Co_{1/3}Nb_{2/3})O_3$	4.040			?	6,23
$Pb(Co_{1/3}Ta_{2/3})O_3$	4.010			?	23
$Pb(Co_{1/3}Ta_{2/3})O_3$	?			complex ordering(E)	24
$Pb(Mg_{1/3}Nb_{2/3})O_3$	4.041			?	6,25
$Pb(Mg_{1/3}Nb_{2/3})O_3$	8.082			$(NH_4)_3FeF_6$ type(E)	26,27,28

Compound	a	c	Structure type	Ref.
$Pb(Mg_{1/3}Ta_{2/3})O_3$	4.020		?	6,23
$Pb(Mn_{1/3}Nb_{2/3})O_3$	?		?	6
$Pb(Ni_{1/3}Nb_{2/3})O_3$	4.025		?	6,25
$Pb(Ni_{1/3}Nb_{2/3})O_3$	8.050		$(NH_4)_3FeF_6$ type(E)	27,29
$Pb(Ni_{1/3}Ta_{2/3})O_3$	4.010		?	6,23
$Pb(Zn_{1/3}Nb_{2/3})O_3$	4.040		?	23,28,29
$Pb(Zn_{1/3}Nb_{2/3})O_3$	8.080		$(NH_4)_3FeF_6$ type(E)	27,29
$Sr(Ca_{1/3}Nb_{2/3})O_3$	5.760	7.16	$Ba(Sr_{1/3}Ta_{2/3})O_3$ type(X)	11
$Sr(Ca_{1/3}Sb_{2/3})O_3$	8.170		$(NH_4)_3FeF_6$ type(X)	3
$Sr(Ca_{1/3}Ta_{2/3})O_3$	5.764	7.096	$Ba(Sr_{1/3}Ta_{2/3})O_3$ type(X)	15
$Sr(Cd_{1/3}Nb_{2/3})O_3$	4.089		?	11
$Sr(Co_{1/3}Nb_{2/3})O_3$	8.010		$(NH_4)_3FeF_6$ type(X)	3
$Sr(Co_{1/3}Sb_{2/3})O_3$	7.990		$(NH_4)_3FeF_6$ type(X)	3
$Sr(Co_{1/3}Ta_{2/3})O_3$	5.630	6.937	$Ba(Sr_{1/3}Ta_{2/3})O_3$ type(X)	15,16
$Sr(Cu_{1/3}Sb_{2/3})O_3$	7.840	8.190	tetragonal(X)	3
$Sr(Fe_{1/3}Nb_{2/3})O_3$	3.997	4.018	? tetragonal(X)	11
$Sr(Mg_{1/3}Nb_{2/3})O_3$	5.660	6.980	$Ba(Sr_{1/3}Ta_{2/3})O_3$ type(X)	11
$Sr(Mg_{1/3}Sb_{2/3})O_3$	7.960		$(NH_4)_3FeF_6$ type(X)	3
$Sr(Mg_{1/3}Ta_{2/3})O_3$	5.652	6.951	$Ba(Sr_{1/3}Ta_{2/3})O_3$ type(X)	15,17
$Sr(Mn_{1/3}Nb_{2/3})O_3$	?		?	1
$Sr(Mn_{1/3}Ta_{2/3})O_3$	?		?	1
$Sr(Ni_{1/3}Nb_{2/3})O_3$	5.640	6.900	$Ba(Sr_{1/3}Ta_{2/3})O_3$ type(X)	6,11
$Sr(Ni_{1/3}Ta_{2/3})O_3$	5.607	6.923	$Ba(Sr_{1/3}Ta_{2/3})O_3$ type(X)	15,16
$Sr(Pb_{1/3}Nb_{2/3})O_3$	?		?	1
$Sr(Pb_{1/3}Ta_{2/3})O_3$	?		?	1
$Sr(Zn_{1/3}Nb_{2/3})O_3$	5.660	6.950	$Ba(Sr_{1/3}Ta_{2/3})O_3$ type(X)	11,16
$Sr(Zn_{1/3}Ta_{2/3})O_3$	5.664	6.951	$Ba(Sr_{1/3}Ta_{2/3})O_3$ type(X)	15,16

* X stands for XRD study and E for TEM study.

? This symbol has the same defination as that in the appendix I.

References:

[1] Galasso, F., *Structures, properties and preparation of perovskite-type compounds*, Pergamon press, New York, (1969).

[2] Sleight, A.W. and Ward, R., *Inorg. Chem.*, 1 p.790, (1962).

[3] Blasse G., J. Inorg. Nucl. Chem., 27, p.993, (1965).

[4] Fresia, F.J., Katz, L. and Ward, R., J. Am. Chem. Soc., 81, p.4783, (1959).

[5] Smolenskii, G.A., Agranovskaya, A.I. and Isupov, V.A., Sov. Phys. Solid State, 1, p.907, (1959).

[6] Agranovskaya, A.I., Bulletin of Acad. Sciences of USSR Physics Series, 24, p.1271, (1960).

[7] Raymond, M.V., Unpublished work at Lehigh University, (1990).

[8] Sleight, A.W. and Ward, R., Inorg. Chem., 1, p.245, (1962).

[9] Hoffman, A., Z. Physik. Chem., 28, p.65, (1953).

[10] Pauling, L., J. of Am. Chem. Soc., 46, p.2738, (1924).

[11] Galasso, F. and Pyle, J., J. Phys. Chem., 67, p.1561, (1963).

[12] Galasso, F., Barrante, J.R. and Katz, A., J. of Am. Chem. Soc., 88, p.2830, (1961).

[13] Brown, B.W. and Banks, E., J. of Am. Chem. Soc., 76, p.963, (1954).

[14] Galasso, F. and Pinto, J., Nature, 207, p.70, (1965).

[15] Galasso, F. and Pyle, J., Inorg. Chem., 2, p.482, (1963).

[16] Galasso, F., Katz, L. and Ward, R., J. of Am. Chem. Soc., 81, p.820, (1959).

[17] Roy, R., J. Am. Ceram. Soc., 37, p.581, (1954).

[18] Matsumo, K., Hinga, T., Takada, K. and Ichimura, H., Proc. of 6th IEEE Int. Symp. on Ferroelectics, Lehigh University, June 8-11, (1986).

[19] Atiji, M. and Rundle, R.E., J. Chem. Phys., 32, p.627, (1960).

[20] Peng, P., Present work, (1990).

[21] Yoshioka, H., Bull. Chem. Soc. Jpn., 60, p.3433, (1987).

[22] Wakino, K., Sagala, D.A. and Tamura, H., Jpn. Appl. Phys., 24, Suppl.2, p.1042, (1985).

[23] Bokov, V.A. and Myl'nikova, I.E., Sov. Phys., Solid State, 2, p.2428, (1961).

[24] Yan, L., Unpublished work at Lehigh University, (1989).

[25] Ismailzade, I.G., Sov. Phys., Cryst., 5, p.292, (1960).

[26] Chen, J., Chan, H.M. and Harmer, M.P., J. Am. Ceram. Soc., 72, p.593, (1989).

[27] Harmer, M.P., Chen, J., Peng, P., Chan, H.M. and Smyth, D.M., Ferroelectrics, 97, p.263, (1989).

[28] Zhang, X.W., Private communication, (1990).

[29] Sung, C.M., Gorton, A. and Chen, J., Unpublished work at Lehigh University, (1988).